TECHNISCHE UNIVERSITÄT MÜNCHEN
Lehrstuhl I für Technische Chemie

Two-Fluid Modeling of Gas-Solid and Gas-Liquid Flows: Solver Development and Application

Yefei Liu

Vollständiger Abdruck der von der Fakultät für Chemie der Technischen Universität München zur Erlangung des akademischen Grades eines

Doktors der Naturwissenschaften (Dr. rer. nat.)

genehmigten Dissertation.

Vorsitzender: Univ.-Prof. Dr. Thomas Brück

Prüfer der Dissertation:

1. Univ.-Prof. Dr.-Ing. Kai-Olaf Hinrichsen
2. Univ.-Prof. Dr. Ville R. I. Kaila

Die Dissertation wurde am 31.07.2014 bei der Technischen Universität München eingereicht und durch die Fakultät für Chemie am 29.09.2014 angenommen.

Acknowledgements

Abstract

The subject of multiphase reaction engineering is becoming increasingly important in various processes such as chemical, petrochemical, pharmaceutical and energy industries. The fluidized beds and bubble column reactors are widely employed in various applications. Nowadays computational fluid dynamics (CFD) provides the state-of-the-art capabilities of simulating the hydrodynamics in these reactors. The two-fluid model needs economical computational resources and has become practical for reactor design and scaling-up.

To evaluate the total variation diminishing (TVD) convection schemes in OpenFOAM® for gas-solid flow modeling, the two-fluid model with kinetic theory of granular flow is implemented into the open source CFD package OpenFOAM. Five TVD schemes are employed to discretize the convection terms of phase velocity and solid volume fraction. Simulated results of the two test cases give reasonable agreement with the experimental data in the literature.

By introducing a monolayer kinetic energy dissipation model into two-fluid model, tube erosion in a bubbling fluidized bed is numerically studied. The hydrodynamical simulations are performed. The time-averaged bubble frequency and bubble rise velocity are calculated to characterize the bed hydrodynamics. The erosion rates of two target tubes are simulated and the influence of the bubble behaviors on erosion rates is evaluated. The bubble behaviors are well captured by the simulations. Good agreement between the calculated and measured erosion rates is also obtained.

The fluidized bed methanation of syngas to produce synthetic natural gas (SNG) is promising to utilize the syngas. A fluidized bed methanation reactor is simulated by coupling methanation kinetics with the two-fluid flow model. The bed height is reasonably predicted with the Gidaspow and Syamlal models. The simulated axial species concentrations agree well with the measured results at the end of the bed. The effects of different operating parameters are evaluated using the established models. The increase in the gas inlet velocity results in more dilute solid concentration and larger bed expansion. The weak bed expansion results from the methanation reaction with gas volume reduction. The methane concentration is increased when increasing catalyst inventory in the reactor. The addition of water into the feedstock with low H_2/CO ratio benefits the methanation reaction.

In the CFD-PBM method, the k-ε model and Reynolds stress model (RSM) are used to account for the liquid turbulence. For the bubble column operated at 0.10 m/s, minor difference is found in the predicted profiles for 10 and 20 bubble classes. By using the Rampure drag model, Tomiyama lift model and bubble-induced turbulence model, the gas holdup is well predicted by the k-ε model and RSM. For the bubble column operated at 0.12 m/s, good agreement with experimental data is obtained when the k-ε BIT model works with the Tsuchiya drag coefficient and Tomiyama lift coefficient. The RSM with BIT gives reasonable prediction when using the Tsuchiya drag coefficient and Tomiyama lift coefficient.

Kurzfassung

Die Mehrphasen-Reaktionstechnik ist von großem Interesse und findet Anwendung in verschiedenen Prozessen der chemischen und petrochemischen Industrie sowie in der Energietechnik. Wirbelschicht- und Blasensäulenreaktoren werden in einer Vielzahl von Anwendungen verwendet. Heutzutage ist die Computational Fluid Dynamics (CFD) das Mittel der Wahl zur Berechnung der Hydrodynamik in diesen Reaktoren. Das Zwei-Fluid-Modell ist wenig rechenintensiv und findet praktische Anwendung im Reaktordesign und Scale-Up.

Um verschiedene Total Variation Diminishing (TVD) Konvektions-Schemata für die Modellierung von Gas-Partikel Strömungen mit OpenFOAM® zu evaluieren wird das Zwei-Fluid-Modell mit kinetischer Gastheorie für Partikelströmungen in der Open-Source CFD Software OpenFOAM implementiert. Fünf TVD Schemata zur Diskretisierung der Konvektionsterme von der Phasengeschwindigkeit und des Feststoffvolumenanteils werden getestet. Die Simulationsergebnisse zweier Testfälle stimmen gut mit Messdaten aus der Literatur.

Durch Verwendung eines Modells für die Monolagendissipation der kinetischen Energie in das Zwei-Fluid-Modell wird die Erosion von Rohreinbauten sowie die Strömung in blasenbildenden Wirbelschichten untersucht. Die Strömung in der Wirbelschicht wird mittels der über die Zeit gemittelten Frequenz und Aufstiegsgeschwindigkeit der Blasen beschrieben. Die Erosionsrate wird an zwei vorgegebenen Rohren simuliert und der Einfluss des Verhaltens der Blasen beschrieben. Das Verhalten der Blasen wird durch die Simulationen zufriedenstellend beschrieben. Die Übereinstimmung zwischen den berechneten und gemessenen Erosionsraten ist gut.

Die Methanisierung von Synthesegas zur Herstellung von synthetischem Erdgas (SNG) in Wirbelschichten ist ein vielversprechender Prozess zur Verwendung von Synthesegas. Ein Wirbelschichtmethanisierungsreaktor wird simuliert mittels Kopplung der Methanisierungskinetik mit dem Zwei-Fluid-Modell. Die Höhe des Betts wird durch die Gidaspow und Syamlal Modelle zufriedenstellend vorhergesagt. Die simulierten axialen Konzentrationen stimmen gut mit den gemessenen Werten am Ende des Bettes überein. Der Einfluss verschiedener Betriebsbedingungen werden mit den etablierten Modellen untersucht. Eine Vergrößerung der Gaseinlassgeschwindigkeit führt zu einer Verringerung der Feststoffkonzentration und damit einer größeren Bett-Expansion. Die geringe Expansion der Wirbelschicht ist auf die Volumenreduktion bei der Methanisierungsreaktion zurückzuführen. Die Konzentration an Methan steigt an wenn die Menge an Katalysator im Reaktor erhöht wird. Ein Hinzufügen von Wasser zum Feed begünstigt die Methanisierung bei geringen H_2/CO-Verhältnissen.

Bei der CFD-PBM (Population Balance Modell) Methode werden das k-ε und das Reynolds-Spannungs-Modell (RSM) zur Beschreibung der Turbulenz in der Flüssigphase verwendet. Bei einer Gaseintrittsgeschwindigkeit von 0.1 m/s am Eingang der Blasensäule gibt es nur geringe Unterschiede zwischen den berechneten Profilen bei der Verwendung von 10 und 20 Blasenklassen. Durch Verwendung des Rampure Widerstandsmodells, des Tomiyama

Kurzzusammenfassung

Auftriebsmodells und des blaseninduzierten Turbulenzmodells wird der Gas-Holdup durch k-ε und RSM gut wiedergegeben. Wenn die Einlassgeschwindigkeit der Blasensäule 0.12 m/s beträgt erhält man gute Übereinstimmung mit den Messdaten unter Verwendung des k-ε BIT Modells zusammen mit dem Tsuchiya Widerstandskoeffizienten und Tomiyama Auftriebskoeffizienten. Mit RSM mit BIT erhält man vernünftige Vorhersagen, wenn man den Tsuchiya Widerstandskoeffizienten und Tomiyama Auftriebskoeffizienten verwendet.

Contents

Contents

H

Contents

J

List of Figures

L

List of Tables

O

Chapter 1

Introduction

1.1 Multiphase reactor engineering

Most chemical reactors used in the commercial applications are operated with multiphase flows. The subject of multiphase reactor engineering is becoming increasingly important in various processes such as chemical, petrochemical, pharmaceutical and energy industries. The fluidized beds and bubble column reactors are studied in the thesis.

1.1.1 Fluidization and fluidized bed reactors

Fluidization is the unit operation by which the solid particles are transferred from a static solid-like state to a dynamic fluid-like state. This process occurs when a fluid (gas or liquid) is passed up through the particle bed. The majority of the fluidization applications have three important characteristics: 1) The strong mixing within a fluidized bed results in the large interfaces between the fluid-solid phases; 2) There is excellent heat transfer between the fluidized bed and heat exchangers immersed in the bed; 3) The fluidized particles can be easily transported between different reactors.
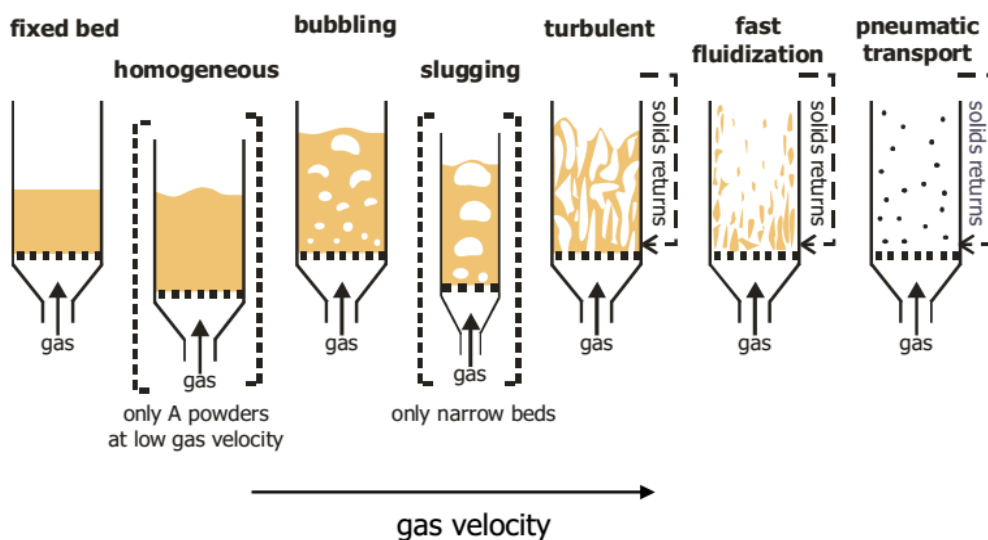
Figure 1.1: Schematics of fluidized beds operated with different regimes [1]

1

A number of flow regimes of fluidization are usually observed, as shown in Figure 1.1. The fluidized bed behaves differently with different velocities, gas and solid properties. When a gas flow with small velocities is introduced through the bed bottom, it moves upwards through the empty space in the bed between the particles. At the low gas inlet velocities, the drag force exerted on each particle is very small, and thus the bed remains at rest, which is called the fixed bed. By increasing the gas velocity, a flow regime is reached where the drag force equals the gravitational force of the particle, and the volume expansion is observed in the bed. This is the onset of fluidization and is called the minimum fluidization with a corresponding minimum fluidization velocity. With the further increase in the gas inlet velocity, the bubbles are formed in the bed and the bubbling fluidized bed occurs. As the velocity is further increased, the bubbles in the fluidized bed coalesce and grow as they rise. If the ratio of the bed height to its diameter is large enough, the size of bubbles is almost the same as the diameter of the bed. This is called the slugging regime. If the particles are fluidized at a very high gas flow rate, the particle velocity exceeds its terminal velocity. The upper surface of the bed disappears and one observes the turbulent motion of solid clusters and gas voids with various sizes and shapes. The bed operated under these conditions is called the turbulent bed. With further increases in gas velocity, the pneumatic transport of solid particles takes place.
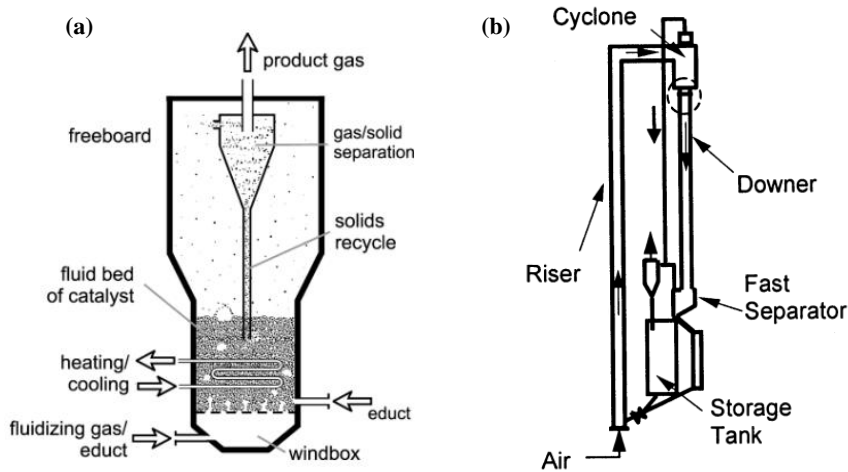
Figure 1.2: Schematics of the bubbling fluidized bed (a) [2] and the circulating fluidized bed (b) [3]

The bubbling fluidized bed is one of the mostly used gas-solid reactor types as shown in Figure 1.2(a). It is characterized by the bubbles and the superficial gas velocity is only slightly higher

than the minimum fluidization velocity. This type of fluidization is called the aggregative fluidization and under these conditions two phases can be recognized, i.e., the bubble phase and the emulsion phase. The bubbles in the bed are very similar to the gas bubbles formed in a liquid. The bubbles coalesce as they move through the bed. The movement of particles in fluidized beds depends largely on the bubbles.

The circulating fluidized beds are also widely employed in chemical, petrochemical, metallurgical and energy industries. The circulating fluidized beds have many advantages such as being a continuous operation, high throughput of gas and particles and ease of solid handling [4]. The schematic diagram of the circulating fluidized bed reactor is shown in Figure 1.2(b), which consists of riser, separator, downer and feed systems for the solids and for the fluid. The riser is a tall vertical section in which hot particles are conveyed upward. The reaction occurs in the riser due to the interaction between the reacting gases and particles. The gas and solid particles are separated at the top of the reactor by cyclones and the particles are returned to the riser via the downer. The feed gas is supplied from the bottom of the riser.

1.1.2 Bubble column reactors

In chemical process engineering, bubble columns are widely used as the gas-liquid reactors. Their typical applications can be found in oxidation, hydrogenation, wastewater treatment and Fischer-Tropsch synthesis [5]. Some distinct advantages of bubble columns are found compared to other gas-liquid contactors. The excellent heat and mass transfer characteristics can be achieved with high heat and mass transfer coefficients. Because of the construction compactness and the lack of moving parts, little maintenance and low operating costs are required. The online catalyst addition and withdrawal ability can also be achieved in the bubble columns. Because of their industrial importance, considerable attention has been paid to the design and scale-up of bubble columns during the past few decades.
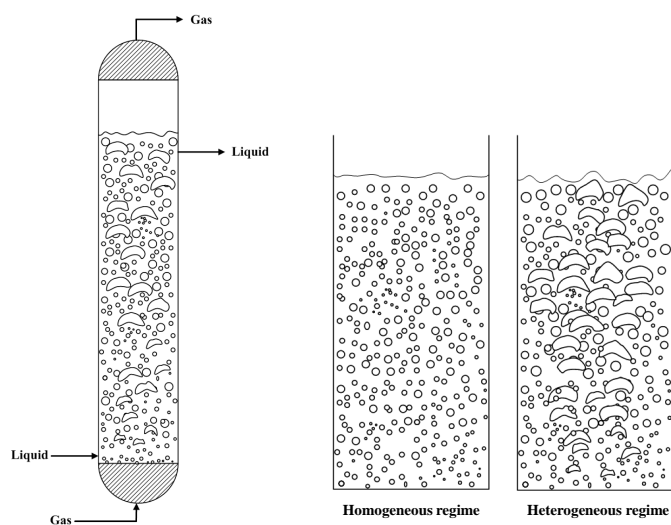
Figure 1.3: Schematic of a bubble column and flow regimes.

Figure 1.3 illustrates the schematic of a bubble column and its basic flow regimes. A bubble column reactor is constructed based on a cylindrical vessel. The gas distributor is equipped at the bottom and the gas is sparged in the form of bubbles into a liquid phase. When the bubble column is operated at low superficial gas velocities, the homogeneous flow regime (bubbly flow regime) is observed. The small spherical bubbles travel upwards through the liquid with nearly the same rise velocities. The interactions between bubbles such as coalescence and breakup are negligible in this flow regime. The bubble size distribution is found to be narrow and mono-modal. The heterogeneous flow regime (churn-turbulent regime) occurs at high superficial gas velocities (greater than 5 cm/s). A wide bubble size distribution is obtained due to the bubble coalescence and breakup. The non-uniform radial gas distribution causes the bulk liquid circulation in this flow regime. The heterogeneous flow regime is frequently observed in the industrial bubble columns.

1.2 Computational methods for multiphase flow

A detailed understanding of multiphase phenomena is crucial for analysing, designing and scaling of the multiphase reactors. Over the past decades, computational fluid dynamics (CFD) has been adopted by researchers to study the underlying physics of the gas-solid and gas-liquid flows. Several models such as the local instantaneous formulations with explicit treatment of interface and the macroscopic continuum method based on various averaging methods are presented. Three levels of modeling can be identified based on the spatial and temporal resolution of the models.

1.2.1 Direct numerical simulation

The gas-particle direct numerical simulation methods have been rapidly developing in the past decade. The trajectories of the discrete particles are determined by the solution of Newton's equations of motion. The flow field around each particle is resolved based on the full Navier-Stokes equation (continuum DNS). The forces acting on particles are estimated by integrating the stresses on the surfaces of particles. No empirical coefficients associated with the drag and lift forces are required in the DNS method. The Joseph group (Hu [6]; Pan et al. [7]) and the Banerjee group (Pan and Banerjee [8, 9]) are well known for the DNS method. Recently, Deen et al. [10] developed a novel simulation technique to perform direct numerical simulation of fluid flow and heat transfer in dense fluid-particle systems. The fluid-solid coupling was achieved by the direct incorporation of the boundary condition (with a second-order method) at the surface of the particles.

The direct numerical simulation of gas-liquid flow is also called interface resolving method. The DNS techniques are based on the local instantaneous conservation equations. These methods focus on the finest level, i.e. individual bubbles, small vortices behind bubbles and bubble-bubble interactions. All the closure equations for the forces acting on a bubble can be directly computed. However, these approaches are restricted to a single bubble or a

few interacting bubbles due to very expensive computational requirements. Nowadays three DNS methods are used, i.e. the volume-of-fluid method (VOF) [11], the level-set method [12] and the front-tracking method [13]. The VOF method is a surface-tracking technique applied to a fixed mesh. It simulates two or more immiscible fluids by solving one single momentum equation and tracking the volume fraction of each fluid. In the open source CFD software OpenFOAM [14], the standard solver `interFoam` is developed based on the compressive volume-of-fluid method. The idea of the level-set method is to define the interface as the zero level set of a smooth scalar function. Unlike the VOF method, the interface is represented as a continuous surface. In the front-tracking method, the velocity field is obtained by solving the momentum equation on a fixed mesh, while the phase interface is represented by a set of marker particles.

1.2.2 Eulerian-Lagrangian method

In the Eulerian-Lagrangian approach, the continuous phase is treated in the Eulerian framework and the averaged equations are solved, whereas the motion of individual discrete particle is simulated by solving the Newton's equations of motion. The trajectories of the particles are computed in the control volume. In contrast to the DNS methods, the Eulerian-Lagrangian approach requires closure relations to account for the interphase forces. The closure models can be obtained from empirical relations or from more sophisticated simulations with fine resolution. Due to the significant computational resources required, the Eulerian-Lagrangian approach becomes infeasible for the simulations of large industrial-scale reactors.

Considerable efforts are made in simulating gas-solid flows using the Eulerian-Lagrangian method. The Eulerian-Lagrangian method was pioneered by Tsuji et al. [15]. Most of the gas-solid Eulerian-Lagrangian methods are developed by coupling CFD with the discrete element method (DEM). A large number of research papers on the CFD-DEM have been published over the past two decades. The Yu group made large progress in the development and application of the CFD-DEM method [16–20]. The Kuipers group also contributed a lot in the CFD-DEM modeling [21–24]. Many successful applications have been achieved in simulating chemical reaction processes. The Cheng group implemented the CFD-DEM method into the commercial software FLUENT to simulate the fluid catalytic cracking (FCC) process in risers and downers [25–27]. Zhang et al. [28] simulated the gas-solid flow and methanol-to-olefins (MTO) reactions in a fluidized bed reactor using the CFD-DEM method. A number of open source and commercial codes are capable of doing the Eulerian-Lagrangian simulations for gas-solid flows, e.g. MFIX-DEM [29, 30], FLUENT with the DPM (Discrete Particle Method) and dense-phase DPM modules [31], Barracuda [32] and OpenFOAM [33, 34].

Several attempts have also been made to simulate the dispersed gas-liquid flows using the Eulerian-Lagrangian approach (also called bubble tracking model). Buwa et al. [35] simulated the dynamics of gas-liquid flows in a rectangular bubble column. Three-dimensional, unsteady simulations were performed to simulate the dynamic characteristics of the oscillating bubble

plume. Hu and Celik [36] simulated a partially aerated flat bubble column using the Eulerian-Lagrangian based large-eddy simulation method. The two-way coupling was achieved between the gas-liquid phases. Mattson and Mahesh [37] simulated the bubble coalescence using an Eulerian-Lagrangian approach. The liquid phase was described using the Eulerian large-eddy simulation method and the Lagrangian particle motion was solved with the equations relating the turbulent motion of the liquid to the forces on each discrete bubble. Gruber et al. [38] developed a four-way coupled Eulerian-Lagrangian method by integrating various bubble coalescence and breakup models.

1.2.3 Eulerian-Eulerian method

In the Eulerian-Eulerian approach, each phase is treated as a continuous medium inter-penetrating the other phase, and is represented by the macroscopic conservation equations, which are valid throughout the entire flow domain. This method is commonly known as the two-fluid model, or when more than two phases are considered, it is called the multi-fluid model [39]. This approach requires less computational effort than the Eulerian-Lagrangian approach. However, the discrete character of the dispersed phase is lost due to the averaging procedure. Appropriate closure models should be provided.

The two-fluid model has been widely used to simulate the gas-solid fluidized beds. To describe the solid properties, the kinetic theory of granular flow is usually employed [40]. Recently, Wang et al. [41, 42] applied the kinetic theory for granular flow of rough sphere to describe the particle collisions. The two-fluid model with kinetic theory of granular flow has been used by researchers for simulating the gas-solid flows, e.g. Asegehegn et al. [43], Cloete et al. [44] and Yusuf et al. [45].

The two-fluid model is also widely employed to simulated the gas-liquid flows. Most of the gas-liquid two-fluid simulations were carried out using single mean bubble size [46–49]. This assumption is usually reasonable in the homogeneous flow regime. To account for the bubble size distribution, many attempts have been made by coupling computational fluid dynamics with population balance model (CFD-PBM) to simulate the gas-liquid flows [50–54].

The Eulerian-based method is also used as the multi-fluid model for simulating the three-phase fluidized bed reactors and slurry bubble column reactors. Panneerselvam et al. [55] simulated a three-phase fluidized bed reactor using the Eulerian multi-fluid model. Hamidipour et al. [56] performed the full three-dimensional multiple-Euler simulations of gas-liquid-solid fluidized beds. Troshko and Zdravistch [57] simulated the slurry bubble column reactors for Fisher-Tropsch synthesis. The syngas-slurry systems were described by a two-phase Eulerian model. The slurry was assumed to be perfectly mixed. Wang et al. [58] simulated a gas-liquid-solid three-phase airlift loop reactor used for the biotreatment of toluene. The three-Euler model was used, i.e., the gas phase was the toluene waste gas, the mineral salt medium was the liquid phase and the solid phase was the immobilized biomass.

1.3 Objective and outline

The objective of this thesis is to apply the CFD method for simulating the gas-solid and gas-liquid flows in the chemical reactors. Numerical simulations are performed based on the two-fluid model. The two-fluid solvers are developed in the open-source CFD package OpenFOAM. This thesis is organized such that each chapter can be read independently of each other.

Chapter 2: the comprehensive theory on the two-fluid model is presented. The derivation of two-fluid model is illustrated by conditionally averaging the local instantaneous conservation equations. The model closures are provided for the interphase momentum transfer in the gas-solid and gas-liquid flows. The particle size distribution and population balance method are discussed. An overview on the two-phase turbulence is provided.

Chapter 3: a gas-solid two-fluid solver is implemented into OpenFOAM and validated by simulating two bubbling fluidized bed cases, i.e., one with uniform gas feed and the other with a central gas jet. The simulated results are compared against the experimental data from the literature. The effect of different discretization schemes is investigated for the convection terms of phase velocities and solid volume fraction.

Chapter 4: the hydrodynamics simulations with erosion modeling are performed to calculate the total erosion rates of the target tubes immersed in a fluidized bed. The two-fluid model is used to simulate the gas-solid flows. The monolayer kinetic energy dissipation model is used to calculate the erosion rates with the input of the hydrodynamic information. The influence of the wall boundary conditions on the simulated erosion rates is also investigated.

Chapter 5: numerical investigations of hydrodynamics and kinetic reactions in a fluidized bed methanation reactor are carried out by coupling methanation kinetics with the two-fluid flow model. A lab-scale fluidized bed methanation reactor is simulated with the test of various grids and drag force models. Simulation results of axial species concentrations are compared with experimental data found in the literature.

Chapter 6: the population balance equation (PBE) is implemented into OpenFOAM and coupled with a CFD solver based on the two-fluid model. The liquid phase turbulence is modelled based on the k-ε model and Reynolds stress model. Two cylindrical bubble columns operated at high superficial gas velocities are simulated using the CFD-PBM method.

Chapter 7: the summary and outlook are given in this chapter.

Literature

[1] D. Kunii, O. Levenspiel, Fluidization engineering, Butterworth-Heinemann, Stoneham, 1991.

[2] J. Werther, E. U. Hartge, Modeling of industrial fluidized-bed reactors, Industrial & Engineering Chemistry Research 43 (2004) 5593–5604.

[3] Y. Zheng, Y. Cheng, F. Wei, Y. Jin, CFD simulation of hydrodynamics in downer reactors, Chemical Engineering Communications 189 (2002) 1598–1610.

[4] J. R. Grace, A. A. Avidan, T. M. Knowlton, Circulating fluidized beds, Blackie Academic and Professional, London, 1997.

[5] N. Kantarci, F. Borak, K. O. Ulgen, Bubble column reactors, Process Biochemistry 40 (2005) 2263–2283.

[6] H. H. Hu, Direct simulation of flows of solid-liquid mixtures, International Journal of Multiphase Flow 22 (1996) 335–352.

[7] T. W. Pan, D. D. Joseph, R. Bai, R. Glowinski, V. Sarin, Fluidization of 1204 spheres: simulation and experiment, Journal of Fluid Mechanics 451 (2002) 169–191.

[8] Y. Pan, S. Banerjee, Numerical simulation of particle interactions with wall turbulence, Physics of Fluids 8 (1996) 2733–2755.

[9] Y. Pan, S. Banerjee, Numerical investigation of the effect of large particle on wall turbulence, Physics of Fluids 9 (1997) 3786–3807.

[10] N. G. Deen, S. H. L. Kriebitzsch, M. A. van der Hoef, J. A. M. Kuipers, Direct numerical simulation of flow and heat transfer in dense fluid-particle systems, Chemical Engineering Science 81 (2012) 329–344.

[11] C. W. Hirt, B. D. Nichols, Volume of Fluid (VOF) method for the dynamics of free boundaries, Journal of Computational Physics 39 (1981) 201–225.

[12] M. Sussman, P. Smereka, S. Osher, A level set approach for computing solutions to incompressible two-phase flow, Journal of Computational Physics 114 (1994) 146–159.

[13] G. Tryggvason, B. Bunner, A. Esmaeeli, D. Juric, N. Al-Rawahi, W. Tauber, J. Han, S. Nas, Y.-J. Janz, A front-racking method for the computations of multiphase flow, Journal of Computational Physics 169 (2001) 708–759.

[14] OpenCFD Ltd., OpenFOAM 2.1.1 User's Guide, UK (2012).

[15] T. Tsuji, T. Kawaguchi, T. Tanaka, Discrete particles simulation of two dimensional fluidized bed, Powder Technology 77 (1993) 79–87.

[16] H. P. Zhu, Z. Y. Zhou, R. Y. Yang, A. B. Yu, Discrete particle simulation of particulate systems: Theoretical developments, Chemical Engineering Science 62 (2007) 3378–3396.

[17] H. P. Zhu, Z. Y. Zhou, R. Y. Yang, A. B. Yu, Discrete particle simulation of particulate systems: A review of major applications and findings, Chemical Engineering Science 63 (2008) 5728–5770.

[18] K. W. Chu, B. Wang, A. B. Yu, A. Vince, CFD-DEM modelling of multiphase flow in dense medium cyclones, Powder Technology 193 (2009) 235–247.

[19] Z. Y. Zhou, S. B. Kuang, K. W. Chu, A. B. Yu, Discrete particle simulation of particle-fluid flow: model formulations and their applicability, Journal of Fluid Mechanics 661 (2010) 482–510.

[20] K. W. Chu, B. Wang, D. L. Xu, Y. X. Chen, A. B. Yu, CFD-DEM simulation of the gas-solid flow in a cyclone separator, Chemical Engineering Science 66 (2011) 834–847.

[21] M. J. V. Goldschmidt, G. G. C. Weijers, R. Boerefijn, J. A. M. Kuipers, Discrete element modelling of fluidised bed spray granulation, Powder Technology 138 (2003) 39–45.

[22] M. J. V. Goldschmidt, R. Beetstra, J. A. M. Kuipers, Hydrodynamic modelling of dense gas-fluidised beds: comparison and validation of 3D discrete particle and continuum models, Powder Technology 142 (2004) 23–47.

[23] M. Ye, M. A. V. der Hoef, J. A. M. Kuipers, A numerical study of fluidization behavior of Geldart A particles using a discrete particle model, Powder Technology 139 (2004) 129–139.

[24] N. G. Deen, M. V. S. Annaland, M. A. van der Hoef, J. A. M. Kuiper, Review of discrete particle modeling of fluidized beds, Chemical Engineering Science 62 (2007) 28–44.

[25] C. N. Wu, B. H. Yan, Y. Jin, Y. Cheng, Modeling and simulation of chemically reacting flows in gas-solid catalytic and non-catalytic processes, Particuology 8 (2010) 525–530.

[26] Y. Z. Zhao, Y. L. Ding, C. N. Wu, Y. Cheng, Numerical simulation of hydrodynamics in downers using a CFD-DEM coupled approach, Powder Technology 1999 (2010) 2–12.

[27] C. N. Wu, Y. Cheng, Y. L. Ding, Y. Jin, CFD-DEM simulation of gas-solid reacting flows in fluid catalytic cracking (FCC) process, Chemical Engineering Science 65 (2010) 542–549.

[28] Y. Q. Zhuang, X. M. Chen, Z. H. Luo, J. Xiao, CFD-DEM modeling of gas-solid flow and catalytic MTO reaction in a fluidized bed reactor, Computers and Chemical Engineering 60 (2014) 1–16.

[29] R. Garg, J. Galvin, T. W. Li, S. Pannala, Open-source MFIX-DEM software for gas-solids flows: Part I-Verification studies, Powder Technology 220 (2012) 122–137.

[30] T. W. Li, R. Garg, J. Galvin, S. Pannala, Open-source MFIX-DEM software for gas-solids flows: Part II-Validation studies, Powder Technology 220 (2012) 138–150.

[31] ANSYS Inc., ANSYS FLUENT Theory Guide Release 14.0, Southpointe, PA, USA (2011).

[32] CPFD Software, LLC. Barracuda 14.4 Released (2011).

[33] J. W. Su, Z. L. Gu, X. Y. Xu, Discrete element simulation of particle flow in arbitrarily complex geometries, Chemical Engineering Science 66 (2011) 6069–6088.

[34] J. Zhao, T. Shan, Coupled CFD-DEM simulation of fluid-particle interaction in geomechanics, Powder Technology 239 (2013) 248–258.

[35] V. V. Buwa, D. S. Deo, V. V. Ranade, Eulerian-Lagrangian simulations of unsteady gas-liquid flows in bubble columns, International Journal of Multiphase Flow 32 (2006) 864–885.

[36] G. Hu, I. Celik, Eulerian-Lagrangian based large-eddy simulation of a partially aerated flat bubble column, Chemical Engineering Science 63 (2008) 253–271.

[37] M. D. Mattson, K. Mahesh, A one-way coupled, Euler-Lagrangian simulation of bubble coalescence in a turbulent pipe flow, International Journal of Multiphase Flow 40 (2012) 68–82.

[38] M. C. Gruber, S. Radl, J. G. Khinast, Coalescence and break-up in bubble columns: Euler-Lagrange simulations using a stochastic approach, Chemie Ingenieur Technik 85 (2013) 1118–1130.

[39] M. Ishii, T. Hibiki, Thermo-fluid dynamics of two-phase flow, Springer, New York, 2006.

[40] D. Gidaspow, Multiphase flow and fluidization, 1st Edition, Academic Press, New York, 1994.

[41] S. Wang, Z. H. Hao, H. L. Lu, G. D. Liu, J. X. Wang, P. F. Xu, A bubbling fluidization model using kinetic theory of rough spheres, AIChE Journal 58 (2012) 440–455.

[42] S. Wang, G. D. Liu, H. Lu, L. Y. Sun, P. F. Xu, CFD simulation of bubbling fluidized beds using kinetic theory of rough sphere, Chemical Engineering Science 71 (2012) 185–201.

[43] T. W. Asegehegn, M. Schreiber, H. J. Krautz, Numerical simulation and experimental validation of bubble behavior in 2D gas-solid fluidized beds with immersed horizontal tubes, Chemical Engineering Science 66 (2011) 5410–5427.

[44] S. Cloete, S. T. Johansen, S. Amini, An assessment of the ability of computational fluid dynamic models to predict reactive gas-solid flows in a fluidized bed, Powder Technology 215-216 (2012) 15–25.

[45] R. Yusuf, B. Halvorsen, M. C. Melaaen, Eulerian-Eulerian simulation of heat transfer between a gas-solid fluidized bed and an immersed tube-bank with horizontal tubes, Chemical Engineering Science 66 (2011) 1550–1564.

[46] D. Zhang, N. G. Deen, J. A. M. Kuipers, Numerical simulation of the dynamic flow behavior in a bubble column: A study of closures for turbulence and interface forces, Chemical Engineering Science 61 (2006) 7593–7608.

[47] D. Law, F. Battaglia, T. J. Heindel, Model validation for low and high superficial gas velocity bubble column flows, Chemical Engineering Science 63 (2008) 4605–4616.

[48] M. V. Tabib, S. A. Roy, J. B. Joshi, CFD simulation of bubble column: an analysis of interphase forces and turbulence models, Chemical Engineering Journal 139 (2008) 589–614.

[49] K. Ekambara, M. T. Dhotre, CFD simulation of bubble column, Nuclear Engineering and Design 240 (2010) 963–969.

[50] P. Chen, J. Sanyal, M. P. Dudukovic, CFD modeling of bubble columns flows: implementation of population balance, Chemical Engineering Science 59 (2004) 5201–5207.

[51] T. F. Wang, J. F. Wang, Y. Jin, A CFD-PBM coupled model for gas-liquid flows, AIChE Journal 52 (2006) 125–140.

[52] R. Bannari, F. Kerdouss, B. Selma, A. Bannari, P. Proulx, Three-dimensional mathematical modeling of dispersed two-phase flow using class method of population balance in bubble columns, Computers and Chemical Engineering 32 (2008) 3224–3237.

[53] M. R. Bhole, J. B. Joshi, D. Ramkrishna, CFD simulation of bubble columns incorporating population balance modeling, Chemical Engineering Science 63 (2008) 2267–2282.

[54] K. Ekambara, K. Nandakumar, J. B. Joshi, CFD simulation of bubble column reactor using population balance, Industrial & Engineering Chemistry Research 47 (2008) 8505–8516.

[55] R. Panneerselvam, S. Savithri, G. D. Surender, CFD simulation of hydrodynamics of gas-liquid-solid fluidised bed reactor, Chemical Engineering Science 64 (2009) 1119–1135.

[56] M. Hamidipour, J. W. Chen, F. Larachi, CFD study on hydrodynamics in three-phase fluidized beds-Application of turbulence models and experimental validation, Chemical Engineering Science 78 (2012) 167–180.

[57] A. A. Troshko, F. Zdravistch, CFD modeling of slurry bubble column reactors for Fisher-Tropsch synthesis, Chemical Engineering Science 64 (2009) 892–903.

[58] X. Wang, X. Q. Jia, J. P. Wen, Transient CFD modeling of toluene waste gas biodegradation in a gas-liquid-solid three-phase airlift loop reactor by immobilized Pseudomonas putida, Chemical Engineering Journal 172 (2011) 735–745.

Chapter 2

Two-fluid modeling methodology

2.1 Two-fluid model formulation

The continuum mechanics is widely applied for analyzing two-phase flow. The two-phase flow is considered as the field that is subdivided into two single-phase regions with the moving interfaces between the phases. The standard single-phase conservation equations are valid for each sub-region with the appropriate jump and boundary conditions. In theory, a two-phase flow model can be formulated in terms of the local instantaneous variable. However, the mathematical difficulties in using the local instantaneous formulations may be insurmountable in many practical cases. Hence, the macroscopic two-fluid model is derived based on the local instantaneous equations using proper averaging methods.

2.1.1 Local instantaneous conservation equations

The local instantaneous formulation of the continuity equation for a single compressible fluid is written as:

$$\frac{\partial \rho}{\partial t} + \nabla \cdot (\rho \mathbf{U}) = 0 \tag{2.1}$$

where ρ is the density of a fluid, $\mathbf{U}$ is the fluid velocity.

The local instantaneous momentum conservation equation is written as

$$\frac{\partial}{\partial t}(\rho \mathbf{U}) + \nabla \cdot (\rho \mathbf{U}\mathbf{U}) = -\nabla p + \nabla \cdot \tau + \rho \mathbf{g} \tag{2.2}$$

where p is the pressure, τ is the viscous (or shear) stress tensor, $\mathbf{g}$ is the gravitational acceleration. The simplest rheological constitutive equation for τ is the one for an inviscid fluid, which is expressed as

$$\tau = 0 \tag{2.3}$$

For most fluids, the Newton's viscosity law is applied to describe the viscous stress. The generalized linearly viscous fluid has a constitutive equation as

$$\tau = \mu[\nabla \mathbf{U} + (\nabla \mathbf{U})^{\mathrm{T}}] - (\frac{2}{3}\mu - \lambda)(\nabla \cdot \mathbf{U})\mathbf{I} \tag{2.4}$$

where μ is the dynamic viscosity relating the viscous stress to the linear deformations and λ is the bulk viscosity relating the viscous stress to the volumetric deformations. Little is known about the bulk viscosity, since its effect is quite small in practice.

2.1.2 Conditional averaging technique

In order to derive the conservation equations of two-fluid model, the individual phases should be distinguished. This is achieved by conditioning the local equations so that contributions to the averaged conservation equation of one phase come only from regions which contain that particular phase [1]. The idea of conditioning is based on the work of Dopazo [2]. For the conditional averaging (sometimes called phase-weighted averaging), the governing equations are multiplied by a phase indicator function before standard averaging techniques are applied. The phase indicator function $I_\varphi(\mathbf{x}, t)$ is defined as

$$I_\varphi(\mathbf{x}, t) = \begin{cases} 1 & \text{if point } (\mathbf{x}, \, t) \text{ is in phase } \varphi \\ 0 & \text{otherwise} \end{cases} \tag{2.5}$$

The phase volume fraction is calculated as the probability of point $(\mathbf{x}, t)$ being in phase φ:

$$\alpha_\varphi = \overline{I_\varphi(\mathbf{x}, t)} \tag{2.6}$$

where the overbar represents the ensemble average. The ensemble average is more fundamental than time and volume average and does not have the time and space restrictions. This single ensemble averaging method has been used by Weller [3] and Rusche [4].

The conditional averaging rules for the differential operations and products are given as

$$\overline{I_\varphi \nabla \Phi} = \nabla(\alpha_\varphi \overline{\Phi}_\varphi) + \overbrace{\Phi_{I,\varphi} \mathbf{n}_{I,\varphi\phi}} \Sigma \tag{2.7}$$

$$\overline{I_\varphi \nabla \cdot \Phi} = \nabla \cdot (\alpha_\varphi \overline{\Phi}_\varphi) + \overbrace{\Phi_{I,\varphi} \cdot \mathbf{n}_{I,\varphi\phi}} \Sigma \tag{2.8}$$

$$\overline{I_\varphi \frac{\partial \Phi}{\partial t}} = \frac{\partial \alpha_\varphi \overline{\Phi}_\varphi}{\partial t} - \overbrace{\Phi_{I,\varphi} \mathbf{n}_{I,\varphi\phi} \cdot \mathbf{U}_{I,\varphi\phi}} \Sigma \tag{2.9}$$

$$\overline{I_\varphi \Phi} = \alpha_\varphi \overline{\Phi} \tag{2.10}$$

$$\overline{I_\varphi \Phi \Psi} = \alpha_\varphi \overline{\Phi}_\varphi \overline{\Psi}_\varphi + \alpha_\varphi \overline{\Phi'_\varphi \Psi'_\varphi} \tag{2.11}$$

where $\frown$ denotes a surface average and Σ is the local averaged interfacial area density.

2.1.3 Conditionally averaged phase continuity equations

The local instantaneous continuity equation is first multiplied by the phase indicator function I_φ, and then averaged as

$$\overline{I_\varphi \frac{\partial \rho}{\partial t}} + \overline{I_\varphi \nabla \cdot (\rho \mathbf{U})} = 0 \tag{2.12}$$

Applying the conditional averaging rules, we obtain

$$\frac{\partial (\alpha_\varphi \overline{\rho}_\varphi)}{\partial t} - \overbrace{\rho_{I,\varphi} \mathbf{n}_{I,\varphi\phi} \cdot \mathbf{U}_{I,\varphi\phi}} \Sigma + \nabla \cdot (\alpha_\varphi \overline{\rho_\varphi \mathbf{U}_\varphi}) + \overbrace{\rho_{I,\varphi} \mathbf{n}_{I,\varphi\phi} \cdot \mathbf{U}_{I,\varphi}} \Sigma = 0 \tag{2.13}$$

where $\rho_{I,\varphi}$ is the density of phase φ at the interface, $\mathbf{n}_{I,\varphi\phi}$ is the unit normal vector at the surface directing from phase φ into phase ϕ, $\mathbf{U}_{I,\varphi\phi}$ is the interface velocity with the direction from phase φ to phase ϕ, $\mathbf{U}_{I,\varphi}$ is the velocity of phase φ at the interface.

Eq.(2.13) can be further simplified by combing the two surface average terms and applying density weighted averaging to the term $\rho \mathbf{U}$:

$$\overline{\rho \mathbf{U}} = \overline{\rho}\, \overline{\mathbf{U}} + \overline{\rho' \mathbf{U}'} = \overline{\rho} \widetilde{\mathbf{U}} \tag{2.14}$$

leading to

$$\frac{\partial (\alpha_\varphi \overline{\rho}_\varphi)}{\partial t} + \nabla \cdot (\alpha_\varphi \overline{\rho}_\varphi \widetilde{\mathbf{U}}_\varphi) = \overbrace{\rho_{I,\varphi} \mathbf{n}_{I,\varphi\phi} \cdot (\mathbf{U}_{I,\varphi\phi} - \mathbf{U}_{I,\varphi})} \Sigma \tag{2.15}$$

The difference between the interface velocity $\mathbf{U}_{I,\varphi\phi}$ and the fluid velocity $\mathbf{U}_{I,\varphi}$ at the interface is called the interface propagation velocity. The product of the interface propagation velocity and the surface normal velocity can be expressed as the interface propagation speed S_φ to account for the interphase mass transfer. Applying the above simplification, the final form of the conditionally averaged continuity equation of phase φ is obtained as

$$\frac{\partial \alpha_\varphi \overline{\rho}_\varphi}{\partial t} + \nabla \cdot (\alpha_\varphi \overline{\rho}_\varphi \widetilde{\mathbf{U}}_\varphi) = \overbrace{\rho_{I,\varphi} S_\varphi} \Sigma \tag{2.16}$$

When the phase φ is assumed to be incompressible and no interfacial mass transfer occurs, the conditional averaged phase continuity equation becomes

$$\frac{\partial \alpha_\varphi}{\partial t} + \nabla \cdot (\alpha_\varphi \overline{\mathbf{U}}_\varphi) = 0 \tag{2.17}$$

2.1.4 Conditionally averaged phase momentum equations

The local instantaneous momentum equation is multiplied by the phase indicator function I_φ, and then averaged as

$$\overline{I_\varphi \frac{\partial(\rho \mathbf{U})}{\partial t}} + \overline{I_\varphi \nabla \cdot (\rho \mathbf{U}\mathbf{U})} = -\overline{I_\varphi \nabla p} + \overline{I_\varphi \nabla \cdot \tau} + \overline{I_\varphi \rho \mathbf{g}} \tag{2.18}$$

Using the conditional averaging rules for differential operations, we obtain

$$\frac{\partial(\alpha_\varphi \overline{\rho_\varphi \mathbf{U}_\varphi})}{\partial t} - \widehat{\rho_{I,\varphi} \mathbf{U}_{I,\varphi}(\mathbf{n}_{I,\varphi\phi} \cdot \mathbf{U}_{I,\varphi\phi})}\Sigma + \nabla \cdot (\alpha_\varphi \overline{\rho_\varphi \mathbf{U}_\varphi \mathbf{U}_\varphi}) + \widehat{\rho_{I,\varphi} \mathbf{U}_{I,\varphi}(\mathbf{n}_{I,\varphi\phi} \cdot \mathbf{U}_{I,\varphi})}\Sigma =$$
$$-\nabla(\alpha_\varphi \overline{p}_\varphi) - \widehat{p_{I,\varphi}\mathbf{n}_{I,\varphi\phi}}\Sigma + \nabla \cdot (\alpha_\varphi \overline{\tau}_\varphi) + \widehat{\tau_{I,\varphi} \cdot \mathbf{n}_{I,\varphi\phi}}\Sigma + \alpha_\varphi \overline{\rho}_\varphi \mathbf{g} \tag{2.19}$$

Combining the two interface average terms on the l.h.s and using the density-averaging method and the Reynolds stress term is $\widetilde{\mathbf{R}}_\varphi = \widetilde{\mathbf{U}''_\varphi \mathbf{U}''_\varphi}$, we obtain

$$\frac{\partial(\alpha_\varphi \overline{\rho}_\varphi \widetilde{\mathbf{U}}_\varphi)}{\partial t} + \nabla \cdot (\alpha_\varphi \overline{\rho}_\varphi \widetilde{\mathbf{U}}_\varphi \widetilde{\mathbf{U}}_\varphi) + \nabla \cdot (\alpha_\varphi \overline{\rho}_\varphi \widetilde{\mathbf{R}}_\varphi) =$$
$$-\nabla(\alpha_\varphi \overline{p}_\varphi) + \nabla \cdot (\alpha_\varphi \overline{\tau}_\varphi) + \alpha_\varphi \overline{\rho}_\varphi \mathbf{g} - \widehat{p_{I,\varphi}\mathbf{n}_{I,\varphi\phi}}\Sigma + \widehat{\tau_{I,\varphi} \cdot \mathbf{n}_{I,\varphi\phi}}\Sigma + \widehat{\rho_{I,\varphi}\mathbf{U}_{I,\varphi}S_\varphi}\Sigma \tag{2.20}$$

The surface average term of the instantaneous pressure p on the r.h.s of Eq.(2.20) can be decomposed into surface average and surface fluctuation:

$$\widehat{p_{I,\varphi}\mathbf{n}_{I,\varphi\phi}}\Sigma = \widehat{p_{I,\varphi}}\nabla\alpha_\varphi + \widehat{p^\sharp_{I,\varphi}\mathbf{n}_{I,\varphi\phi}}\Sigma \tag{2.21}$$

And using the following relations

$$\nabla(\alpha_\varphi \overline{p}_\varphi) = \alpha_\varphi \nabla \overline{p}_\varphi + (\nabla \alpha_\varphi)\overline{p}_\varphi \tag{2.22}$$

Finally, the conditionally averaged phase momentum equation is written as

$$\frac{\partial(\alpha_\varphi \overline{\rho}_\varphi \widetilde{\mathbf{U}}_\varphi)}{\partial t} + \nabla \cdot (\alpha_\varphi \overline{\rho}_\varphi \widetilde{\mathbf{U}}_\varphi \widetilde{\mathbf{U}}_\varphi) + \nabla \cdot (\alpha_\varphi \overline{\rho}_\varphi \widetilde{\mathbf{R}}_\varphi) = -\alpha_\varphi \nabla \overline{p}_\varphi + \nabla \cdot (\alpha_\varphi \overline{\tau}_\varphi) + \alpha_\varphi \overline{\rho}_\varphi \mathbf{g}$$
$$+\mathbf{M}_\varphi + \widehat{\rho_{I,\varphi}\mathbf{U}_{I,\varphi}S_\varphi}\Sigma \tag{2.23}$$

where $\mathbf{M}_\varphi$ accounts for the interfacial momentum transfer and $\widehat{\rho_{I,\varphi}\mathbf{U}_{I,\varphi}S_\varphi}\Sigma$ is the interfacial mass transfer term. The interfacial mass transfer term is usually ignored when there is no interphase mass transfer (e.g. phase change). The interfacial momentum transfer term is

$$\mathbf{M}_\varphi = -(\widehat{p_{I,\varphi}} + \overline{p}_\varphi)\nabla\alpha_\varphi - \widehat{p^\sharp_{I,\varphi}\mathbf{n}_{I,\varphi\phi}}\Sigma + \widehat{\tau_{I,\varphi} \cdot \mathbf{n}_{I,\varphi\phi}}\Sigma \tag{2.24}$$

The two phase pressures are usually assumed to be equal to the average pressure $\bar{p}$. For the incompressible fluid, the phase momentum equation can be written by diving the phase density $\bar{\rho}_\varphi$ as

$$\frac{\partial(\alpha_\varphi \overline{\mathbf{U}}_\varphi)}{\partial t} + \nabla \cdot (\alpha_\varphi \overline{\mathbf{U}}_\varphi \overline{\mathbf{U}}_\varphi) + \nabla \cdot (\alpha_\varphi \overline{\mathbf{R}}_\varphi) = -\frac{\alpha_\varphi \nabla \bar{p}}{\bar{\rho}_\varphi} + \frac{\nabla \cdot (\alpha_\varphi \bar{\tau}_\varphi)}{\bar{\rho}_\varphi} + \alpha_\varphi \mathbf{g} + \frac{\mathbf{M}_\varphi}{\bar{\rho}_\varphi} \quad (2.25)$$

Combing the Reynolds stress term and viscous shear stress term, we obtain

$$\frac{\partial(\alpha_\varphi \overline{\mathbf{U}}_\varphi)}{\partial t} + \nabla \cdot (\alpha_\varphi \overline{\mathbf{U}}_\varphi \overline{\mathbf{U}}_\varphi) = -\frac{\alpha_\varphi \nabla \bar{p}}{\bar{\rho}_\varphi} + \frac{\nabla \cdot (\alpha_\varphi \bar{\tau}_{\varphi,\text{eff}})}{\bar{\rho}_\varphi} + \alpha_\varphi \mathbf{g} + \frac{\mathbf{M}_\varphi}{\bar{\rho}_\varphi} \quad (2.26)$$

Due to the averaging procedure, the conditionally averaged equations for mass and momentum contain extra unknown terms which represent the effects of the interphase momentum transfer and the turbulent velocity fluctuations. These terms should be modeled in terms of known quantities. In the following sections, the closures for these terms will be given for the gas-solid and gas-liquid flows.

2.2 Gas-solid interphase momentum transfer

In the gas-solid flows, the drag force is usually considered to model the interphase momentum transfer terms in the momentum equations. The interphase momentum transfer term $\mathbf{M}_\varphi$ is expressed by the product of the interphase momentum transfer coefficient β and the slip velocity $(\mathbf{U}_g - \mathbf{U}_s)$. In the following, three typical drag models are presented for calculating the coefficient β.

2.2.1 Syamlal-O'Brien model

The Syamlal-O'Brien model was derived by converting the terminal velocity correlations in fluidized or settling beds [5]:

$$\beta = \frac{3}{4} C_D \frac{\alpha_g \alpha_s \rho_g}{V_r^2 d_\text{p}} |\mathbf{U}_g - \mathbf{U}_s| \quad (2.27)$$

$$C_D = \left(0.63 + 4.8\sqrt{\frac{V_r}{\text{Re}}}\right)^2 \quad (2.28)$$

$$V_r = 0.5\left[a - 0.06\text{Re} + \sqrt{(0.06\text{Re})^2 + 0.12\text{Re}(2b - a) + a^2}\right] \quad (2.29)$$

$$a = \alpha_g^{4.14}, \quad b = \begin{cases} 0.8\alpha_g^{1.28} & \alpha_g \leqslant 0.85 \\[2mm] \alpha_g^{2.65} & \alpha_g > 0.85 \end{cases} \quad (2.30)$$

$$\text{Re} = \frac{\rho_g d_\text{p} |\mathbf{U}_g - \mathbf{U}_s|}{\mu_g} \quad (2.31)$$

2.2.2 Gidaspow model

Gidaspow [6] adopted the Wen and Yu correlation for $\alpha_s < 0.2$ and the Ergun equation for $\alpha_s \geqslant 0.2$. The Ergun equations were derived using the packed-bed pressure drop data [7], whereas the Wen and Yu model was formulated based on the homogeneous expansion of fluidized beds [8]. This drag model was recommended for describing dense fluidized beds. The interphase momentum transfer coefficient is expressed as

$$
\beta = \begin{cases} \dfrac{3}{4} \dfrac{C_D \alpha_g \alpha_s \rho_g |\mathbf{U}_g - \mathbf{U}_s|}{d_{\mathrm{p}}} \alpha_g^{-2.65} & \alpha_s < 0.2 \\[3mm] 150 \dfrac{\mu_g \alpha_s^2}{\alpha_g^2 d_{\mathrm{p}}^2} + 1.75 \dfrac{\rho_g \alpha_s}{\alpha_g d_{\mathrm{p}}} |\mathbf{U}_g - \mathbf{U}_s| & \alpha_s \geqslant 0.2 \end{cases}
\tag{2.32}
$$

The drag coefficient C_D is calculated by

$$
C_D = \begin{cases} \dfrac{24}{\mathrm{Re}}[1 + 0.15(\mathrm{Re})^{0.687}] & \mathrm{Re} < 1000 \\[3mm] 0.44 & \mathrm{Re} \geqslant 1000 \end{cases}
\tag{2.33}
$$

where the particle Reynolds number Re is defined as

$$
\mathrm{Re} = \frac{\rho_g d_{\mathrm{p}} |\mathbf{U}_g - \mathbf{U}_s|}{\mu_g}
\tag{2.34}
$$

2.2.3 EMMS model

A promising approach for modeling the gas-solid drag force is the energy minimization multi-scale (EMMS) model proposed by Yang et al. [9]. The EMMS model was developed based on the multi-scale analysis of the mass and momentum balance in fluidized beds. The EMMS model assumes the flow consists of a particle cluster phase and its surrounding phase. The interphase momentum transfer coefficient is calculated as

$$
\beta = \begin{cases} \dfrac{3}{4} \dfrac{C_{\mathrm{D}} \alpha_g \alpha_s \rho_g |\mathbf{U}_g - \mathbf{U}_s|}{d_{\mathrm{p}}} C_{D0} \omega(\alpha_g) & \alpha_g > 0.74 \\[3mm] 150 \dfrac{\mu_g \alpha_s^2}{\alpha_g^2 d_{\mathrm{p}}^2} + 1.75 \dfrac{\rho_g \alpha_s}{\alpha_g d_{\mathrm{p}}} |\mathbf{U}_g - \mathbf{U}_s| & \alpha_g \leqslant 0.74 \end{cases}
\tag{2.35}
$$

$$
C_{D0} = \begin{cases} \dfrac{24}{\alpha_g \mathrm{Re}}[1 + 0.15(\alpha_g \mathrm{Re})^{0.687}] & \alpha_g \mathrm{Re} < 1000 \\[3mm] 0.44 & \alpha_g \mathrm{Re} \geqslant 1000 \end{cases}
\tag{2.36}
$$

$$\omega(\alpha_g) = \begin{cases} -0.5760 + \dfrac{0.0214}{4(\alpha_g - 0.7463) + 0.0044} & 0.74 \leqslant \alpha_g \leqslant 0.82 \\[3mm] -0.0101 + \dfrac{0.0038}{4(\alpha_g - 0.7789) + 0.0040} & 0.82 \leqslant \alpha_g \leqslant 0.97 \\[3mm] -31.8295 + 32.8295\alpha_g & \alpha_g > 0.97 \end{cases} \qquad (2.37)$$

2.3 Gas-liquid interphase momentum transfer

Generally, in the gas-liquid flows, the interfacial forces are divided into two categories: drag force and non-drag forces. The non-drag forces are the lift force, the virtual mass force, the turbulent dispersion force, and the wall lubrication force. The interphase momentum transfer term $\mathbf{M}_\varphi$ is calculated as

$$\mathbf{M}_\varphi = \mathbf{M}_D + \mathbf{M}_L + \mathbf{M}_{VM} + \mathbf{M}_{TD} + \mathbf{M}_{WL} \qquad (2.38)$$

2.3.1 Drag force

The drag force acting on a single bubble is resistant to the motion of a bubble through a fluid flow. Its direction is opposite to that of the flow velocity and the drag force increases with the relative velocity. The steady drag force on a single bubble is usually given as

$$\mathbf{F}_D = \frac{1}{2} C_D \rho_l \frac{\pi d_B^2}{4} |\mathbf{U}_l - \mathbf{U}_g|(\mathbf{U}_l - \mathbf{U}_g) \qquad (2.39)$$

where C_D is the drag coefficient, d_B is the bubble diameter. The inter-phase momentum transfer terms in the momentum equations due to the drag force are calculated as

$$\mathbf{M}_{g,D} = -\mathbf{M}_{l,D} = \frac{3}{4} C_D \frac{\alpha_g \rho_l}{d_B} |\mathbf{U}_l - \mathbf{U}_g|(\mathbf{U}_l - \mathbf{U}_g) \qquad (2.40)$$

The drag coefficient is related to many factors: the bubble shape, orientation with respect to the flow, flow parameters such as the bubble Reynolds number, the Eötvös number, turbulent level, and so on. Table 2.1 presents the different correlations of the drag coefficient. The following drag coefficients are only derived and valid for the single bubble systems. The drag coefficients for the single bubble systems can be directly used for the dilute bubble swarm, or some corrections should be introduced for the dense bubble swarms.

At high gas fractions, the drag force acting on a single bubble is influenced by its neighbouring bubbles, which is referred to as the swarm effect. The drag coefficient of bubbles in a swarm is usually related to that of a single bubble. Richardson and Zaki [10] conducted the pioneering work on the swarm effect by establishing the dependence of the relative velocity of solid particles in batch-fluidization and sedimentation experiments. Some other corrections were proposed by Griffith and Wallis [11], Bridge et al. [12], Marrucci [13], Davidson and Harrison [14], and Lockett and Kirkpatrick [15].

Table 2.1: Drag coefficient expressions

Author	Drag coefficient
Schiller & Naumann [16]	$C_D = \begin{cases} \dfrac{24}{\mathrm{Re}}\left[1 + 0.15(\mathrm{Re})^{0.687}\right] & \mathrm{Re} < 1000 \\[2ex] 0.44 & \mathrm{Re} \geqslant 1000 \end{cases}$
Dalla Valle [17]	$C_D = \left(0.63 + \dfrac{4.8}{\sqrt{\mathrm{Re}}}\right)^2$
White [18]	$C_D = C_\infty + \dfrac{24}{\mathrm{Re}} + \dfrac{1}{1 + \sqrt{\mathrm{Re}}} \quad 0 \leqslant \mathrm{Re} \leqslant 2 \times 10^5$
Moore [19]	$C_D = \dfrac{48}{\mathrm{Re}}\left(1 - \dfrac{2.21}{\mathrm{Re}^{0.5}}\right) + O(\mathrm{Re}^{-11/6})$
Ishii & Zuber [20]	$C_D = \dfrac{2}{3}\sqrt{\mathrm{Eo}}$
Grevskott et al. [21]	$C_D = \dfrac{5.645}{\mathrm{Eo}^{-1} + 2.835}$
Lain et al. [22]	$C_D = \begin{cases} \dfrac{16}{\mathrm{Re}} & \mathrm{Re} \leqslant 1.5 \\[2ex] \dfrac{14.9}{\mathrm{Re}^{0.78}} & 1.5 < \mathrm{Re} < 80 \\[2ex] \dfrac{48}{\mathrm{Re}}\left(1 - \dfrac{2.21}{\sqrt{\mathrm{Re}}}\right) + 1.86 \times 10^{-15}\mathrm{Re}^{4.756} & 80 \leqslant \mathrm{Re} < 1500 \\[2ex] 2.61 & 1500 \leqslant \mathrm{Re} \end{cases}$
Tsuchiya [23]	$C_D = \max\left[\dfrac{24}{\mathrm{Re}}(1 + 0.15\mathrm{Re}^{0.687}), \dfrac{8}{3}\dfrac{\mathrm{Eo}}{\mathrm{Eo} + 4}\right]$
Tomiyama [24]	$C_D = \dfrac{8}{3}\dfrac{\mathrm{Eo}(1 - \mathrm{E}^2)}{\mathrm{E}^{2/3}\mathrm{Eo} + 16(1 - \mathrm{E}^2)\mathrm{E}^{4/3}}F(\mathrm{E})^{-2}$ $\mathrm{E} = \dfrac{1}{1 + 0.163\mathrm{Eo}^{0.757}}$ $F(\mathrm{E}) = \dfrac{\sin^{-1}\sqrt{1 - \mathrm{E}^2} - \mathrm{E}\sqrt{1 - \mathrm{E}^2}}{1 - \mathrm{E}^2}$
Murray et al. [25]	$C_D = \begin{cases} \dfrac{24}{\mathrm{Re}} & \mathrm{Re} < 1 \\[2ex] \dfrac{24}{\mathrm{Re}}\left[1 + \dfrac{3.6}{\mathrm{Re}^{0.313}}\left(\dfrac{\mathrm{Re} - 1}{19}\right)^2\right] & 1 \leqslant \mathrm{Re} < 20 \\[2ex] \dfrac{24}{\mathrm{Re}}(1 + 0.15\mathrm{Re}^{0.687}) & 20 \leqslant \mathrm{Re} \end{cases}$

More recently, Rusche and Issa [26] introduced a correction function to account for the influence of gas holdup on the drag coefficient:

$$C_{D,swarm} = C_{D,\infty}(1 - \alpha_g)\Big(e^{3.64\alpha_g} + \alpha_g^{0.864}\Big)$$ (2.41)

where α_g is the gas holdup and $C_{D,\infty}$ is the single bubble drag coefficient. The correction function was derived by fitting the experimental data in the literature. This method was used by Behzadi et al. [27]. Ishii and Zuber [20] proposed a correction term $(1 - \alpha_g)^p$ and $p = 2$. Olmos et al. [28] tested different values of p. They recommended the higher values of p should be used when increasing the superficial gas velocity. Rampure et al. [29] used the corrections term $(1 - \alpha_g)^2$ for superficial gas velocities below 0.20 m/s and $(1 - \alpha_g)^4$ for higher superficial gas velocities. Simonnet et al. [30] proposed a drag coefficient based on the experimental data measured by using optical methods. However, the optical methods are only appropriate to the dilute bubbly flows. The direct numerical simulation method provides a good way to investigate the bubble swarms. Roghair et al. [31, 32] proposed a bubble swarm drag coefficient using the DNS:

$$C_{D,swarm} = C_{D,\infty}(1 - \alpha_g)\Big(1 + \frac{18}{\text{Eo}}\alpha_g\Big)$$ (2.42)

2.3.2 Lift force

The lift force is the perpendicular component of the hydrodynamic force relative to the flow direction. The lift coefficient is well known for a single bubble, but for bubbles in a turbulent plume uncertainty remains. Some authors set the coefficient to zero and some use it as a tuning parameter. Whether the lift force is significant or not is still open for debate.

The lift force on a single bubble is widely expressed as

$$\mathbf{F}_L = V_B \rho_l C_L \mathbf{U}_{slip} \times \omega_l$$ (2.43)

where V_B is the bubble volume, $\mathbf{U}_{slip}$ is the slip velocity between bubbles and liquid, $\mathbf{U}_{slip} = \mathbf{U}_l - \mathbf{U}_g$, ω_l is the vorticity of liquid, $\omega_l = \nabla \times \mathbf{U}_l$, C_L is the lift coefficient. The momentum transfer terms due to the lift force are calculated as

$$\mathbf{M}_{g,L} = -\mathbf{M}_{l,L} = \alpha_g \rho_l C_L (\mathbf{U}_l - \mathbf{U}_g) \times (\nabla \times \mathbf{U}_l)$$ (2.44)

For a single spherical particle, the lift coefficient is 0.5 [33]. For dilute bubble plumes and single bubbles, the lift coefficient is known to vary with bubble size and shape. Small bubbles tend to move towards the edge of a plume and larger bubbles tend to move towards the centre of a plume. Table 2.2 gives various correlations for the lift coefficient.

Table 2.2: Lift coefficient expressions

Author	Lift coefficient
Tomiyama [34]	$C_L = \begin{cases} \min\big[0.288\tanh(0.121\mathrm{Re}), f(\mathrm{Eo})\big] & \mathrm{Eo} < 4 \\ f(\mathrm{Eo}) & 4 \leqslant \mathrm{Eo} \leqslant 10 \\ -0.29 & \mathrm{Eo} \geqslant 10 \end{cases}$ $f(\mathrm{Eo}) = 0.00105\mathrm{Eo}^3 - 0.0159\mathrm{Eo}^2 - 0.0204\mathrm{Eo} + 0.474$
Tomiyama [35]	$C_L = \begin{cases} \min\big[0.288\tanh(0.121\mathrm{Re}), f(\mathrm{Eo_d})\big] & \mathrm{Eo_d} < 4 \\ f(\mathrm{Eo_d}) & 4 \leqslant \mathrm{Eo_d} \leqslant 10 \\ -0.29 & \mathrm{Eo_d} \geqslant 10 \end{cases}$ $f(\mathrm{Eo_d}) = 0.00105\mathrm{Eo_d}^3 - 0.0159\mathrm{Eo_d}^2 - 0.0204\mathrm{Eo_d} + 0.474$ $\mathrm{Eo_d} = \dfrac{\mathrm{Eo}}{\mathrm{E}^2}, \quad \mathrm{E} = \dfrac{1}{1 + 0.163\mathrm{Eo}^{0.757}}$
Tomiyama [24]	$C_L = \begin{cases} \min\big[0.288\tanh(0.121\mathrm{Re}), f(\mathrm{Eo_d})\big] & \mathrm{Eo_d} < 4 \\ f(\mathrm{Eo_d}) & 4 \leqslant \mathrm{Eo_d} \leqslant 10 \\ -0.29 & \mathrm{Eo_d} > 10 \end{cases}$ $f(\mathrm{Eo_d}) = 0.00105\mathrm{Eo_d}^3 - 0.0159\mathrm{Eo_d}^2 - 0.0204\mathrm{Eo_d} + 0.474$ $\mathrm{Eo_d} = \dfrac{\mathrm{Eo}}{\mathrm{E}^{2/3}}, \quad \mathrm{E} = \dfrac{1}{1 + 0.163\mathrm{Eo}^{0.757}}$
Legendre & Magnaudet [36]	$C_L = \sqrt{(C_L^{\mathrm{lowRe}})^2 + (C_L^{\mathrm{highRe}})^2}$ $\mathrm{Sr} = \dfrac{\mathrm{Re}_\nabla}{\mathrm{Re}}, \quad \mathrm{Re}_\nabla = \dfrac{\rho_l \omega_l d_B^2}{\mu_l}, \quad \omega_l = |\nabla \times \mathbf{U}_l|$ $C_L^{\mathrm{lowRe}} = \dfrac{6}{\pi^2}(\mathrm{ReSr})^{-1/2} J(\varepsilon)$ $C_L^{\mathrm{highRe}} = \dfrac{1}{2}\dfrac{1 + 16\mathrm{Re}^{-1}}{1 + 29\mathrm{Re}^{-1}}$ $\varepsilon = \sqrt{\dfrac{\mathrm{Sr}}{\mathrm{Re}}}, \quad J(\varepsilon) = \dfrac{2.255}{(1 + 0.2\varepsilon^{-2})^{3/2}}$
Mei [37]	$C_L = \begin{cases} 6.46 f & \mathrm{Re} < 40 \\ 6.46 \times 0.0524(\beta\mathrm{Re})^{1/2} & 40 < \mathrm{Re} < 100 \end{cases}$ $f = (1 - 0.3314\beta^{1/2})\mathrm{e}^{-0.1\mathrm{Re}} + 0.3314\beta^{1/2}$ $\beta = 0.5\dfrac{\mathrm{Re}_\nabla}{\mathrm{Re}}$

To account for the influence of phase fraction on the lift coefficient, Beyerlein et al. [38] analyzed phase fraction data for vertical upward flows. Their lift coefficient is expressed as

$$C_L = 1.65 \times 10^{-3} \overline{\alpha}_g^{-0.78} \tag{2.45}$$

where $\overline{\alpha}_g$ is the mean gas phase fraction in the pipe. However, the lift coefficient is correlated with the mean gas phase fraction. Clearly, the local value should be used. Behzadi et al. [27] proposed a correlation as

$$C_L = 6.51 \times 10^{-4} \alpha_g^{-1.2} \tag{2.46}$$

where α_g is the local gas phase fraction. It should be noted that the lift coefficient would tend to infinity when $\alpha_g \to 0$. This is avoided by limiting C_L by a finite value which is taken as 0.25.

2.3.3 Virtual mass force

The virtual mass force results from the effect that an accelerated particle always entrains a part of its surrounding fluid. The interphase momentum transfer terms due to the virtual mass force are expressed as

$$\mathbf{M}_{l,VM} = -\mathbf{M}_{g,VM} = C_{VM} \alpha_g \rho_l \left(\frac{D_g \mathbf{U}_g}{Dt} - \frac{D_l \mathbf{U}_l}{Dt} \right) \tag{2.47}$$

where $\dfrac{D_i}{D_t}$ is the total derivative:

$$\frac{D_i}{Dt} = \frac{\partial}{\partial t} + \mathbf{U}_i \cdot \nabla \tag{2.48}$$

For a single spherical particle, the coefficient of virtual mass force C_{VM} is assigned with the value of 0.5. For bubbles with changeable shapes, this value is generally lower. However, this value is usually neglected because there are hardly any reliable correlations. From the studies of Zhang et al. [39] the absolute value of the coefficient of the virtual mass force is very small in a bubbly flow.

2.3.4 Turbulent dispersion force

Gas bubbles move along fluctuating trajectories in a turbulent flow field, while they interact with turbulence-induced liquid vortex. These fluctuations can drive the gas bubbles apart. In the two-fluid model, this dispersion can be considered by introducing a force which is proportional to the gradient of gas phase fraction. The following formulation of the turbulent dispersion force proposed by Lopez de Bertodano [40] is widely used:

$$\mathbf{M}_{l,TD} = -\mathbf{M}_{g,TD} = -C_{TD} \rho_l k_l \nabla \alpha_g \tag{2.49}$$

The coefficient of the turbulent dispersion force C_{TD} is assumed to be in the range of 0.1-1.0 in many cases.

2.3.5 Wall lubrication force

Under certain circumstances, e.g. bubbly upflow in a vertical pipe, the dispersed phase is observed to concentrate in a region close to the wall, but not immediately adjacent to the wall. This effect may be modeled by introducing the wall lubrication force, which tends to push the dispersed phase away from the wall. The wall lubrication force along with the lift force has significant influence on the radial distribution of the gas phase at a two-phase flow in a pipe. The interphase momentum transfer terms due to the wall lubrication force are formulated as

$$\mathbf{M}_{l,WL} = -\mathbf{M}_{g,WL} = -C_{WL}\alpha_g\rho_l[\mathbf{U}_r - (\mathbf{U}_r \cdot \mathbf{n}_w)\mathbf{n}_w]^2\mathbf{n}_w \tag{2.50}$$

where C_{WL} is the coefficient of the wall lubrication force, $\mathbf{n}_w$ is the outward vector normal to the wall, and $\mathbf{U}_r$ is the relative velocity.

Antal et al. [41] computed the wall lubrication force coefficient C_{WL} as follows:

$$C_{WL} = \max\left(0, \frac{C_{W1}}{d_{\mathrm{B}}} + \frac{C_{W2}}{y_w}\right) \tag{2.51}$$

In the ANSYS CFX implementation the coefficients C_{W1} and C_{W2} have the default values of -0.01 and 0.05, respectively. y_w represents the distance to the nearest wall.

Tomiyama [34] modified Antal's model based on extensive experimental data measured in the glycerol-air system. The coefficient of wall lubrication force was defined as follows:

$$C_{WL} = C_{W3}\frac{d_B}{2}\left[\frac{1}{y_w^2} - \frac{1}{(D - y_w)^2}\right] \tag{2.52}$$

where D is the pipe diameter. The coefficient C_{W3} is a function of the Eötvös number Eo:

$$C_{W3} = \begin{cases} -0.933\mathrm{Eo} + 0.179 & 1 \leqslant \mathrm{Eo} \leqslant 5 \\ 0.00599\mathrm{Eo} - 0.187 & 5 < \mathrm{Eo} \leqslant 33 \\ 0.179 & 33 < \mathrm{Eo} \end{cases} \tag{2.53}$$

Frank et al. [42, 43] generalized Tomiyama's model, which has no dependence on pipe diameter, and it is given as

$$C_{WL} = C_{W3} \cdot \max\left\{0, \frac{1}{C_{WD}}\frac{1 - \dfrac{y_w}{C_{WC}d_{\mathrm{B}}}}{y_w\left(\dfrac{y_w}{C_{WC}d_{\mathrm{B}}}\right)^{p-1}}\right\} \tag{2.54}$$

The coefficient C_{W3} preserves the same dependence on Eötvös number as the Tomiyama model. $C_{WC} = 10$, $C_{WD} = 6.8$ and $p = 1.7$.

2.4   Particle size distribution

The polydispersity in multiphase flows is present in many industrial and environmental applications. The particles (e.g. gas bubble, liquid droplet and solid particle) in the flows may interact among themselves. They collide and aggregate together. They also can be broken up due to collisions or due to interaction with the continuous phase flow. In the two-fluid model, the interphase transfer terms need to be modeled considering the interfacial area density. The particle size distribution should be determined for the interfacial area density in the polydispersed multiphase flows. Population balance method is becoming a powerful tool to describe the particle size distribution.

2.4.1   Population balance equation

The particles can be characterized by time t, external coordinates $\mathbf{x}$, which denotes the spatial position of the particle, and a set of internal coordinates ϕ, which could include particle mass, size, composition, and temperature. The particle number density function $n(\mathbf{x}, \phi, t)$ is the number of the particle with property ϕ per volume at the position $\mathbf{x}$, which is also called particle distribution function (PDF) or particle number distribution function.

For the mono-variable or mono-dimensional case, the particle volume v is usually used to describe the particle property. Thus, the particle number density function is expressed as $n(\mathbf{x}, v, t)$. For the sake of simplicity, the position vector $\mathbf{x}$ is not written in the subsequent sections. The population balance equation for the particle number density function in a computational cell is generally written as [44]

$$
\begin{aligned}
\frac{\partial n(v,t)}{\partial t} + \nabla \cdot \Big[\mathbf{U}_p(v,t)n(v,t) \Big] = \frac{1}{2} \int_0^v & c(v-v',v')n(v-v',t)n(v',t)dv' \\
& - \int_0^\infty c(v,v')n(v,t)n(v',t)dv' \\
& + \int_v^\infty \beta(v,v')b(v')n(v',t)dv' \\
& - b(v)n(v,t) \qquad (2.55)
\end{aligned}
$$

where the second term on the l.h.s. of Eq.(2.55) represents the change of particle number density due to the convection, $c(v_i, v_j)$ is the coalescence frequency, $b(v)$ is the breakup frequency of a fluid particle with size v, and $\beta(v,v')$ is the daughter particle size distribution.

Many solution methods are proposed for solving the population balance equation. The most obvious way is to carry out a discretization on the bubble size, similar to discretization in space and time. This leads into the so-called classes method [44–48]. The classes method is also called discrete method or sectional method. The main advantage of this method is that the particle size distribution can be directly obtained. However, to reflecting the reality, a large number of classes have to be used. Hence, the computational afford is very high to solve the discretized population balance equations with other conservation equations.

More recently, many attempts have been made to solve the population balance equation using the direct quadrature method of moments (DQMOM) [49–51]. The DQMOM was developed based on the quadrature method of moments (QMOM) [52]. The DQMOM avoids the time-consuming quadrature evaluation from the moments of the distribution.

2.4.2 Discretization of population balance equation

In the classes method, Eq.(2.55) is transformed into the continuity equation of every bubble class. The bubble size distribution is divided into a number of discrete size intervals. It is assumed that all the bubbles have the same size in a discrete size interval (v_i, v_{i+1}) and this size is represented by a pivot size x_i. The pivot size x_i does not equal to v_i or v_{i+1}. The bubble number density function can be given as

$$n(v,t) = \sum_{k=1}^{N-1} N_k(t)\delta(v - x_k) \tag{2.56}$$

and N_i is defined as the number of bubbles of volume between v_i and v_{i+1} per unit volume. It is calculated as:

$$N_i(t) = \int_{v_i}^{v_{i+1}} n(v,t)dv \tag{2.57}$$

When $v_i \to v_{i+1}$, $N_i(t)$ will be the number of bubble with volume v_i. In a computational cell with volume V, the number of bubbles with volumes between v_i and v_{i+1} is calculated as

$$N(t) = \int_V \int_{v_i}^{v_{i+1}} n(v,t)dvdV \tag{2.58}$$

Integrating Eq.(2.55) over each size interval (v_i, v_{i+1}), the discrete population balance equation can be expressed as

$$\frac{\partial N_i(t)}{\partial t} + \nabla \cdot \left[\mathbf{U}_b(t)N_i(t) \right] = \frac{1}{2} \int_{v_i}^{v_{i+1}} dv \int_0^v c(v - v', v')n(v - v', t)n(v', t)dv'$$
$$- \int_{v_i}^{v_{i+1}} n(v,t)dv \int_0^\infty c(v, v')n(v', t)dv'$$
$$+ \int_{v_i}^{v_{i+1}} dv \int_v^\infty \beta(v, v')b(v')n(v', t)dv'$$
$$- \int_{v_i}^{v_{i+1}} b(v)n(v,t)dv \tag{2.59}$$

We aim to obtain the dependent variable $N_i(t)$. However, the terms on the r.h.s. of Eq.(2.59) still contain $n(v,t)$ and the equation is not solvable. These terms should be represented by $N_i(t)$ to close this equation.

When the size of a formed bubble does not equal to v_i or x_i, the bubble should be redistributed to conserve the number and mass of the bubbles [47]. When the newly formed bubble volume is defined as v in the size range (x_i, x_{i+1}) and the number of the newly formed bubbles is assumed to be N, there will be $\Psi(v, x_i) \times N$ bubbles assigned to x_i and $\zeta(v, x_{i+1}) \times N$ bubbles assigned to x_{i+1}. There is a relationship to calculate the coefficients $\Psi(v, x_i)$ and $\zeta(v, x_{i+1})$:

$$\Psi(v, x_i)x_i + \zeta(v, x_{i+1})x_{i+1} = v \tag{2.60}$$

$$\Psi(v, x_i) + \zeta(v, x_{i+1}) = 1 \tag{2.61}$$

Eq.(2.59) can be rewritten by considering the bubble redistribution. After the reconstruction of the four terms, the discrete population balance equation is given as follows:

$$\frac{dN_i(t)}{dt} + \nabla \cdot \left[\mathbf{U}_b(t) N_i(t) \right] = \sum_{\substack{j,k \\ x_{i-1} \leqslant (x_j + x_k) \leqslant x_{i+1}}}^{j \geqslant k} (1 - \frac{1}{2}\delta_{jk})\eta_{i,jk}c(x_j, x_k)N_j(t)N_k(t)$$

$$- N_i(t)\sum_{k=1}^{M} c(x_i, x_k)N_k(t)$$

$$+ \sum_{k=i}^{M} \gamma_{i,k}b(x_k)N_k(t)$$

$$- b(x_i)N_i(t) \tag{2.62}$$

with

$$\eta_{j,ik} = \begin{cases} \dfrac{x_{i+1} - v}{x_{i+1} - x_i} & x_i \leqslant v \leqslant x_{i+1} \\[2mm] \dfrac{v - x_{i+1}}{x_i - x_{i-1}} & x_{i-1} \leqslant v \leqslant x_i \end{cases} \tag{2.63}$$

$$\gamma_{i,k} = \int_{x_{i-1}}^{x_i} \frac{v - x_{i-1}}{x_i - x_{i-1}}\beta(v, x_k)dv + \int_{x_i}^{x_{i+1}} \frac{x_{i+1} - v}{x_{i+1} - x_i}\beta(v, x_k)dv \tag{2.64}$$

In the gas-liquid bubbly flows, the bubble number of class i and the gas holdup have the following relationship:

$$\alpha_g f_i = N_i x_i \tag{2.65}$$

where f_i is the volume fraction of class i in the gas holdup, and x_i is the volume of bubbles between v_i and v_{i+1}. The bubble population balance equation is finally expressed as follows:

$$\frac{\partial}{\partial t}(\alpha_g f_i) + \nabla \cdot (\alpha_g \mathbf{U}_{g,i} f_i) = \sum_{\substack{j,k \\ x_{i-1} \leqslant (x_j+x_k) \leqslant x_{i+1}}}^{j \geqslant k} (1 - \frac{1}{2}\delta_{jk})\eta_{i,jk}c(x_j,x_k)\frac{\alpha_g f_j}{x_j}\frac{\alpha_g f_k}{x_k}x_i$$

$$-\alpha_g f_i \sum_{k=1}^{M} c(x_i,x_k)\frac{\alpha_g f_k}{x_k}$$

$$+\sum_{k=i}^{M} \gamma_{i,k}b(x_k)\frac{\alpha_g f_k}{x_k}x_i$$

$$-b(x_i)\alpha_g f_i \quad (2.66)$$

The computational fluid dynamics-population balance model (CFD-PBM) coupled model combines the advantages of CFD to calculate the entire flow field and of the PBM to calculate the local bubble size distribution [53]. To reduce the computational time, the MUltiple SIze Group method (MUSIG) is widely applied in the commercial CFD codes like CFX [54]. This standard/homogeneous MUSIG method avoids solving the momentum equation for every bubble class. Only one common momentum equation is solved for all bubble size classes. It is assumed that all the bubble classes share the same velocity field. The concept of the MUSIG method is widely used, e.g. Chen et al. [55, 56], Olmos et al. [28, 57], Wang et al. [53, 58], and Bannari et al. [59]. However, the homogeneous MUSIG method fails to predict the phase distribution when the different bubble motions become important. The inhomogeneous MUSIG model was proposed [60–63]. In the inhomogeneous MUSIG model, the gas phase is divided into N velocity groups, where each velocity group has its own velocity field. And each velocity group is subdivided into M bubble classes.

2.4.3 Bubble kernel functions

2.4.3.1 Breakup mechanisms and models

The breakage of fluid particles in viscous and turbulent dispersions is influenced by the continuous-phase fluid dynamics, transport phenomena, and interfacial interactions. The breakage mechanisms can be classified into four main categories: (1) turbulent fluctuation and collision; (2) viscous shear stress force; (3) shearing-off process; (4) interface instability [64]. Some typical models for breakup frequency and daughter size distribution have been proposed by considering the above mechanisms.

Various models are developed based on turbulent fluctuation and collision. There are five criteria for this mechanism: (1) turbulent kinetic energy of the drop greater than a critical value [65]; (2) velocity fluctuation around the particle surface greater than a critical value [66–68]; (3) turbulent kinetic energy of the bombarding turbulent eddy greater than a critical value [69–71]; (4) inertial force of the bombarding turbulent eddy greater than the interfacial

force of the smallest daughter particle [72]; (5) the combination of the criterion (3) and (4) [73, 74].

2.4.3.2 Coalescence mechanisms and models

The bubble coalescence mechanism is considered more complex than the breakup process, since it is affected by the interactions of bubbles with the surrounding liquid and other bubbles. Three bubble coalescence criteria have been proposed: the film drainage model, the critical approach velocity model and the energy model [75]. In all cases, the bubbles should contact and collide to coalesce. The bubble collisions result from various relative velocities. The relative motion may be due to five mechanisms in the turbulent flows: (1) the mean velocity gradients in the flow; (2) the turbulent fluctuations in the surrounding fluid; (3) the different bubble rise velocities; (4) the bubbles captured in an eddy; (5) the wake interactions. Since not all bubble collisions result in the coalescence, the coalescence efficiency should be used. The coalescence frequency is determined with the collision frequency and coalescence efficiency. A detailed literature review has been made by Liao and Lucas [75].

Considerable effort has been made on the modeling of the coalescence frequency. Some empirical or semi-empirical models with the adjustable parameters were developed, e.g. Casamatta et al. [76], Konno et al. [77], Wright et al. [78] and Kentish et al. [79]. However, the empirical models cannot be used for the general flows. Recently, some physical models of the coalescence frequency are developed by multiplying the collision frequency with the coalescence efficiency [70, 72, 80].

2.5 Two-phase turbulence modeling

In addition to the interphase momentum transfer terms, the two-fluid model requires closure relations for the Reynolds stresses in the phase momentum equations. These unknown stresses represent the effects of turbulence on the average phase momentum and need to be expressed in terms of known quantities.

2.5.1 Gas-solid turbulence modeling

The gas-solid turbulent flow is characterized by the fluctuating velocity of gas phase and solid phase. In the two-fluid model, the solid particle phase is considered to be a continuous fluid. Some researchers assumed that the laminar flows exist in both gas and solid phases, e.g. Chang et al. [81], Schreiber et al. [82], Passalacqua and Fox [83], and Verma et al. [84]. This assumption is reasonable in simulating the bubbling fluidized beds, since the superficial gas velocity is quite low in the bubbling fluidized beds.

For gas-solid flows with high Reynolds numbers, the gas-phase turbulence has a noticeable effect on the momentum and energy transfer between both phases. Bolio et al. [85] used the low Reynolds number k-ε model to account for the gas turbulence, while the solid phase was

assumed to be laminar. The particle-particle interactions were described by the kinetic theory of granular flow. Benavides and van Wachem [86] presented a general Eulerian framework the derivation of the averaged transport equations for turbulent gas-particle flows. The eddy viscosity in the gas phase was determined by solving a k-ε model. The solid viscosity was calculated using the kinetic theory of granular flow. Benavides and van Wachem [87] also simulated the turbulent gas-particle flow in a vertically oriented backward-facing step. The gas-phase turbulence was modeled by a k-ε model. The turbulence modification by the presence of solid particles were performed in the turbulence transport equations. The solid phase was modeled by the kinetic theory of granular flow including the models for describing the solid phase interactions with the gas phase.

Cheng et al. [88] simulated the hydrodynamics in downer reactors. The kinetic theory model coupled with the turbulence models of both gas phase and particle phase was proposed. The gas-phase turbulence was modeled by the standard k-ε model. The turbulent kinetic energy of particles was described by solving the turbulent kinetic energy equation of particle phase. This gas-solid turbulence modeling method was used by Zheng et al. [89] for simulating the hydrodynamics in riser reactors. Gryczka et al. [90] simulated the hydrodynamic behavior of a prismatic spouted bed apparatus using the Eulerian method. The turbulence in the gas phase was predicted with the modified k-ε model. The influence of the solid phase on the gas-phase turbulence was considered in the k-ε model. The turbulent quantities for the solid phase were calculated following Simonin and Viollet [91].

2.5.2   Gas-liquid turbulence modeling

2.5.2.1   Two equation k-ε turbulence models

In most cases, the single-phase standard k-ε model is used as a basis for the two-phase turbulence models. The k and ε transport equations of the continuous phase, i.e. the liquid phase, are written as follows:

$$\frac{\partial}{\partial t}(\alpha_l \rho_l k_l) + \nabla \cdot (\alpha_l \rho_l \mathbf{U}_l k_l) = \nabla \cdot \left[\alpha_l \big(\mu_l + \frac{\mu_{t,l}}{\sigma_k} \big) \nabla k_l \right] + \alpha_l G_{k,l} - \alpha_l \rho_l \varepsilon_l + S_{k,l} \qquad (2.67)$$

$$\frac{\partial}{\partial t}(\alpha_l \rho_l \varepsilon_l) + \nabla \cdot (\alpha_l \rho_l \mathbf{U}_l \varepsilon_l) = \nabla \cdot \left[\alpha_l \big(\mu_l + \frac{\mu_{t,l}}{\sigma_\varepsilon} \big) \nabla \varepsilon_l \right] + \alpha_l \frac{\varepsilon}{k} (C_{\varepsilon 1} G_{k,l} - C_{\varepsilon 2} \rho_l \varepsilon) + S_{\varepsilon,l} \quad (2.68)$$

The production of turbulent kinetic energy is calculated in its exact form:

$$G_{k,l} = \nabla \mathbf{U}_l : \tau_{\text{eff},l} \qquad (2.69)$$

$$\tau_{\text{eff},l} = \mu_{\text{eff},l} [\nabla \mathbf{U}_l + (\nabla \mathbf{U}_l)^{\text{T}}] - \frac{2}{3} \mu_{\text{eff},l} (\nabla \cdot \mathbf{U}_l) \mathbf{I} - \frac{2}{3} \rho_l k_l \mathbf{I} \qquad (2.70)$$

The source terms $S_{k,l}$ and $S_{\varepsilon,l}$ account for the influence of the presence of the dispersed phase on the liquid phase turbulence (i.e. bubble-induced turbulence). Modeling of bubble-induced turbulence in gas-liquid flows is still an unresolved issue. Some researchers neglected the

bubble-induced turbulence when simulating the gas-liquid flows, e.g. Ranade [92], Pfleger et al. [93], Sokolichin and Eigenberger [94], Buwa and Ranade [95] and Marschall et al. [96].

2.5.2.2 Reynolds stress transport model

The Reynolds stress transport model is also called the second-order or second-moment closure model. It is the highest level of turbulence closure currently feasible for practical applications. Launder et al. [97] developed a hierarchy of Reynolds stress transport models by consolidating the work of various groups into a unified framework. The Launder model has been one of the most widely used Reynolds stress models in engineering applications.

The transport equation of the Reynolds stress $R_{i,j} = \overline{u_i' u_j'}$ in the liquid phase is formulated as

$$\frac{\partial(\alpha_l \rho_l \mathbf{R}_l)}{\partial t} + \nabla \cdot (\alpha_l \rho_l \mathbf{U}_l \mathbf{R}_l) = \nabla \cdot \left[\alpha_l \big(\mu_l + \rho_l C_s \frac{k_l}{\varepsilon_l} \mathbf{R}_l \big) \nabla \mathbf{R}_l \right] + \alpha_l \rho_l \mathbf{P}_l + \alpha_l \rho_l \mathbf{\Phi}_l$$
$$- \frac{2}{3} \alpha_l \rho_l \varepsilon_l \mathbf{I} + \mathbf{S}_{R,l} \quad (2.71)$$

The molecular and turbulent transport term in the r.h.s of Eq.(2.71) is modeled with the general gradient diffusion hypothesis (GGDH) of Daly and Harlow [98].

The production rate of Reynolds stress is calculated in its exact form:

$$P_{ij} = -\left(\overline{u_i u_k} \frac{\partial u_j}{\partial x_k} + \overline{u_j u_k} \frac{\partial u_i}{\partial x_k} \right) \quad (2.72)$$

The pressure-strain correlation term $\mathbf{\Phi}_l$ is one of the most important terms, but most difficult one to model accurately. It is modeled according to Gibson and Launder [99], Fu et al. [100], and Launder [101, 102]:

$$\mathbf{\Phi}_l = \mathbf{\Phi}_1 + \mathbf{\Phi}_2 + \mathbf{\Phi}_w \quad (2.73)$$

where $\mathbf{\Phi}_1$ is the slow pressure-strain term, also known as the return-to-isotropy term, $\mathbf{\Phi}_2$ is called the rapid pressure-strain term, and $\mathbf{\Phi}_w$ is the wall-reflection term. The slow pressure-strain term is modeled as

$$\mathbf{\Phi}_1 = -C_1 \frac{\varepsilon_l}{k_l} \big(\mathbf{R}_l - \frac{2}{3} k_l \mathbf{I} \big) \quad (2.74)$$

The isotropization of production model is used for the rapid pressure-strain term:

$$\mathbf{\Phi}_2 = -C_2 \big(\mathbf{P}_l - \frac{1}{3} \text{tr}(\mathbf{P}_l) \mathbf{I} \big) \quad (2.75)$$

The wall-reflection term $\phi_{ij,w}$ is responsible for the redistribution of normal stresses near the wall. It tends to damp the normal stress perpendicular to the wall, while enhance the stresses parallel to the wall. This term is modeled as

$$\phi_{ij,w} = C_{1w}\frac{\varepsilon_l}{k_l}\left(\overline{u_k'u_m'}n_kn_m\delta_{ij} - \frac{3}{2}\overline{u_i'u_k'}n_kn_j - \frac{3}{2}\overline{u_j'u_k'}n_kn_i\right)\frac{C_\mu^{3/4}k_l^{3/2}}{\kappa\varepsilon_l d}$$
$$+C_{2w}\left(\phi_{km,2}n_kn_m\delta_{ij} - \frac{3}{2}\phi_{ik,2}n_kn_j - \frac{3}{2}\phi_{jk,2}n_kn_i\right)\frac{C_\mu^{3/4}k^{3/2}}{\kappa\varepsilon d} \tag{2.76}$$

where $C_{1w} = 0.5$, $C_{2w} = 0.3$, n_k is the x_k component of the unit normal to the wall, d is the normal distance to the wall, $C_\mu = 0.09$ and κ is the von Kármán constant ($\kappa = 0.4187$).

The fourth term in the r.h.s of Eq.(2.71) is modeled by assuming the isotropy of the small dissipative eddies and it only affects the normal Reynolds stresses. The source term $\mathbf{S}_{R,l}$ represents the influence of the bubbles on the Reynolds stress in the liquid phase.

The transport equation of the dissipation rate of turbulence kinetic energy is expressed as

$$\frac{\partial(\alpha_l\rho_l\varepsilon_l)}{\partial t} + \nabla\cdot(\alpha_l\rho_l\mathbf{U}_l\varepsilon_l) = \nabla\cdot\left[\alpha_l\left(\mu_l + \rho_lC_\varepsilon\frac{k_l}{\varepsilon_l}\mathbf{R}_l\right)\nabla\varepsilon_l\right] + \alpha_l\rho_l\frac{\varepsilon_l}{k_l}(C_{1\varepsilon}G_{k,l} - C_{2\varepsilon}\varepsilon_l) + S_{\varepsilon,l} \tag{2.77}$$

The Reynolds stress model constants are listed as $C_1 = 1.8$, $C_2 = 0.6$, $C_s = 0.22$, $C_{1\varepsilon} = 1.44$, $C_{2\varepsilon} = 1.92$, $C_\varepsilon = 0.15$.

2.5.2.3 Bubble-induced turbulence models

Generally, there are three approaches to account for the bubble-induced turbulence. One approach is to simply add an extra bubble-induced contribution to the effective viscosity. Sato and Sekoguchi [103] and Sato et al. [104] proposed the simplest model for the consideration of the bubble influence on the liquid turbulence. The bubble-induced viscosity is added to the laminar viscosity and shear-induced turbulent viscosity:

$$\mu_{\text{eff},l} = \mu_l + \mu_{t,l} + \mu_{B,l} \tag{2.78}$$

It is assumed that the bubble-induced turbulent viscosity is proportional to the local gas holdup and the slip velocity:

$$\mu_{B,l} = \rho_lC_{\mu,B}\alpha_gd_B|\mathbf{U}_g - \mathbf{U}_l| \tag{2.79}$$

where the model constant $C_{\mu,B}$ is set to 0.6. This model does not provide a direct value for the total turbulent kinetic energy which includes the contributions from both shear-induced and bubble-induced turbulence.

The second approach to model the bubble-induced turbulence is proposed by Arnold et al. [105] and Lahey et al. [106]. The total turbulence stress tensor is calculated as

$$\tau_{t,l} = \tau_{l,SI} + \tau_{l,BI} \tag{2.80}$$

The shear-induce turbulence stress tensor $\tau_{l,SI}$ can be modeled using the Boussinesq relation or by solving the Reynolds stress transport equation. The bubble-induced turbulence stress $\tau_{l,BI}$ is given as

$$\tau_{l,BI} = -\rho_l \mathbf{R}_{l,BI} = -\alpha_g \rho_l C_{\text{vm}} \Big[a(\mathbf{U}_r \otimes \mathbf{U}_r) + b(\mathbf{U}_r \cdot \mathbf{U}_r)\mathbf{I} \Big] \tag{2.81}$$

where $C_{\text{vm}} = 0.5$, $a = 1/10$ and $b = 3/10$. The bubble-induced turbulent kinetic energy is derived by taking the trace of the bubble-induced turbulence stress:

$$k_{l,BI} = \frac{1}{2}\text{tr}(\mathbf{R}_{l,BI}) = \frac{1}{2}\alpha_g C_{\text{vm}}|\mathbf{U}_g - \mathbf{U}_l|^2 \tag{2.82}$$

The total turbulent kinetic energy is calculated as

$$k_l = k_{l,SI} + k_{l,BI} \tag{2.83}$$

The third method is to introduce the bubble-induced source terms in the turbulence model equations. The influence of bubbles on the liquid phase turbulence is implicitly included. Various source terms have been proposed. Gosman et al. [107] incorporated the effects of the dispersed phase on turbulence with additional source terms in the k-ε equations. Oliveira and Issa [108] also used the similar bubble-induced source terms in the k-ε equations. The influence of gas-liquid interface on the liquid turbulence is modeled by Mudde and Simonin [109] as the source terms in the k-ε equations. The source term in the k-equation is from Bel F'Dhila and Simonin [110]. The source term in the ε-equation is from the work of Elghobashi and Abou-Arab [111]. In the commercial CFD software FLUENT, the so-called dispersed k-ε turbulence model describes the turbulence in the continuous phase by the modified k-ε equations with extra terms that include interphase turbulent momentum transfer. Selma et al. [112] incorporated the effect of the gas-liquid interface and the dispersed phase on the liquid turbulence.

Kataoka and Serizawa [113] proposed the source term in the k-equation which is proportional to the product of the drag force and the slip velocity between the two phases. This type of source term is widely used by other researchers, e.g. Olmos et al. [28], Pfleger and Beck [114], Le Moullec et al. [115], Mahmoodi et al. [116], Troshko and Hassan [117], Rzehak and Krepper [118, 119].

2.5.2.4 Dispersed phase turbulence modeling

The modeling of the dispersed phase turbulence was neglected by some researchers, e.g. Olmos et al. [28, 57], Pfleger et al. [93], Pfleger and Becker [114], Wang et al. [120], and van Baten and Krishna [121]. This assumption can be justified when the dilute dispersed phase exists. However, it is much less certain in the churn-turbulent flows with high gas fractions.

The eddy viscosity approach is also used for the dispersed phase turbulence. The Reynolds stress tensor of the dispersed phase is expressed as

$$-\overline{u'_d u'_d} = \nu_{t,d}\Big[\nabla\mathbf{U}_d + (\nabla\mathbf{U}_d)^{\mathrm{T}}\Big] - \frac{2}{3}\nu_{t,d}(\nabla \cdot \mathbf{U}_d)\mathbf{I} - \frac{2}{3}k_d\mathbf{I} \tag{2.84}$$

The disadvantage with the eddy viscosity approach is the need to formulate and solve the dispersed phase k-ε equations for calculating the dispersed phase eddy viscosity. To avoid this, some workers related the dispersed phase eddy viscosity to the continuous phase eddy viscosity by using the Peskin's formula [122], e.g. Pourshmadi [123], Pourahmadi and Humphrey [124], and Elghobashi and Abou-Arab [111, 125]. Simpler relations between the two phase eddy viscosities were proposed by Chen and Wood [126, 127]. The dispersed phase turbulent kinetic energy was also related to that of the continuous phase.

Politis [128] adopted the response coefficient C_t to relate the dispersed phase Reynolds stress with the continuous phase Reynolds stress. Rusche [4] calculated the turbulent kinetic energy and the effective viscosity of the dispersed phase by using the following expressions:

$$k_d = C_t^2 k_c \tag{2.85}$$

$$\nu_{\mathrm{eff},d} = \nu_d + C_t^2 \nu_{t,c} \tag{2.86}$$

Oliveira and Issa [108] also related the dispersed phase turbulent kinetic energy and viscosity to the continuous phase ones by means of the response functions:

$$k_d = C_t^2 k_c \tag{2.87}$$

$$\nu_{\mathrm{eff},d} = \nu_d + \nu_{t,c} \tag{2.88}$$

Simonin and his coworkers [109, 129] achieved the turbulent predictions of the dispersed bubble by an extension of Tchen's theory. The particle or bubble fluctuations are assumed to be driven by the surrounding continuous phase. In this way, the dispersed phase properties are algebraically related to the continuous phase properties. In the commercial CFD package FLUENT, the dispersed k-ε turbulence model also uses the Simonin's method to predict the turbulence in the dispersed phase.

Literature

[1] D. P. Hill, The computer simulation of dispersed two-phase flow, Ph.D. thesis, Imperial College of Science, Technology and Medicine, London, UK (1998).

[2] C. Dopazo, On conditional averages for intermittent turbulent flows, Journal of Fluid Mechanics 81 (1977) 433–438.

[3] H. G. Weller, Derivation, modeling and solution of the conditionally averaged two-phase flow equations, Tech. rep., OpenCFD Ltd. (2002).

[4] H. Rusche, Computational fluid dynamics of dispersed two-phase flows at high phase fractions, Ph.D. thesis, Imperial College of Science, Technology and Medicine, London, UK (2002).

[5] M. Syamlal, W. Rogers, T. J. OBrien, MFIX Documentation: Theory Guide; Technical Note DOE/METC-94/1004; U.S. Department of Energy (DOE), Morgantown Energy Technology Center: Morgantown, WV, USA (1993).

[6] D. Gidaspow, Multiphase flow and fluidization: Continuum and kinetic theory descriptions. Academic Press, Boston, 1994.

[7] S. Ergun, Fluid flow through packed columns, Chemical Engineering Progress 48 (1952) 89–95.

[8] C. Y. Wen, Y. H. Yu, Mechanics of fluidization, Chemical Engineering Progress Symposium Series 62 (1966) 100–111.

[9] N. Yang, W. Wang, W. Ge, L. N. Wang, J. H. Li, Simulation of heterogeneous structure in a circulating fluidized-bed riser by combining the two-fluid model with the EMMS approach, Industrial & Engineering Chemistry Research 43 (2004) 5548–5561.

[10] J. Richardson, W. Zaki, Sedimentation and fluidisation: part i, Transactions of the Institution of Chemical Engineers 32 (1954) 35–53.

[11] P. Griffith, G. Wallis, Two phase slug flow, ASME Transactions. Journal of Heat Transfer 83 (1961) 307–320.

[12] A. Bridge, L. Lapidus, J. Elgin, The mechanics of vertical gas-liquid fluidized system. Part I: countercurrent flow, AIChE Journal 10 (1964) 819–826.

[13] G. Marrucci, Rising velocity of a swarm of spherical bubbles, Industrial and Engineering Chemistry Research Fundamentals 4 (1965) 224–225.

[14] J. Davidson, D. Harrison, The behavior of a continuity bubbling fluidized bed, Chemical Engineering Science 21 (1966) 731–738.

[15] M. Lockett, R. Kirkpatrick, Ideal bubbly flow and actual flow in bubble columns, Transactions of the Institution of Chemical Engineers 53 (1975) 267–273.

[16] L. Schiller, Z. Naumann, Über die grundlegenden Berechnungen bei der Schwerkraftaufbereitung, Zeitschrift des Vereins Deutscher Ingenieure 77 (1935) 318–320.

[17] J. D. Valle, Micrometrics, Pitman Publishing Co., New York, 1948.

[18] F. M. White, Viscous fluid flow, McGraw-Hill, New York, 1974.

[19] D. Moore, The boundary layer on a spherical gas bubble, Journal of Fluid Mechanics 16 (1963) 161–176.

[20] M. Ishii, N. Zuber, Drag coefficient and relative velocity in bubbly, droplet or particulate flows, AIChE Journal 25 (1979) 843–855.

[21] S. Grevskott, B. H. Sannaes, M. P. Dudukovic, K. W. Hjarbo, H. F. Svendsen, Liquid circulation, bubble size distributions, and solids movement in two and three phase bubble columns, Chemical Engineerig Science 51 (1996) 1703–1713.

[22] S. Lain, D. Broder, M. Sommerfeld, M. F. Goz, Modelling hydrodynamics and turbulence in a bubble column using the Euler-Lagrange procedure, International Journal of Multiphase Flow 28 (2002) 1381–1407.

[23] K. Tsuchiya, A. Furumoto, L. S. Fan, J. P. Zhang, Suspension viscosity and bubble rise velocity in liquid-solid fluidized beds, Chemical Engineerig Science 52 (1997) 3053–3066.

[24] A. Tomiyama, Drag and lift and virtual mass forces acting on a single bubble. In: 3rd International Symposium on Two-Phase Flow Expressioning and Experimentation, Pisa, Italy, 2004.

[25] R. Murray, M. Omar, K. Joseph, O. Maitre, Statistical analysis of small bubble dynamics in isotropic turbulence, Physics of Fluids 19 (2007) 1–25.

[26] H. Rusche, R. Issa, The effect of voidage on the drag force on particles, droplets and bubbles in dispersed two-phase flow. In: Japanese European Two-Phase Flow Meeting, Tsukuba, Japan, 2000.

[27] A. Behzadi, R. Issa, H. Rusche, Modeling of dispersed bubble and droplet flow at high phase fractions, Chemical Engineering Science 59 (2003) 759–770.

[28] E. Olmos, C. Gentric, N. Midoux, Numerical description of flow regime transitions in bubble column reactors by a multiple gas phase model, Chemical Engineering Science 58 (2003) 2113–2121.

[29] M. R. Rampure, A. A. Kulkarni, V. V. Ranade, Hydrodynamics of bubble column reactors at high gas velocity: Experiments and Computational Fluid Dynamics (CFD) simulations, Industrial & Engineering Chemistry Research 46 (2007) 8431–8447.

[30] M. Simonnet, C. Gentric, E. Olmos, N. Midoux, Experimental determination of the drag coefficient in a swarm of bubbles, Chemical Engineerig Science 62 (2007) 858–866.

[31] I. Roghair, Y. M. Lau, N. G. Deen, H. M. Slagter, M. W. Baltussen, M. V. S. Annaland, J. A. M. Kuipers, On the drag force of bubbles in bubble swarms at intermediate and high Reynolds numbers, Chemical Engineerig Science 66 (2011) 3204–3211.

[32] I. Roghair, M. V. S. Annaland, J. A. M. Kuipers, Drag force and clustering in bubble swarms, AIChE Journal 59 (2013) 1791–1800.

[33] T. R. Auton, The lift on a spherical body in a rotational flow, Journal of Fluid Mechanics 183 (1987) 199–218.

[34] A. Tomiyama, Struggle with computational bubble dynamics, Multiphase Science and Technology 10 (1998) 369–405.

[35] A. Tomiyama, H. Tamaia, I. Zunb, S. Hosokawaa, Transverse migration of single bubbles in simple shear flows, Chemical Engineerig Science 57 (2002) 1849–1858.

[36] D. Legendre, J. Magnaudet, The lift force on a spherical bubble in a viscous linear shear flow, Journal of Fluid Mechanics 368 (1998) 81–126.

[37] R. Mei, An approximate expression for the shear lift force on a spherical particle at finite Reynolds number, International Journal of Multiphase Flow 18 (1992) 145–147.

[38] S. Beyerlein, R. Cossman, H. Richter, Prediction of bubble concentration profiles in vertical turbulent two-phase flow, International Journal of Multiphase Flow 11 (1985) 629–641.

[39] D. Zhang, N. G. Deen, J. A. M. Kuipers, Numerical simulation of the dynamic flow behavior in a bubble column: A study of closures for turbulence and interface forces, Chemical Engineerig Science 61 (2006) 7593–7608.

[40] M. A. L. de Bertodano, Turbulent bubbly two-phase flow data in a triangular duct, Ph.D. thesis, Rensselaer Polytechnic Institute, Troy, New York, USA (1992).

[41] S. P. Antal, R. T. Lahey, J. E. Flaherty, Analysis of phase distribution in fully developed laminar bubbly two-phase flow, International Journal of Multiphase Flow 17 (1991) 635–652.

[42] T. Frank, J. M. Shi, A. D. Burns, Validation of Eulerian multiphase flow models for nuclear safety applications. In: 3rd International Symposium on Two-Phase Flow Modelling and Experimentation, Pisa, Italy, 2004.

[43] T. Frank, P. J. Zwart, E. Krepper, H. M. Prasser, D. Lucas, Validation of CFD models for mono-and polydisperse air-water two-phase flows in pipes, Nuclear Engineering and Design 238 (2008) 647–659.

[44] D. Ramkrishna, Population Balances: Theory and Applications to Particulate Systems in Engineering, Academic Press, San Diego, CA, 2000.

[45] M. J. Hounslow, R. L. Ryall, V. R. Marshall, A discretized population balance for nucleation, growth, and aggregation, AIChE Journal 34 (1988) 1821–1832.

[46] J. D. Litster, D. J. Smit, M. J. Hounslow, Adjustable discretization population balance for growth and aggregation, AIChE Journal 41 (1995) 591–603.

[47] S. Kumar, D. Ramkrishna, On the solution of population balance equations by discretization-I. A fixed pivot technique, Chemical Engineering Science 51 (1996) 1311–1332.

[48] S. Kumar, D. Ramkrishna, On the solution of population balance equations by discretization-II. A moving pivot technique, Chemical Engineering Science 51 (1996) 1333–1342.

[49] D. L. Marchisio, R. O. Fox, Solution of the population balance equation using the direct quadrature method of moments, Journal of Aeorosol Science 36 (2005) 43–73.

[50] L. F. L. R. Silva, R. B. Damian, P. L. C. Lage, Implementation and analysis of numerical solution of the population balance equation in CFD packages, Computers and Chemical Engineering 32 (2008) 2933–2945.

[51] L. F. L. R. Silva, P. L. C. Lage, Development and implementation of a polydispersed multiphase flow model in OpenFOAM, Computers and Chemical Engineering 35 (2011) 2653–2666.

[52] R. McGraw, Description of the aerosol dynamics by the quadrature method of moments, Aerosol Science and Technology 27 (1997) 255–265.

[53] T. F. Wang, J. F. Wang, Y. Jin, A CFD-PBM coupled model for gas-liquid flows, AIChE Journal 52 (2006) 125–140.

[54] S. Lo, Application of population balance to CFD modelling of bubbly flow via the MUSIG model, Tech. rep., AEA Technology (1996).

[55] P. Chen, J. Sanyal, M. P. Dudukovic, CFD modeling of bubble columns flows: implementation of population balance, Chemical Engineering Science 59 (2004) 5201–5207.

[56] P. Chen, J. Sanyal, M. P. Dudukovic, Numerical simulation of bubble columns flows: effect of different breakup and coalescence closures, Chemical Engineering Science 60 (2005) 1085–1101.

[57] E. Olmos, C. Gentric, C. Vial, G. Wild, N. Midoux, Numerical simulation of multiphase flow in bubble column reactors. influence of bubble coalescence and break-up, Chemical Engineering Science 56 (2001) 6359–6365.

[58] T. F. Wang, J. F. Wang, Y. Jin, Population balance model for gas-liquid flows: Influence of bubble coalescence and breakup models, Industrial & Engineering Chemistry Research 44 (2005) 7540–7549.

[59] R. Bannari, F. Kerdouss, B. Selma, A. Bannari, P. Proulx, Three-dimensional mathematical modeling of dispersed two-phase flow using class method of population balance in bubble columns, Computers and Chemical Engineering 32 (2008) 3224–3237.

[60] T. Frank, P. J. Zwart, J.-M. Shi, E. Krepper, D. Lucas, U. Rohde, Inhomogeneous MUSIG model - a population balance approach for polydispersed bubbly flows. In: International Conference on Nuclear Energy for New Europe, Bled, Slovenia, 2005.

[61] E. Krepper, T. Frank, D. Lucas, H.-M. Prasser, P. J. Zwart, Inhomogeneous MUSIG model - a population balance approach for polydispersed bubbly flows. In: 6th International Conference on Multiphase Flow, Leipzig, Germany, 2007.

[62] E. Krepper, T. Frank, D. Lucas, H.-M. Prasser, P. J. Zwart, Inhomogeneous MUSIG model - a population balance approach for polydispersed bubbly flows. In: 12th International Topical Meeting on Nuclear Reactor Thermal Hydraulics, Pittsburgh, Pennsylvania, USA, 2007.

[63] E. Krepper, D. Lucas, T. Frank, H.-M. Prasser, P. J. Zwart, The inhomogeneous MUSIG model for the simulation of polydispersed flows, Nuclear Engineering and Design 238 (2008) 1690–1702.

[64] Y. Liao, D. Lucas, A literature review of theoretical models for drop and bubble breakup in turbulent dispersions, Chemical Engineering Science 64 (2009) 3389–3406.

[65] C. A. Coulaloglou, L. L. Tavlarides, Description of interaction processes in agitated liquid-liquid dispersions, Chemical Engineerig Science 32 (1977) 1289–1297.

[66] G. Narsimhan, J. P. Gupta, A model for transitional breakage probability of droplets in agitated lean liquid-liquid dispersions, Chemical Engineerig Science 34 (1979) 257–265.

[67] V. Alopaeus, J. Koskinen, K. I. Keskinen, Simulation of the population balances for liquid-liquid systems in a nonideal stirred tank. Part 1 Description and qualitative validation of the model, Chemical Engineering Science 54 (1999) 5887–5899.

[68] V. Alopaeus, J. Koskinen, K. I. Keskinen, J. Majander, Simulation of the population balances for liquid-liquid systems in a nonideal stirred tank. Part 2 Parameter fitting and the use of the multiblock model for dense dispersions, Chemical Engineerig Science 57 (2002) 1815–1825.

[69] C. H. Lee, L. E. Erickson, L. A. Glasgow, Bubble breakup and coalescence in turbulent gas-liquid dispersions, Chemical Engineering Communications 59 (1987) 65–84.

[70] M. J. Prince, H. W. Blanch, Bubble coalescence and break-up in air-sparged bubble columns, AIChE Journal 36 (1990) 1485–1499.

[71] H. Luo, H. F. Svendsen, Theoretical model for drop and bubble breakup in turbulent dispersions, AIChE Journal 42 (1996) 1225–1233.

[72] F. Lehr, M. Millies, D. Mewes, Bubble-size distributions and flow fields in bubble columns, AIChE Journal 48 (2002) 2426–2443.

[73] T. F. Wang, J. F. Wang, Y. Jin, A novel theoretical breakup kernel function for bubbles/droplets in a turbulent flow, Chemical Engineering Science 58 (2003) 4629–4637.

[74] H. Zhao, W. Ge, A theoretical bubble breakup model for slurry beds or three phase fluidized beds under high pressure, Chemical Engineerig Science 62 (2007) 109–115.

[75] Y. Liao, D. Lucas, A literature review on mechanisms and models for the coalescence process of fluid particles, Chemical Engineering Science 65 (2010) 2851–2864.

[76] G. Casamatta, A. Vogelpohl, Modeling of fluid dynamics and mass transfer in extraction columns, German Chemical Engineering 8 (1985) 96–103.

[77] M. Konno, T. Mutto, S. Saito, Coalescence of dispersed drops in an agitated tank, Journal of Chemical Engineering of Japan 21 (1988) 335–338.

[78] H. Wright, D. Ramkrishna, Factors affecting coalescence frequency of droplets in a stirred liquid-liquid dispersion, AIChE Journal 40 (1994) 767–776.

[79] S. E. Kentish, G. W. Stevens, H. R. C. Pratt, Estimation of coalescence and breakage rate constants within a Kuhni column, Industrial & Engineering Chemistry Research 37 (1998) 1099–1106.

[80] F. Lehr, D. Mewes, A transport equation for the interfacial area density applied to bubble columns, Chemical Engineering Science 56 (2001) 1159–1166.

[81] J. Chang, G. Wang, J. S. Gao, K. Zhang, H. G. Chen, Y. P. Yang, CFD modeling of particle-particle heat transfer in dense gas-solid fluidized beds of binary mixture, Powder Technology 217 (2012) 50–60.

[82] M. Schreiber, T. W. Asegehegn, H. J. Krautz, Numerical and experimental investigation of bubbling gas-solid fluidized beds with dense immersed tube bundles, Industrial & Engineering Chemistry Research 50 (2011) 7653–7666.

[83] A. Passalacqua, R. O. Fox, Implementation of an iterative solution procedure for multi-fluid gas-particle flow models on unstructured grids, Powder Technology 213 (2011) 174–187.

[84] V. Verma, N. G. Deen, J. T. Padding, J. A. M. Kuipers, Two-fluid modeling of three-dimensional cylindrical gas-solid fluidized beds using the kinetic theory of granular flow,

Chemical Engineerig Science 102 (2013) 227–245.

[85] E. J. Bolio, J. L. Sinclair, Gas turbulence modulation in the pneumatic conveying of massive particles in vertical tubes, International Journal of Multiphase Flow 21 (1995) 985–1001.

[86] A. Benavides, B. van Wachem, Numerical simulation and validation of dilute turbulent gas-particle flow with inelastic collisions and turbulence modulation, Powder Technology 182 (2008) 294–306.

[87] A. Benavides, B. van Wachem, Eulerian-Eulerian prediction of dilute turbulent gas-particle flow in a backward-facing step, International Journal of Heat and Fluid Flow 30 (2009) 452–461.

[88] Y. Cheng, Y. C. Guo, F. Wei, Y. Jin, W. Y. Lin, Modeling the hydrodynamics of downer reactors based on kinetic theory, Chemical Engineering Science 54 (1999) 2019–2027.

[89] Y. Zheng, X. T. Wan, Z. Qian, F. Wei, Y. Jin, Numerical simulation of the gas-particle turbulent flow in riser reactor based on k-ε-k_p-ε_p-θ two-fluid model, Chemical Engineering Science 56 (2001) 6813–6822.

[90] O. Gryczka, S. Heinrich, N. G. Deen, M. van Sint Annaland, J. A. M. Kuipers, M. Jacob, L. Mörl, Characterization and CFD-modeling of the hydrodynamics of a prismatic spouted bed apparatus, Chemical Engineering Science 64 (2009) 3352–3375.

[91] C. Simonin, P. L. Viollet, Predictions of an oxygen droplet pulverization in a compressible subsonic coflowing hydrogen flow, Numerical Methods for Multiphase Flows 91 (1990) 65–82.

[92] V. Ranade, Modeling of turbulent flow in a bubble column reactor, Chemical Engineering Research and Design 75 (1997) 14–23.

[93] D. Pfleger, S. Gomes, N. Gilbert, H. Wagner, Hydrodynamic simulations of laboratory scale bubble columns. Fundamental studies of the Eulerian-Eulerian modeling approach, Chemical Engineering Science 54 (1999) 5091–5099.

[94] A. Sokolichin, G. Eigenberger, Applicability of the standard k-ϵ turbulence model to the dynamic simulation of bubble columns: Part I. Detailed numerical simulations, Chemical Engineering Science 54 (1999) 2273–2284.

[95] V. V. Buwa, V. V. Ranade, Dynamics of gas-liquid flow in a rectangular bubble column: experiments and single/multi-group CFD simulations, Chemical Engineering Science 57 (2002) 4715–4736.

[96] H. Marschall, R. Mornhinweg, A. Kossmann, S. Oberhauser, K. Langbein, O. Hinrichsen, Numerical simulation of dispersed gas/liquid flows in bubble columns at high phase fractions using OpenFOAM. Part I: Modeling basics, Chemical Engineering & Technology 34 (2011) 1311–1320.

[97] B. Launder, G. Reece, W. Rodi, Progress in the development of a Reynolds-stress turbulence closure, Journal of Fluid Mechanics 68 (1975) 537–566.

[98] B. Daly, F. Harlow, Transport equations in turbulence, Physics of Fluids 13 (1970) 2634–2649.

[99] M. M. Gibson, B. E. Launder, Ground effects on pressure fluctuations in the atmospheric boundary layer, Journal of Fluid Mechanics 86 (1978) 491–511.

[100] S. Fu, B. E. Launder, M. A. Leschziner, Modeling strongly swirling recirculating jet flow with Reynolds-stress transport closures. In: 6th Symposium on Turbulent Shear Flows, Toulouse, France, 1987.

[101] B. E. Launder, Second-moment closure and its use in modeling turbulent industrial flows, International Journal for Numerical Methods in Fluids 9 (1989) 963–985.

[102] B. E. Launder, Second-moment closure: Present... and future?, International Journal of Heat and Fluid Flow 10 (1989) 282–300.

[103] Y. Sato, K. Sekoguchi, Liquid velocity distribution in two-phase bubble flow, International Journal of Multiphase Flow 2 (1975) 79–95.

[104] Y. Sato, M. Sadatomi, K. Sekoguchi, Momentum and heat transfer in two-phase bubble flow, International Journal of Multiphase Flow 7 (1981) 167–177.

[105] G. S. Arnold, D. A. Drew, R. T. Lahey, Derivation of constitutive equations for interfacial force and Reynolds stress for suspension of spheres using ensemble cell averaging, Chemical Engineering Communications 86 (1989) 43–54.

[106] R. T. Lahey, M. L. de Bertodano, O. C. Jones, Phase distribution in complex geometry conduits, Nuclear Engineering and Design 177 (1993) 177–201.

[107] A. D. Gosman, C. Lekakou, S. Politis, R. I. Issa, M. K. Looney, Multidimensional modeling of turbulent two-phase flows in stirred vessels, AIChE Journal 38 (1992) 1946–1956.

[108] P. J. Oliveira, R. I. Issa, Numerical aspects of an algorithm for the Eulerian simulation of two-phase flows, International Journal for Numerical Methods in Fluids 43 (2003) 1177–1198.

[109] R. F. Mudde, O. Simonin, Two- and three-dimensional simulations of a bubble plume using a two-fluid model, Chemical Engineering Science 54 (1999) 5061–5069.

[110] R. B. F'Dhila, O. Simonin, Eulerian prediction of a turbulent bubbly flow down-stream a sudden pipe expansion. In: 6th Workshop on Two-phase Flow Predictions, Erlangen, Germany, 1992.

[111] S. E. Elghobashi, T. W. Abou-Arab, A two-equation turbulence model for two-phase flows, Physics of Fluids 26 (1983) 931–938.

[112] B. Selma, R. Bannari, P. Proulx, A full integration of a dispersion and interface closures in the standard k-ε model of turbulence, Chemical Engineerig Science 65 (2010) 5417–5428.

[113] I. Kataoka, A. Serizawa, Basic equations of turbulence in gas-liquid two-phase flow, International Journal of Multiphase Flow 15 (1989) 843–855.

[114] D. Pfleger, S. Becker, Modelling and simulation of the dynamic flow behaviour in a bubble column, Chemical Engineering Science 56 (2001) 1737–1747.

[115] Y. L. Moullec, O. Potier, C. Gentric, J. P. Leclerc, Flow field and residence time distribution simulation of a cross-flow gas-liquid wastewater treatment reactor using CFD, Chemical Engineering Science 63 (2008) 2436–2449.

[116] B. Mahmoodi, M. R. K. Nikou, M. B. Bahrami, An assessment on the performance of Reynolds Stress Model (RSM) in modeling churn fully turbulent flow in bubble column reactors, International Journal of Computer Applications 39 (2012) 1–7.

[117] A. A.Troshko, Y. A. Hassan, A two-equation turbulence model of turbulent bubbly flows, International Journal of Multiphase Flow 27 (2001) 1965–2000.

[118] R. Rzehak, E. Krepper, Bubble-induced turbulence: Comparison of CFD models, Nuclear Engineering and Design 258 (2013) 57–65.

[119] R. Rzehak, E. Krepper, CFD modeling of bubble-induced turbulence, International Journal of Multiphase Flow 55 (2013) 138–155.

[120] S. K. Wang, S. J. Lee, O. C. Jones, R. T. Lahey, 3-D turbulence structure and phase distribution measurements in bubbly two-phase flows, International Journal of Multiphase Flow 13 (1987) 327–343.

[121] J. M. van Baten, R. Krishna, Eulerian simulations for determination of the axial dispersion of liquid and gas phases in bubble columns operating in the churn-turbulent regime, Chemical Engineering Science 56 (2001) 503–512.

[122] R. L. Peskin, The diffusivity of small suspended particles in turbulent fluid. In: AIChE National Meeting, Baltimore, Maryland, USA, 1962.

[123] F. Pourahmadi, Turbulence modelling of single and two-phase curved channel flows, Ph.D. thesis, University of California, Berkeley, USA (1982).

[124] F. Pourahmadi, J. A. Chumphrey, Modelling solid-fluid turbulent flows with application to predicting erosive wear, Physico-Chemical Hydrodynamics 43 (1983) 191–219.

[125] S. E. Elghobashi, T. W. Abou-Arab, M. Rizk, A. Mostafa, Prediction of the particle-laden jet with a two-equation turbulence model, International Journal of Multiphase Flow 10 (1984) 697–710.

[126] C. P. Chen, P. E. Wood, A turbulence closure model for dilute gas-particle flows, The Canadian Journal of Chemical Engineering 63 (1985) 349–360.

[127] C. P. Chen, P. E. Wood, Turbulence closure modeling of the dilute gas-particle axisymmetric jet, AIChE Journal 32 (1986) 163–166.

[128] S. Politis, Prediction of two-phase solid-liquid turbulent flow in stirred vessels, Ph.D. thesis, Imperial College of Science, Technology and Medicine, London, UK (1989).

[129] O. Simonin, Eulerian formulation for particle dispersion in turbulent two-phase flows. In: 5th Workshop on Two-Phase Flow Predictions, Erlangen, Germany, 1990.

Chapter 3

CFD modeling of gas-solid bubbling fluidized beds: Model validation and comparison of TVD differencing schemes

This chapter originates from the following publication:

Abstract

The two-fluid model with kinetic theory of granular flow is implemented into the open source CFD package OpenFOAM. The effect of total variation diminishing (TVD) convection schemes is investigated by simulating two bubbling fluidized beds. Five TVD schemes are employed to discretize the convection terms of phase velocity and solid volume fraction. Simulated results of the two test cases give reasonable agreement with the experimental data in the literature. For the discretization of the phase velocity convection terms, the five schemes give quite similar time-averaged radial profiles of particle axial velocity. The predicted bubbles in the bed with a central jet are not influenced by the different schemes. For the discretization of the solid volume fraction convection terms, the limitedLinear01, Sweby01 and vanLeer01 schemes give the converged and reasonable solutions, whereas the SuperBee01 and MUSCL01 schemes diverge the solutions. When using the faceLimited gradient scheme the convection scheme becomes more diffusive.

3.1 Introduction

The Eulerian-Eulerian two-fluid model is widely employed for computational fluid dynamics (CFD) simulations of the gas-solid flows, since it requires economical computational resources and enables large-scale reactor modeling. The two-fluid model treats gas and solid phases as fully interpenetrating continua, which typically involves two sets of averaged Navier-Stokes equations [1–3]. These governing equations are closed with the interfacial transfer models and the kinetic-frictional models for the description of granular phase [4–8].

Numerical solution of two-fluid model equations with kinetic theory of granular flow (KTGF) has been achieved with some commercial software, in-house programs and open source codes, e.g., FLUENT, CFX, MFIX and K-FIX. The commercial CFD packages FLUENT and CFX gain many practices in Eulerian-based modeling of gas-solid flows [9–14]. FLUENT uses a phase-coupled SIMPLE (Semi-Implicit Method for Pressure-Linked Equations) algorithm, while the inter-phase slip algorithm is adopted in CFX. The open source code MFIX (Multiphase Flow with Interphase eXchange) developed at National Energy Technology Laboratory is also widely applied for fluidized bed simulations [15–18]. MFIX is developed with staggered grid arrangement and Fortran coding. The MFIX manuals are well documented and freely available to researchers. The in-house program K-FIX and its alternate versions are employed by few researchers [19, 20]. The K-FIX source codes are not available to the public. Recently, the open source CFD code OpenFOAM (Open source Field Operation And Manipulation) [21] receives much more attention from academia and industry. In OpenFOAM the original gas-solid flow solvers with two-fluid model are not yet fully developed and validated [22]. To improve the solver accuracy and robustness, Passalacqua and Fox [23] proposed an iterative solution procedure to solve the two-fluid model equations.

OpenFOAM is developed based on the fundamental ideas of object orientation, layered software design and equation mimicking. Many CFD solvers for specialized applications have been implemented in OpenFOAM. Compared with the business software products, OpenFOAM offers the possibility to have insight into the source codes and hence it is of great convenience for code customization. Instead of the staggered grids, OpenFOAM adopts the co-located grids. The unstructured polyhedral cells can be deployed to handle complex geometries. The use of the object-oriented C++ language further makes users implement new models readily. OpenFOAM is becoming a flexible alternative tool for CFD simulation. However, the gas-solid flow simulations with OpenFOAM are still quite few.

Gas-solid flow simulation in a fluidized bed depends not only on the fundamental two-fluid model theory but also on the numerical techniques, i.e., time step, solution algorithm and discretization scheme. First, it is important to achieve the complete implementation of the two-fluid model with KTGF. While a robust gas-solid solver was developed and tested by Passalacqua and Fox [23], further experimental validations are still very necessary to confirm the applicability of OpenFOAM in simulating fluidized beds. Second, for the fluidized beds

with convection-dominated flows, great care should be taken to the discretization schemes of the convection terms. Guenther and Syamlal [24] compared the first-order upwind scheme with three second-order schemes (SMART, SuperBee and MINMOD) in the MFIX code. And the effect of convection scheme on the isolated bubble shape was investigated. Braun et al. [25] also simulated the bubble behaviors in a fluidized bed by using the MFIX code. The first-order upwind and SuperBee schemes were compared. Although various convection schemes are available in OpenFOAM, little attention is paid to the effect of convection scheme on the solution results of gas-solid flows in fluidized beds. It is of major importance to perform an in-depth comparison of convection schemes within the OpenFOAM framework. Such a study provides the guideline on the selection of convection schemes in the gas-solid flow modeling.

In this work a two-fluid solver is implemented into OpenFOAM. Experimental validations are performed by simulating two bubbling fluidized bed cases, i.e., one with uniform gas feed and the other with a central gas jet. The simulated results are compared against the experimental data from the literature. The effect of different convection schemes is investigated for the convection terms of phase velocities and solid volume fraction.

3.2 Mathematical models

The continuity equations of the gas and solid phases are written as

$$\frac{\partial(\alpha_g\rho_g)}{\partial t} + \nabla \cdot (\alpha_g\rho_g\mathbf{U}_g) = 0 \tag{3.1}$$

$$\frac{\partial(\alpha_s\rho_s)}{\partial t} + \nabla \cdot (\alpha_s\rho_s\mathbf{U}_s) = 0 \tag{3.2}$$

where ρ_g is the gas phase density, ρ_s is the solid phase density, $\mathbf{U}_g$ is the gas phase velocity, $\mathbf{U}_s$ is the solid phase velocity, α_g and α_s are the volumetric fractions of gas and solid phases, $\alpha_g = 1 - \alpha_s$. The momentum equations of the gas and solid phases are given as

$$\frac{\partial(\alpha_g\rho_g\mathbf{U}_g)}{\partial t} + \nabla \cdot (\alpha_g\rho_g\mathbf{U}_g\mathbf{U}_g) = -\alpha_g\nabla p + \nabla \cdot (\alpha_g\tau_g) + \beta(\mathbf{U}_s - \mathbf{U}_g) + \alpha_g\rho_g\mathbf{g} \tag{3.3}$$

$$\frac{\partial(\alpha_s\rho_s\mathbf{U}_s)}{\partial t} + \nabla \cdot (\alpha_s\rho_s\mathbf{U}_s\mathbf{U}_s) = -\alpha_s\nabla p - \nabla p_s + \nabla \cdot (\alpha_s\tau_s) + \beta(\mathbf{U}_g - \mathbf{U}_s) + \alpha_s\rho_s\mathbf{g} \tag{3.4}$$

where p is the bed pressure, p_s is the solid phase pressure, τ_g and τ_s are the stress tensors of gas and solid phases, β is the interphase momentum transfer coefficient, and $\mathbf{g}$ is the gravitational acceleration.

The gas phase is assumed as a Newtonian fluid, and its stress tensor is defined using the Newtonian stress-strain relation as

$$\tau_g = \mu_g\big[\nabla\mathbf{U}_g + (\nabla\mathbf{U}_g)^{\mathrm{T}}\big] - \frac{2}{3}\mu_g(\nabla \cdot \mathbf{U}_g)\mathbf{I} \tag{3.5}$$

where μ_g is the shear viscosity of gas phase and $\mathbf{I}$ is the unit tensor. Similarly, the shear stress tensor of solid phase is expressed as

$$\tau_s = \mu_s\big[\nabla\mathbf{U}_s + (\nabla\mathbf{U}_s)^{\mathrm{T}}\big] + \big(\lambda_s - \frac{2}{3}\mu_s\big)(\nabla\cdot\mathbf{U}_s)\mathbf{I} \tag{3.6}$$

where μ_s is the solid shear viscosity and λ_s is the solid bulk viscosity.

3.2.1 Interphase momentum transfer coefficient

In order to close the phase momentum equations, the interphase momentum transfer coefficient β should be calculated with the drag force functions. The majority of the reported drag models were empirically developed. No drag model is available for predicting a wide range of gas-solid flow types. In this work, the drag force function of Syamlal et al. [15] is applied for the fluidized bed with uniform gas feed. This function was derived by converting the terminal velocity correlations in fluidized or settling beds. The fluidized bed with a central jet is simulated with the drag model proposed by Gidaspow [26]. The Gidaspow model combines the Ergun equations [27] with the Wen and Yu model [28]. The Ergun equations were derived from the packed-bed pressure drop data, whereas the Wen and Yu model was formulated based on the homogeneous expansion of fluidized beds.
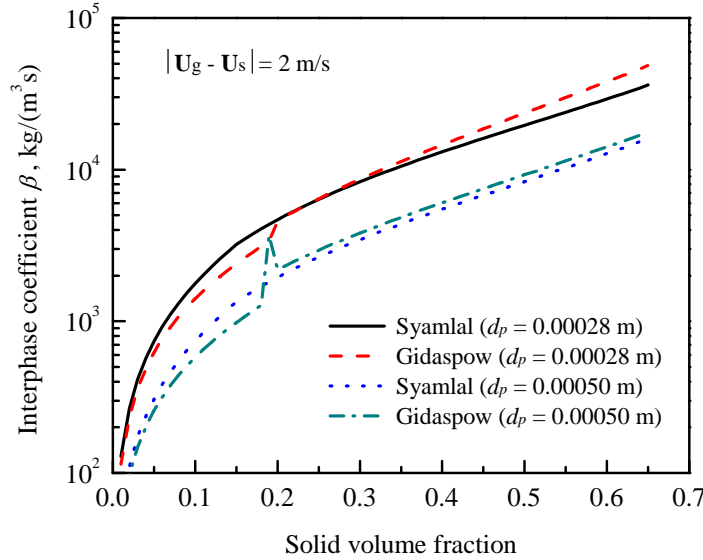
Figure 3.1: Comparison of different interphase momentum transfer coefficients

The drag correlations of the Syamlal and Gidaspow models are given in Table 3.1. Figure 3.1 shows the comparison between these models. At the high solid volume fractions, the values of β calculated with the Gidaspow model are larger than those calculated with the Syamlal model. Therefore, the Gidaspow model predicts stronger bed expansion and the predicted solid concentrations are smaller. Our preliminary study revealed that the fluidized bed with

uniform gas feed is better simulated using the Syamlal model. However, the Gidaspow model is needed to obtain the satisfactory predictions on the fluidized bed with a central jet.

Table 3.1: The interphase momentum transfer coefficients

(a) Syamlal model [15]

$$\beta = \frac{3}{4}C_D\frac{\alpha_g\alpha_s\rho_g}{V_r^2 d_\mathrm{p}}|\mathbf{U}_g - \mathbf{U}_s|$$

$$C_D = \left(0.63 + 4.8\sqrt{\frac{V_r}{\mathrm{Re}}}\right)^2$$

$$V_r = 0.5\left[a - 0.06\mathrm{Re} + \sqrt{(0.06\mathrm{Re})^2 + 0.12\mathrm{Re}(2b - a) + a^2}\right]$$

$$a = \alpha_g^{4.14}, b = \begin{cases} 0.8\alpha_g^{1.28}, & \alpha_g \leqslant 0.85 \\ \alpha_g^{2.65}, & \alpha_g > 0.85 \end{cases}$$

$$\mathrm{Re} = \frac{\rho_g d_\mathrm{p}|\mathbf{U}_g - \mathbf{U}_s|}{\mu_g}$$

(b) Gidaspow model [26]

$$\beta = \begin{cases} \dfrac{3}{4}\dfrac{C_\mathrm{D}\alpha_g\alpha_s\rho_g|\mathbf{U}_g - \mathbf{U}_s|}{d_\mathrm{p}}\alpha_g^{-2.65}, & \alpha_s < 0.2 \\ 150\dfrac{\mu_g\alpha_s^2}{\alpha_g^2 d_\mathrm{p}^2} + 1.75\dfrac{\rho_g\alpha_s}{\alpha_g d_\mathrm{p}}|\mathbf{U}_g - \mathbf{U}_s|, & \alpha_s \geqslant 0.2 \end{cases}$$

$$C_\mathrm{D} = \begin{cases} \dfrac{24}{\alpha_g\mathrm{Re}}[1 + 0.15(\alpha_g\mathrm{Re})^{0.687}], & \alpha_g\mathrm{Re} < 1000 \\ 0.44, & \alpha_g\mathrm{Re} \geqslant 1000 \end{cases}$$

3.2.2 Kinetic theory of granular flow

The properties of solid phase, i.e., solid shear stress τ_s and solid pressure p_s in Eq.(3.4), are derived based on the kinetic theory of granular flow [26]. For the kinetic theory of granular flow, the fluctuation energy of solid phase, also known as granular temperature, is obtained by solving the granular temperature transport equation which is expressed as follows:

$$\frac{3}{2}\left[\frac{\partial(\alpha_s\rho_s\Theta)}{\partial t} + \nabla \cdot (\alpha_s\rho_s\mathbf{U}_s\Theta)\right] = (-p_s\mathbf{I} + \tau_s) : \nabla\mathbf{U}_s + \nabla \cdot (\kappa_s\nabla\Theta) - \gamma_s + J_{vis} + J_{slip} \quad (3.7)$$

where Θ is the granular temperature, κ_s is the conductivity of granular temperature, γ_s is the dissipation rate due to particle collisions, J_{vis} is the dissipation rate resulting from viscous damping, and J_{slip} is the production rate due to the slip between gas and particle. These terms are modeled following Gidaspow [26].

47

The solid bulk viscosity λ_s and the solid shear viscosity μ_s are calculated according to Gidaspow [26]:

$$\lambda_s = \frac{4}{3}\alpha_s^2\rho_s d_\mathrm{p} g_0 (1+e)\sqrt{\frac{\Theta}{\pi}} \tag{3.8}$$

$$\mu_{s,\mathrm{KTGF}} = \frac{4}{5}\alpha_s\rho_s d_\mathrm{p} g_0 (1+e)\sqrt{\frac{\Theta}{\pi}} + \frac{10\rho_s d_s\sqrt{\Theta\pi}}{96\alpha_s g_0(1+e)}\left[1+\frac{4}{5}\alpha_s g_0(1+e)\right]^2 \tag{3.9}$$

where d_p is the particle diameter, e is the particle-particle restitution coefficient and g_0 is the radial distribution function. The solid phase pressure p_s is calculated following Lun et al. [5]:

$$p_s = \alpha_s\rho_s\Theta + 2\rho_s\alpha_s^2 g_0\Theta(1+e) \tag{3.10}$$

The expression for g_0 is given following Sinclair and Jackson [29]:

$$g_0 = \left[1 - \left(\frac{\alpha_s}{\alpha_{s,\mathrm{max}}}\right)^{1/3}\right]^{-1} \tag{3.11}$$

where $\alpha_{s,\mathrm{max}}$ is the particle packing limit.

3.2.3 Frictional stress models

In the regions where the particles are closely packed, the behavior of the granular flow is dominated by the frictional stresses and it is not adequately described only by KTGF. Similar to the solid kinetic stresses, the solid frictional stresses consist of the frictional shear stress and the frictional normal stress (i.e., solid frictional pressure). When the solid volume fraction exceeds a critical value $\alpha_{s,\mathrm{min}}$, the solid frictional stresses are usually added to the solid kinetic stresses calculated from KTGF [30]:

$$p_s = p_{s,\mathrm{KTGF}} + p_{s,\mathrm{f}}, \quad \mu_s = \mu_{s,\mathrm{KTGF}} + \mu_{s,\mathrm{f}} \tag{3.12}$$

The solid frictional pressure $p_{s,\mathrm{f}}$ proposed by Schaeffer [7] and the frictional shear viscosity $\mu_{s,\mathrm{f}}$ by Johnson et al. [30] are employed as

$$p_{s,\mathrm{f}} = F_r\frac{(\alpha_s - \alpha_{s,\mathrm{min}})^\mathrm{n}}{(\alpha_{s,\mathrm{max}} - \alpha_s)^\mathrm{p}} \tag{3.13}$$

$$\mu_{s,\mathrm{f}} = \frac{p_{s,\mathrm{f}}\sin\phi_\mathrm{f}}{2\sqrt{I_{2D}}} \tag{3.14}$$

where $F_r = 0.05\ \mathrm{N/m^2}$, $\mathrm{n} = 2$, $\mathrm{p} = 5$, ϕ_f is the internal frictional angle and $I_{2\mathrm{D}}$ represents the second invariant of the deviator of the strain rate tensor D_s:

$$I_{2\mathrm{D}} = \frac{1}{6}\left[(D_{s,11} - D_{s,22})^2 + (D_{s,22} - D_{s,33})^2 + (D_{s,11} - D_{s,33})^2\right] + D_{s,12}^2 + D_{s,23}^2 + D_{s,13}^2 \tag{3.15}$$

$$D_s = \frac{1}{2}\left[\nabla\mathbf{U}_s + (\nabla\mathbf{U}_s)^\mathrm{T}\right] \tag{3.16}$$

3.3 Numerical implementation

3.3.1 Discretization of the phase momentum equations

The gas and solid phases are assumed to be incompressible. Eqs. (3.3) and (3.4) are re-written by dividing the density of each phase:

$$\frac{\partial(\alpha_g \mathbf{U}_g)}{\partial t} + \nabla \cdot (\alpha_g \mathbf{U}_g \mathbf{U}_g) - \nabla \cdot (\alpha_g \nu_g \nabla \mathbf{U}_g) + \nabla \cdot (\alpha_g \mathrm{R}_g^C) = -\frac{\alpha_g}{\rho_g} \nabla p$$
$$+ \frac{\beta}{\rho_g}(\mathbf{U}_s - \mathbf{U}_g) + \alpha_g \mathbf{g} \qquad (3.17)$$

$$\frac{\partial(\alpha_s \mathbf{U}_s)}{\partial t} + \nabla \cdot (\alpha_s \mathbf{U}_s \mathbf{U}_s) - \nabla \cdot (\alpha_s \nu_s \nabla \mathbf{U}_s) + \nabla \cdot (\alpha_s \mathrm{R}_s^C) = -\frac{\alpha_s}{\rho_s} \nabla p - \frac{1}{\rho_s} \nabla p_s$$
$$+ \frac{\beta}{\rho_s}(\mathbf{U}_g - \mathbf{U}_s) + \alpha_s \mathbf{g} \qquad (3.18)$$

where ν is the kinematic viscosity, $\nu = \mu/\rho$. R_g^C and R_s^C are expressed as follows:

$$\mathrm{R}_g^C = -\nu_g(\nabla \mathbf{U}_g)^{\mathrm{T}} + \frac{2}{3}\nu_g(\nabla \cdot \mathbf{U}_g)\mathbf{I}$$

$$\mathrm{R}_s^C = -\nu_s(\nabla \mathbf{U}_s)^{\mathrm{T}} - \left(\frac{\lambda_s}{\rho_s} - \frac{2}{3}\nu_s\right)(\nabla \cdot \mathbf{U}_s)\mathbf{I}$$

The difficulty is found in the solution of the phase momentum equations, since the solid phase is not necessarily present in the whole computational domain of a bubbling fluidized bed. As a result, the discretized momentum equations result in the singular system of linear algebraic equations. Some workers suggested re-writing the phase momentum equations in the non-conservative or semi-conservative forms to avoid the singularity [31, 32]. Passalacqua and Fox [23] adopted the conservative forms of the phase momentum equations. In those computational cells with solid volume fraction lower than a specified minimum value, the discretized momentum equations were not solved.

The momentum conservative form is also adopted in our solver. As an example of the equation implementation in OpenFOAM, the transient term, convection term, diffusion term and divergence term in the l.h.s. of Eq.(3.18) are discretized with the following codes:

```
fvVectorMatrix UaEqn
(
    fvm::ddt(alpha,Ua)
  + fvm::div(alphaf*phia,Ua)
  - fvm::laplacian(alpha*nua,Ua)
  + fvc::div(alpha*Rca)
);
```

where `alpha` represents the solid volume fraction, `alphaf` is the interpolated face value of solid volume fraction, and `phia` is the particle velocity flux. The `fvm` operator returns the implicit discretization of the transient, convection and diffusion terms, while the divergence of `alpha*Rca` is explicitly discretized with the `fvc` operator. It is seen that the different terms in the C++ implementation mimics their mathematical counterparts.

By discretizing the transient, convection, diffusion and divergence terms in Eqs.(3.17) and (3.18) are discretized, the semi-discretized forms of the momentum equations are written as

$$A_g \mathbf{U}_g = \mathbf{H}_g - \frac{\alpha_g}{\rho_g} \nabla p + \frac{\beta}{\rho_g}(\mathbf{U}_s - \mathbf{U}_g) + \alpha_g \mathbf{g} \tag{3.19}$$

$$A_s \mathbf{U}_s = \mathbf{H}_s - \frac{\alpha_s}{\rho_s} \nabla p - \frac{1}{\rho_s} \nabla p_s + \frac{\beta}{\rho_s}(\mathbf{U}_g - \mathbf{U}_s) + \alpha_s \mathbf{g} \tag{3.20}$$

where A and $\mathbf{H}$ are accessed by using the member function `A()` and `H()` of the class `fvVectorMatrix`, respectively. The parameter A gives the diagonal coefficients of the velocity matrix. $\mathbf{H}$ represents the off-diagonal part of the velocity matrix and the source part.

The partial elimination algorithm proposed by Spalding [33] is adopted to decouple the momentum equations. The different velocities in Eqs.(3.19) and (3.20) are collected:

$$\mathbf{U}_g = \xi_g \left(\mathbf{H}_g - \frac{\alpha_g}{\rho_g} \nabla p + \alpha_g \mathbf{g} \right) + \xi_g \frac{\beta}{\rho_g} \mathbf{U}_s \tag{3.21}$$

$$\mathbf{U}_s = \xi_s \left(\mathbf{H}_s - \frac{\alpha_s}{\rho_s} \nabla p - \frac{1}{\rho_s} \nabla p_s + \alpha_s \mathbf{g} \right) + \xi_s \frac{\beta}{\rho_s} \mathbf{U}_g \tag{3.22}$$

with

$$\xi_g = \frac{1}{A_g + \max(\delta, \alpha_g \alpha_s)\dfrac{\beta^*}{\rho_g}}, \ \xi_s = \frac{1}{A_s + \max(\delta, \alpha_g \alpha_s)\dfrac{\beta^*}{\rho_s}}$$

where β^* is obtained by extracting $\alpha_g \alpha_s$ from β. In this study a small value ($\delta = 1 \times 10^{-4}$) is introduced into β to avoid the infinite values of ξ_g and ξ_s when $\alpha_s = 0$. Substituting $\mathbf{U}_s$ in Eq.(3.19) using Eq.(3.22) and $\mathbf{U}_g$ in Eq.(3.20) using Eq.(3.21), we obtain the decoupled momentum equations:

$$\mathbf{U}_g = \frac{\mathbf{H}_g}{A_g^*} + \frac{\xi_s \beta}{\rho_g A_g^*}\mathbf{H}_s - \left(\frac{\alpha_g}{\rho_g A_g^*} + \frac{\alpha_s \xi_s \beta}{\rho_g \rho_s A_g^*} \right)\nabla p - \frac{\xi_s \beta}{\rho_g \rho_s A_g^*}\nabla p_s + \left(\frac{\alpha_g}{A_g^*} + \frac{\alpha_s \xi_s \beta}{\rho_g A_g^*} \right)\mathbf{g} \tag{3.23}$$

$$\mathbf{U}_s = \frac{\mathbf{H}_s}{A_s^*} + \frac{\xi_g \beta}{\rho_s A_s^*}\mathbf{H}_g - \left(\frac{\alpha_s}{\rho_s A_s^*} + \frac{\alpha_g \xi_g \beta}{\rho_g \rho_s A_s^*} \right)\nabla p - \frac{1}{\rho_s A_s^*}\nabla p_s + \left(\frac{\alpha_s}{A_s^*} + \frac{\alpha_g \xi_g \beta}{\rho_s A_s^*} \right)\mathbf{g} \tag{3.24}$$

with

$$\mathrm{A}_g^* = \mathrm{A}_g - \frac{\beta}{\rho_g}\left(\xi_s\frac{\beta}{\rho_s} - 1\right), \ \mathrm{A}_s^* = \mathrm{A}_s - \frac{\beta}{\rho_s}\left(\xi_g\frac{\beta}{\rho_g} - 1\right)$$

3.3.2 Pressure equation and PISO algorithm

The PISO (Pressure Implicit with Split Operator) algorithm is adopted to handle the pressure-velocity coupling [34], where a pressure equation based on the volumetric continuity equation is solved to correct the predicted velocities. The velocity fluxes are obtained by calculating the dot-product of velocities in Eqs.(3.23) and (3.24) with face area vector $\mathbf{S}_f$:

$$\varphi_g = \left(\frac{\mathbf{H}_g}{\mathrm{A}_g^*}\right)_f \cdot \mathbf{S}_f + \left(\frac{\xi_s\beta}{\rho_g\mathrm{A}_g^*}\mathbf{H}_s\right)_f \cdot \mathbf{S}_f - \left(\frac{\alpha_g}{\rho_g\mathrm{A}_g^*} + \frac{\alpha_s\xi_s\beta}{\rho_g\rho_s\mathrm{A}_g^*}\right)_f |\mathbf{S}_f|\nabla^\perp p$$
$$-\left(\frac{\xi_s\beta}{\rho_g\rho_s\mathrm{A}_g^*}\right)_f (\nabla p_s)_f \cdot \mathbf{S}_f + \left(\frac{\alpha_g}{\mathrm{A}_g^*} + \frac{\alpha_s\xi_s\beta}{\rho_g\mathrm{A}_g^*}\right)_f \mathbf{g}\cdot\mathbf{S}_f \qquad (3.25)$$

$$\varphi_s = \left(\frac{\mathbf{H}_s}{\mathrm{A}_s^*}\right)_f \cdot \mathbf{S}_f + \left(\frac{\xi_g\beta}{\rho_s\mathrm{A}_s^*}\mathbf{H}_g\right)_f \cdot \mathbf{S}_f - \left(\frac{\alpha_s}{\rho_s\mathrm{A}_s^*} + \frac{\alpha_g\xi_g\beta}{\rho_g\rho_s\mathrm{A}_s^*}\right)_f |\mathbf{S}_f|\nabla^\perp p$$
$$-\left(\frac{1}{\rho_s\mathrm{A}_s^*}\right)_f (\nabla p_s)_f \cdot \mathbf{S}_f + \left(\frac{\alpha_s}{\mathrm{A}_s^*} + \frac{\alpha_g\xi_g\beta}{\rho_s\mathrm{A}_s^*}\right)_f \mathbf{g}\cdot\mathbf{S}_f \qquad (3.26)$$

Due to the volumetric conservation, the total volumetric flux is obtained as

$$\nabla \cdot \varphi = \nabla \cdot (\alpha_{g,f}\varphi_g + \alpha_{s,f}\varphi_s) = 0 \qquad (3.27)$$

From Eq.(3.27), the pressure equation can be derived as

$$\nabla \cdot \left\{\left[\alpha_{g,f}\left(\frac{\alpha_g}{\mathrm{A}_g^*\rho_g} + \frac{\alpha_s\xi_s\beta}{\rho_g\rho_s\mathrm{A}_g^*}\right)_f + \alpha_{s,f}\left(\frac{\alpha_s}{\mathrm{A}_s^*\rho_s} + \frac{\alpha_g\xi_g\beta}{\rho_s\rho_s\mathrm{A}_s^*}\right)_f\right]|\mathbf{S}_f|\nabla^\perp p\right\} = \nabla \cdot \varphi^\mathrm{o} \quad (3.28)$$

where φ^o is the total volumetric flux without the contribution of the pressure gradient and it is expressed as

$$\varphi^\mathrm{o} = \varphi_g^\mathrm{o} + \varphi_s^\mathrm{o} \qquad (3.29)$$

$$\varphi_g^\mathrm{o} = \left(\frac{\mathbf{H}_g}{\mathrm{A}_g^*}\right)_f \cdot \mathbf{S}_f + \left(\frac{\xi_s\beta}{\rho_g\mathrm{A}_g^*}\mathbf{H}_s\right)_f \cdot \mathbf{S}_f - \left(\frac{\xi_s\beta}{\rho_g\rho_s\mathrm{A}_g^*}\right)_f (\nabla p_s)_f \cdot \mathbf{S}_f + \left(\frac{\alpha_g}{\mathrm{A}_g^*} + \frac{\alpha_s\xi_s\beta}{\rho_g\mathrm{A}_g^*}\right)_f \mathbf{g}\cdot\mathbf{S}_f$$
$$(3.30)$$

$$\varphi_s^\mathrm{o} = \left(\frac{\mathbf{H}_s}{\mathrm{A}_s^*}\right)_f \cdot \mathbf{S}_f + \left(\frac{\xi_g\beta}{\rho_s\mathrm{A}_s^*}\mathbf{H}_g\right)_f \cdot \mathbf{S}_f - \left(\frac{1}{\rho_s\mathrm{A}_s^*}\right)_f (\nabla p_s)_f \cdot \mathbf{S}_f + \left(\frac{\alpha_s}{\mathrm{A}_s^*} + \frac{\alpha_g\xi_g\beta}{\rho_s\mathrm{A}_s^*}\right)_f \mathbf{g}\cdot\mathbf{S}_f$$
$$(3.31)$$

Once the pressure equation is solved, the velocity flux of each phase is corrected using the new pressure field:

$$\varphi_g = \varphi_g^o - \left(\frac{\alpha_g}{\rho_g A_g^*} + \frac{\alpha_s \xi_s \beta}{\rho_g \rho_s A_g^*} \right)_f \mid \mathbf{S}_f \mid \nabla^\perp p^n \tag{3.32}$$

$$\varphi_s = \varphi_s^o - \left(\frac{\alpha_s}{\rho_s A_s^*} + \frac{\alpha_g \xi_g \beta}{\rho_g \rho_s A_s^*} \right)_f \mid \mathbf{S}_f \mid \nabla^\perp p^n \tag{3.33}$$

Finally, the new velocity fields are reconstructed from the corrected face fluxes using the flux reconstruction method [23].

3.3.3 Discretization of the solid phase continuity equation

The boundedness of solid phase fraction is the key issue in the discretization of solid phase continuity equation. The phase fraction should be bounded between zero and one. Following the approach of Rusche [35], the boundedness is achieved by re-formulating the continuity equation as

$$\frac{\partial \alpha_s}{\partial t} + \nabla \cdot (\mathbf{U} \alpha_s) + \nabla \cdot (\alpha_g \mathbf{U}_r \alpha_s) = 0 \tag{3.34}$$

where $\mathbf{U}$ is the mixture velocity, $\mathbf{U} = \alpha_s \mathbf{U}_s + \alpha_g \mathbf{U}_g$, and $\mathbf{U}_r$ is the relative velocity, $\mathbf{U}_r = \mathbf{U}_s - \mathbf{U}_g$.

Special care should be taken on the discretization of the solid phase continuity equation, since the solid volume fraction should not exceed its physical maximum value. In MFIX, the effect of solid pressure is explicitly included in the solid phase continuity equation to obtain a solid volume fraction correction equation. This correction equation is solved using the local relaxation to avoid numerical instability [36]. However, this explicit approach is not always satisfactory [23]. To make the solid volume fraction below the packing limit, we implicitly include the solid pressure gradient in the solid phase continuity equation. The solid pressure gradient is expressed as the product of the elastic stress modulus $G(\alpha_s)$ and the gradient of solid volume fraction [37]:

$$\nabla p_s = G(\alpha_s) \nabla \alpha_s \tag{3.35}$$

$$G(\alpha_s) = \frac{\partial p_s}{\partial t} \tag{3.36}$$

Finally, the solid phase continuity equation is re-formulated as

$$\frac{\partial \alpha_s}{\partial t} + \nabla \cdot (\mathbf{U}^* \alpha_s) + \nabla \cdot (\alpha_g \mathbf{U}_r^* \alpha_s) - \nabla \cdot \left[\alpha_s \left(\frac{1}{\rho_s A_s^*} \right) G(\alpha_s) \nabla \alpha_s \right] = 0 \tag{3.37}$$

with

$$\mathbf{U}^* = \mathbf{U} + \alpha_s \Big(\frac{1}{\rho_s \mathrm{A}_s^*}\Big) G(\alpha_s)\nabla\alpha_s$$

$$\mathbf{U}_r^* = \mathbf{U}_r + \Big(\frac{1}{\rho_s \mathrm{A}_s^*}\Big) G(\alpha_s)\nabla\alpha_s$$

Eq.(3.37) is discretized with the class `fvScalarMatrix` as

```
fvScalarMatrix alphaEqn
(
    fvm::ddt(alpha)
  + fvm::div(phi,alpha)
  + fvm::div(-fvc::flux(-phir, beta), alpha)
  - fvm::laplacian(alphaf*ppMagf, alpha)
);
```

where `phi` is the flux of the mixture velocity, `phir` is the flux of the relative velocity, `ppMagf` is the face value of the term $G(\alpha_s)/(\rho_s \mathrm{A}_s^*)$, `beta` is gas phase volume fraction. The discretization of the Laplacian term is provided in Appendix A.

3.4 TVD differencing schemes

The finite volume method divides the spatial domain into a number of contiguous control volumes or cells (Figure 3.2). Dependent variables and other properties are stored at cell centers in OpenFOAM. For the face f connecting two cells, OpenFOAM designates an owner cell P and a neighbour cell N. The face area vector $\mathbf{S}_f$ is a vector normal to the face pointing out of the owner cell, whose magnitude is that of the face area. The vector $\mathbf{d}$ connects the centers of two adjacent cells.
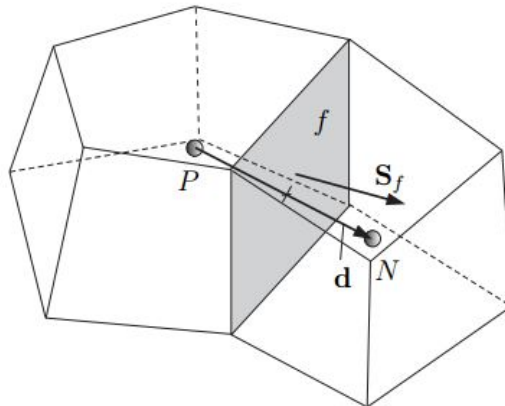
Figure 3.2: Geometric parameters of the control volumes

3.4.1 Discretization of convection terms

The discretization of convection terms in fluid transport equations has proven to be one of the most troublesome issues. The general convection term is integrated over a control volume after applying the Gauss theorem and linearized as follows:

$$\int_V \nabla \cdot (\rho \mathbf{U} \phi) dV = \int_S d\mathbf{S} \cdot (\rho \mathbf{U} \phi) \approx \sum_f \mathbf{S}_f \cdot (\rho \mathbf{U})_f \phi_f = \sum_f F_f \phi_f \qquad (3.38)$$

where ϕ is a dependent variable and F_f is the face flux, $F_f = \mathbf{S}_f \cdot (\rho \mathbf{U})_f$. The approximation of the face value ϕ_f from the cell-centered values is the key problem in the cell-centered finite volume discretization. Generally, the face value can be determined with the first-order upwind scheme and high-order convection schemes (linear and non-linear schemes). The central differencing scheme is an example of the high-order linear convection schemes (also called κ-schemes), while the flux limiter and normalized-variable approach are the two widely used non-linear high-order convection schemes [38].

For the central differencing (CD) scheme, the face value ϕ_f is calculated as

$$\phi_{f,CD} = f_{CD}\phi_P + (1 - f_{CD})\phi_N = f_{CD}(\phi_P - \phi_N) + \phi_N \qquad (3.39)$$

where f_{CD} is a weighting factor, $f_{CD} = \overline{fN}/\overline{PN}$. While the central differencing scheme is second-order accurate, this scheme causes unphysical spatial oscillations in the convection-dominated flows and thus violating the boundedness.

To maintain the boundedness the upwind differencing (UD) scheme determines the face value ϕ_f from the direction of the flow:

$$\phi_{f,UD} = f_{UD}(\phi_P - \phi_N) + \phi_N \qquad (3.40)$$

where the weighting factor f_{UD} equals to 1 if the flux $F_f > 0$ and 0 otherwise. The upwind scheme ensures the unconditional boundedness at the cost of accuracy by introducing numerical diffusion.

In an attempt to preserve the boundedness with reasonable accuracy, OpenFOAM provides the blended schemes by combining the upwind and central differencing schemes. The face value ϕ_f in the blended schemes is formulated as

$$\phi_f = (1 - \omega)\phi_{f,UD} + \omega \phi_{f,CD} \qquad (3.41)$$

where ω is a blending factor which determines how much numerical diffusion will be introduced. Clearly, $\omega = 0$ gives the upwind scheme and $\omega = 1$ results in the central differencing.

The discretized convection term along with the discretization of the transient, diffusion, and source terms generates the following linear equation system:

$$a_P \phi_P = \sum_N a_N \phi_N + S_P \tag{3.42}$$

where S_P is the source term from the transient term and the volume integral of the linearized source term. Jasak [39] pointed out that only the upwind scheme creates the diagonally equal matrix. The other convection schemes would create negative matrix coefficients in Eq.(3.42). The negative coefficients violate the diagonal equality and result in the unbounded solutions. In order to improve the matrix quality, Khosla and Rubin [40] proposed the deferred correction method to implement the high-order convection schemes. In this method, the part of the convection term corresponding to upwind differencing is implicitly built into the matrix, and the other part is added into the source term. At present, the deferred correction method is not available in the OpenFOAM package and is not used in this work.

3.4.2 TVD flux limiters in OpenFOAM

The blending factor ω in Eq.(3.41) can be evaluated in a face-by-face way based on total variation diminishing (TVD) [41, 42] or normalized variable diagram (NVD) [43, 44]. The TVD flux limiting procedure creates a differencing scheme which is higher than first-order accurate without the spurious oscillations. The NVD approach stabilizes the central differencing scheme and ensures the solution boundedness by introducing a small amount of numerical diffusion [39].

The TVD concept has proved to be the most promising method [39]. The performances of TVD schemes are preferentially evaluated in our gas-solid flow simulations. The blending factor ω (also called flux limiter in TVD method) requires the calculation of the variable r which represents the ratio of successive gradients of the interpolated variable. The TVD limiting scheme of the scalar fields calculates r as follows:

$$r = \begin{cases} 2\dfrac{\mathbf{d} \cdot (\nabla \phi)_P}{\phi_N - \phi_P} - 1 & F_f > 0 \\[3mm] 2\dfrac{\mathbf{d} \cdot (\nabla \phi)_N}{\phi_N - \phi_P} - 1 & F_f \leqslant 0 \end{cases} \quad \text{(scalar } \phi\text{)} \tag{3.43}$$

where $(\nabla \phi)_P$ is the full gradient calculated at the owner cell P. The discretization of gradient term is given in Appendix B.

When discretizing the vector fields, OpenFOAM adopts the V-scheme to maximize the limiting based on the worst-case direction where the steepest gradient exists [45]. The V-scheme is used by adding V to the name of a TVD scheme. The calculation of r for a vector field is expressed as

$$r = \begin{cases} 2\dfrac{(\phi_N - \phi_P) \cdot (\mathbf{d} \cdot (\nabla\phi)_P)}{(\phi_N - \phi_P) \cdot (\phi_N - \phi_P)} - 1 & F_f > 0 \\[3mm] 2\dfrac{(\phi_N - \phi_P) \cdot (\mathbf{d} \cdot (\nabla\phi)_N)}{(\phi_N - \phi_P) \cdot (\phi_N - \phi_P)} - 1 & F_f \leqslant 0 \end{cases} \quad (\text{vector } \phi) \tag{3.44}$$

To bound some scalar fields (e.g., α_s), the name of a scheme can be preceded by the word limited and followed with the lower bound and upper bound, respectively. This limited scheme uses the upwind differencing scheme ($\omega = 0$) when the value of ϕ in the cell is not between the lower bound and upper bound. For example, to bound the vanLeer scheme between -2 and 3, it is specified as limitedVanLeer -2.0 3.0. For the scalar fields commonly bounded between 0 and 1, the limited scheme is renamed as the 01-scheme and is used by adding 01 to the name of the scheme.

Table 3.2: The TVD flux limiters used in the present study

Flux limiter	Formulation	Reference
limitedLinear	$\omega = \max[\min(2r/k, 1), 0]\ \ 0 < k \leqslant 1$	OpenCFD Ltd.[21]
Sweby	$\omega = \max[0, \min(kr, 1), \min(r, k)]\ \ 0 < k \leqslant 2$	Sweby [42]
SuperBee	$\omega = \max[0, \min(2r, 1), \min(r, 2)]$	Roe [46]
vanLeer	$\omega = \frac{r+|r|}{1+|r|}$	van Leer [47]
MUSCL	$\omega = \max[\min(2r, 0.5r + 0.5, 2), 0]$	van Leer [48]
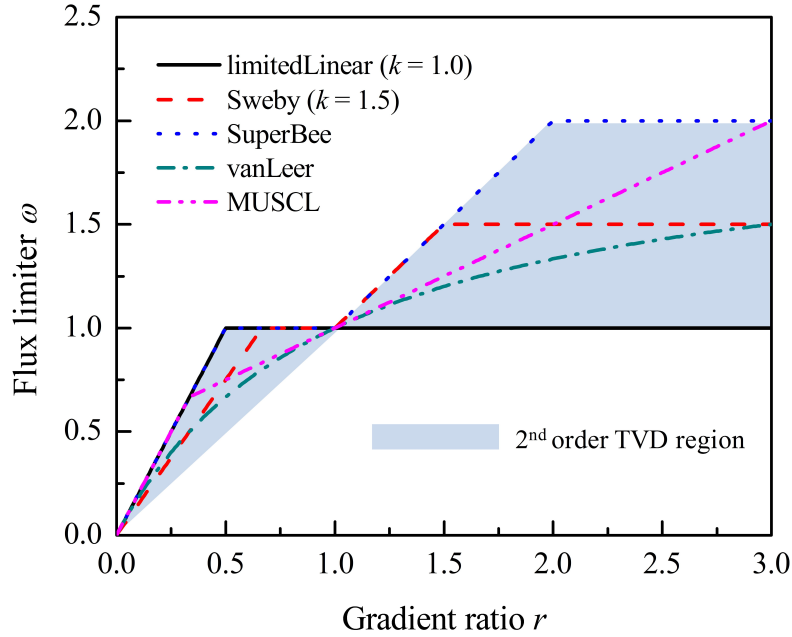
Figure 3.3: Profiles of five TVD flux limiters in the Sweby diagram

Five TVD flux limiters are formulated in Table 3.2 and also profiled in Figure 3.3. The limited-Linear scheme is an OpenFOAM invention and it is the stabilized central differencing scheme with a limiter. For the limiterLinear and Sweby schemes, the coefficient k is needed. When $k = 0$, the limitedLinear and Sweby schemes become the central differencing scheme. For the smooth variation ($r = 1$), all the TVD schemes degenerate the central differencing scheme. The Sweby, SuperBee, vanLeer and MUSCL schemes can use some downwinding, whereas the limitedLinear scheme only combines the upwind and central differencing schemes.

3.5 Test case descriptions

3.5.1 Experimental conditions

The fluidized bed setup with uniform gas feed (Figure 3.4a) is simulated which was experimentally studied by Taghipour et al. [49]. The bed material is made of spherical glass beads with a mean diameter of 2.8×10^{-4} m and a density of 2500 kg/m^3. The experiment started with a static bed height of 0.4 m and a solid volume fraction of 0.6. The bubbling fluidized bed with a central jet (Figure 3.4b) used by Gidaspow et al. [50] is also simulated which is filled with the particles having a mean diameter of 5.0×10^{-4} m. The initial bed height is up to 0.2922 m from the bottom. At the center of the bottom, a rectangular orifice of 0.0127 m $\times$ 0.0381 m allows a central jet into the bed, while the rest of the bottom is uniformly fed by air at the minimum fluidization velocity of 0.282 m/s.
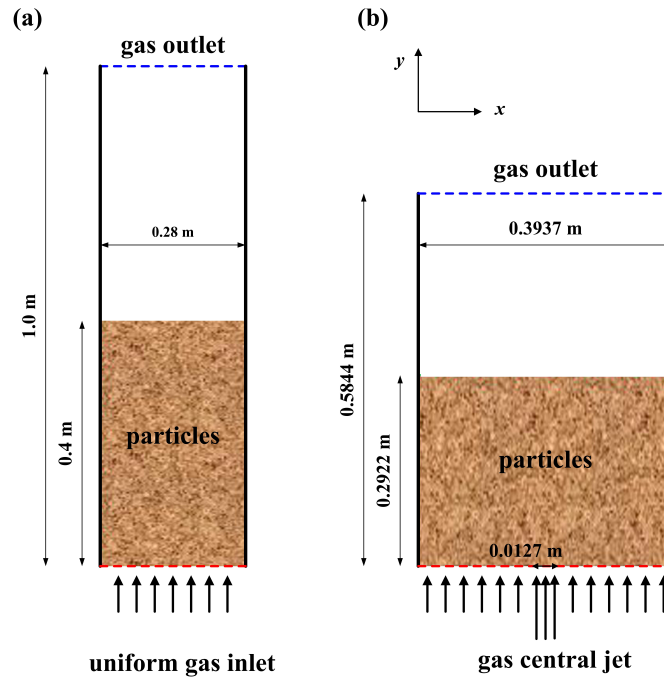
Figure 3.4: Schematics of fluidized beds with (a) uniform gas feed (b) a central jet

3.5.2 Simulation setup

The 2D computational domain is employed for the fluidized bed with uniform gas feed and is discretized with 11200 rectangular cells, corresponding to a grid width of 0.005 m. The grid size is the same as that adopted by Taghipour et al. [49]. The fluidized bed with a central jet is simulated using 2D domain with 124 cells in the x-direction and 108 cells in the y-direction. The parameters for the two fluidized bed cases are summed up in Tables 3.3 and 3.4. The transient simulations are conducted with an adaptive time step method. The time step is adapted with the Courant number which is defined in Eq.(3.45):

$$\text{Co} = \frac{\Delta t \mid \mathbf{U}_r \mid}{\Delta x} \tag{3.45}$$

where Δt is the time step, $|\mathbf{U}_r|$ is the magnitude of the relative velocity through the cell and Δx is the cell size in the direction of the relative velocity. The Courant number is not allowed to be larger than 0.1. The maximum value of time step is set to 1.0×10^{-4} s.

Table 3.3: Parameters for the simulation of fluidized bed with uniform gas feed

Parameter	Value
Bed width, m	0.28
Bed height, m	1.0
Bed depth, m	0.025
Initial bed height, m	0.4
Initial solid packing	0.6
Superficial gas velocity, m/s	0.38, 0.46
Min. fluidization velocity, m/s	0.065
Gas density, kg/m^3	1.2
Gas kinematic viscosity, m^2/s	1.4×10^{-5}
Particle diameter, m	2.8×10^{-4}
Particle density, kg/m^3	2500
Particle - particle restitution coefficient	0.8
Specularity coefficient	0.5
$\alpha_{s,\max}$	0.65
$\alpha_{s,\min}$	0.50

Table 3.4: Parameters for the simulation of fluidized bed with a central jet

Parameter	Value
Bed width, m	0.3937
Bed height, m	0.5844
Bed depth, m	0.0381
Jet orifice width, m	0.0127
Initial bed height, m	0.2922
Voidage at min. fluidization	0.402
Jet inlet velocity, m/s	1.511, 3.55
Min. fluidization velocity, m/s	0.282
Gas density, kg/m^3	1.2
Gas kinematic viscosity, m^2/s	1.4×10^{-5}
Particle diameter, m	5.0×10^{-4}
Particle density, kg/m^3	2610
Particle - particle restitution coefficient	0.8
Specularity coefficient	0.5
$\alpha_{s,\mathrm{max}}$	0.65
$\alpha_{s,\mathrm{min}}$	0.63

The inlets of fluidized beds are made impenetrable for the solid phase by setting the velocity of solid phase to be zero m/s. The uniform gas velocity is employed at the inlets. The pressure at the outlet is specified as the atmospheric pressure. The no-slip boundary condition is applied at the wall for the gas phase velocity, while the partial slip boundary condition proposed by Johnson and Jackson [6] is used for the solid phase in the two test cases. At the wall surfaces, the particle velocity is determined with the following correlation:

$$\nabla \tau_{s,\mathrm{w}} = -\frac{\pi}{6} \frac{\alpha_s}{\alpha_{s,\mathrm{max}}} \psi \rho_s g_0 \sqrt{3\Theta} \mathbf{U}_{s,\mathrm{w}} \tag{3.46}$$

where ψ is the specularity coefficient. When the value of ψ is zero, the perfect smooth wall exists, on the contrary unity represents the no-slip wall boundary condition.

3.6 Results and discussion

3.6.1 Model validations

3.6.1.1 Bubbling fluidized bed with uniform gas feed

Figure 3.5 shows the comparison of the simulated profiles of solid volume fraction with the experimental results measured at two gas inlet velocities (0.38 and 0.46 m/s). The simulations are run for 60 s of real time. The time-averaged results are computed over the last 55 s of

the simulation. It is tested that the time period for averaging is enough to obtain the time-averaged results. Here, the limitedLinear, limitedLinearV and limitedLinear01 schemes are adopted for the convection terms in the granular temperature transport equation, the phase momentum equations and the solid phase continuity equation, respectively. The simulated results of solid volume fraction give reasonable agreement with the experimental data. At the gas inlet velocity of 0.38 m/s, the dense particle flows are formed in the bed center region. While increasing gas inlet velocity to 0.46 m/s, the gas-particle flows are more developed which results in the flat radial profiles at the bed center.
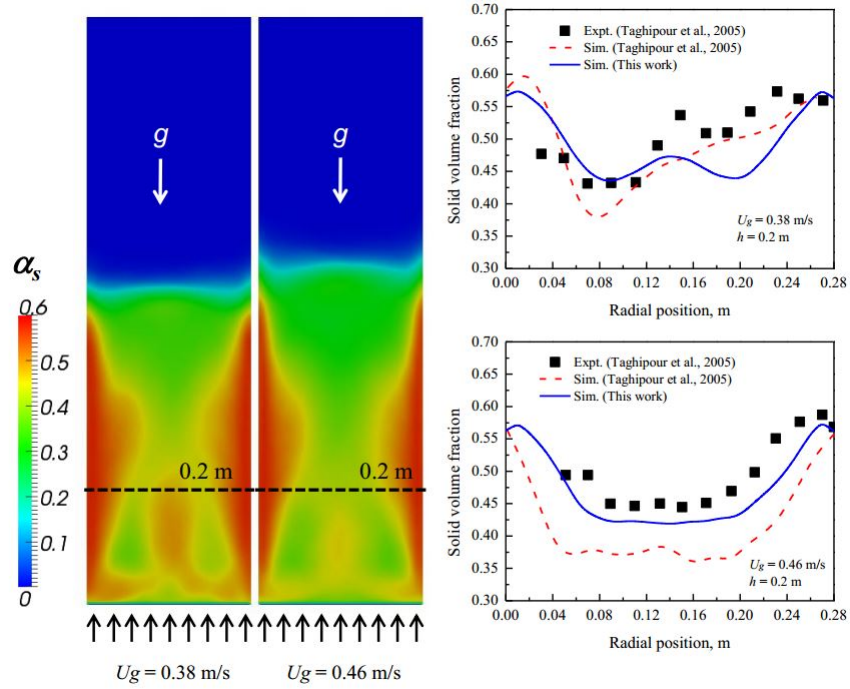
Figure 3.5: Comparison of the simulated time-averaged solid volume fractions with experimental data at two superficial gas velocities
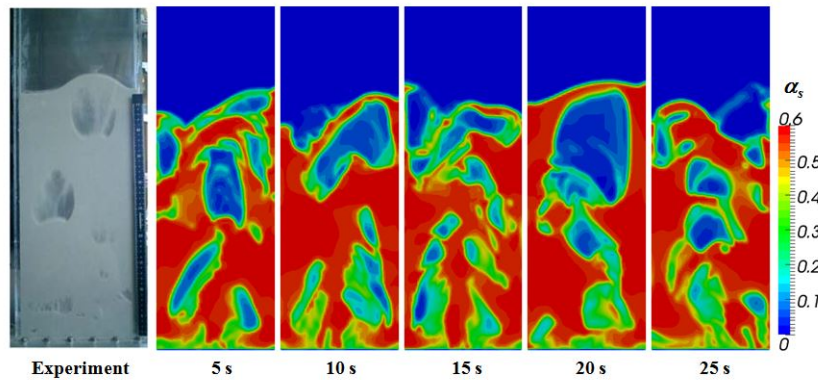
Figure 3.6: Snapshots of experimental and simulated solid volume fraction distributions ($U_g = 0.46$ m/s)

As a comparison, the simulated results collected from Taghipour et al. [49] are given in Figure 3.5. For the inlet velocity of 0.46 m/s, the simulated solid concentrations in this work show better predictions than those from Taghipour et al. [49]. Moreover, the typical core-annular flow structures in the fluidized bed are properly captured where high particle concentrations are found in the near wall region and low concentrations in the bed center. In Figure 3.6, the detailed bed hydrodynamics is shown by the contours of solid volume fraction and the snapshot from Taghipour et al. [49]. Both experimental and simulated results indicate that the small gas bubbles are mainly formed at the bed bottom, whereas the large bubbles exist at the upper part due to the bubble coalescence.

3.6.1.2   Bubbling fluidized bed with a central jet

The fluidized bed with a central gas jet is chosen to investigate the simulated bubble behaviors. Figure 3.7 displays the evolution of the first bubble injected by the central jet. Gradually, the first bubble is formed due to the more compact particle layer around it. The first bubble expands as it rises through the bed. The bubble shapes are quite similar to the ones simulated by Passalacqua and Marmo [51]. The typical rounded kidney shape of the first bubble is well captured at $t = 0.4$ s.
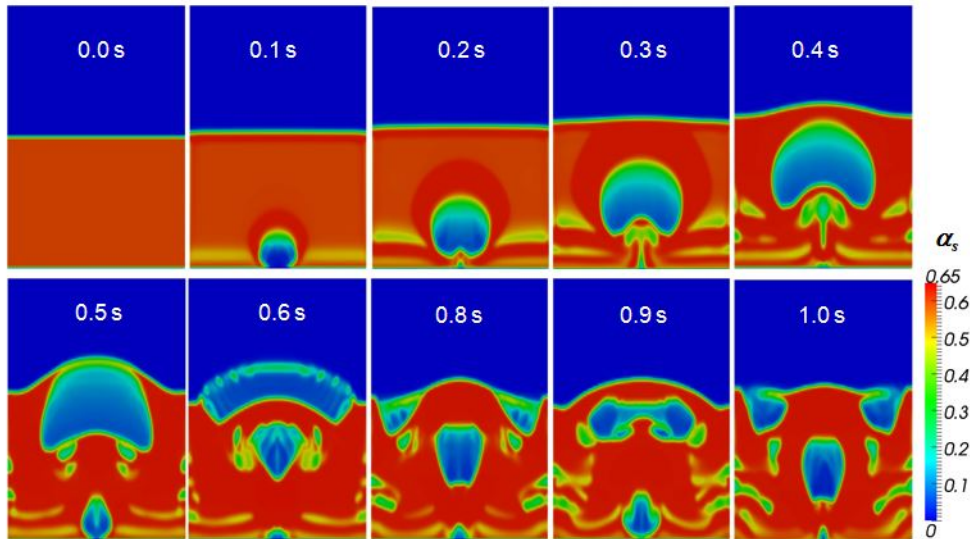
Figure 3.7: Simulated contours of the fluidized bed with a jet velocity of 3.55 m/s

Figure 3.8 gives the comparison of the simulated profiles of solid volume fraction with the experimental data from Gidaspow et al. [50]. The fine agreement between experiments and simulations is also achieved for two different jet velocities. In summary, our gas-solid solver is well capable of describing the solid particle concentrations and bubble behaviors in the different fluidized beds.
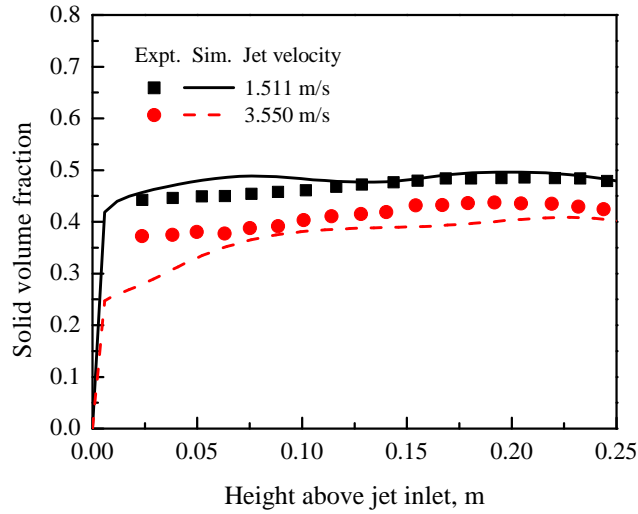
Figure 3.8: Comparison of the simulated profiles of solid volume fraction with the experimental data from Gidaspow et al. [50]

3.6.2 Discretization of phase velocity convection terms

For the velocity fields ($\mathbf{U}_s$ and $\mathbf{U}_g$), the V-schemes of the five TVD flux limiters are employed for all phase velocity convection terms. The gradient terms are discretized with the non-limited Gauss linear scheme. For the fluidized bed with uniform gas feed, the simulated radial profiles of particle axial velocity are compared for the five schemes (Figure 3.9). It is observed that the particles flow up in the bed center, while the downward flow exists in the near wall region. These particle flow patterns can be captured with the five schemes. Furthermore, the difference in the profiles of particle axial velocity is not pronounced among these schemes.
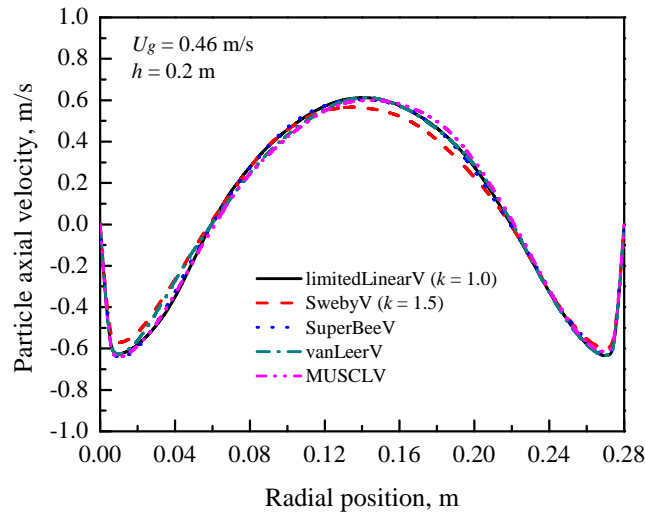
Figure 3.9: Effect of discretization of the phase velocity convection terms on the time-averaged results of particle axial velocity

The effect of the discretization of phase velocity convection terms on the first bubble shape is studied in the fluidized bed with a central jet. Figure 3.10 presents the comparison of the first bubbles simulated using the different schemes ($t = 0.4$ s). Clearly, the bubble shapes predicted with the five schemes are almost identical. Figure 3.11 indicates the simulated instantaneous profiles of particle axial velocity at the vertical position of 0.2 m in the bed. Also, quite similar velocity profiles are observed among the five schemes.

Since the five TVD schemes give quite similar results, it is inferred that the gradient ratio r calculated with Eq.(3.44) is around 1 and the five TVD flux limiters become the central differencing scheme (see Figure 3.3). From the above study, little care can be taken on the choice of the TVD convection schemes used for phase velocity convection terms.
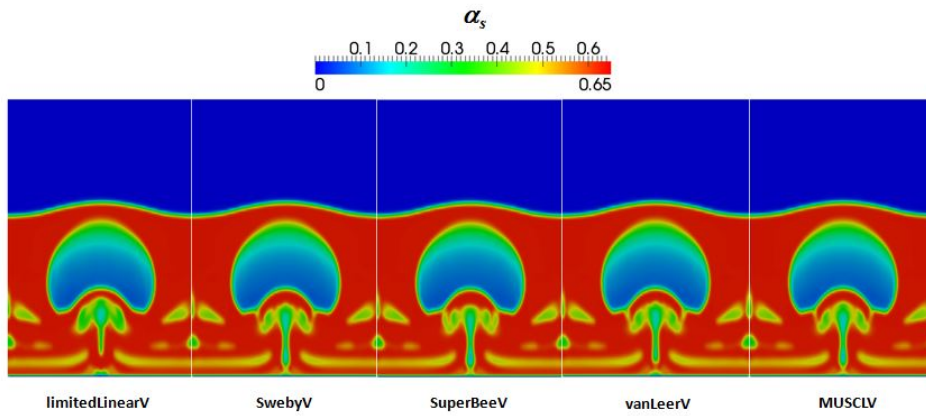
Figure 3.10: The bubble shapes simulated with five TVD schemes for the phase velocity convection terms ($t = 0.4$ s)
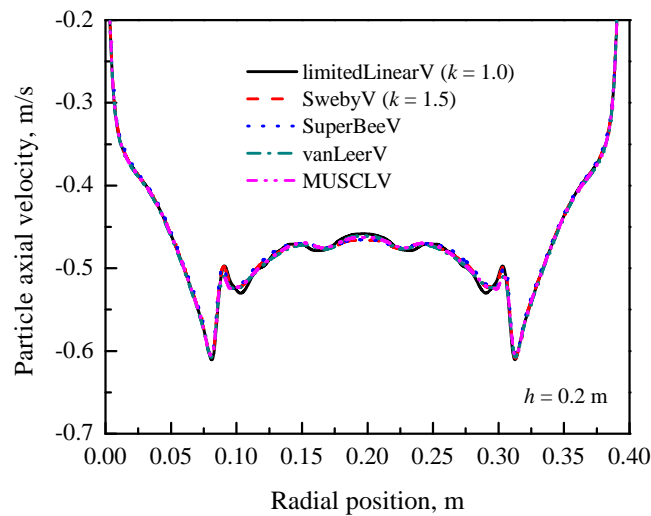
Figure 3.11: Effect of discretization of the phase velocity convection terms on the instantaneous particle axial velocities ($t = 0.4$ s).

3.6.3 Discretization of solid volume fraction convection terms

3.6.3.1 Comparison of the TVD schemes

The 01-schemes of the TVD flux limiters, i.e., limitedLinear01, Sweby01 and vanLeer01, are applied for the solid volume fraction convection terms. The phase velocity convection terms are discretized with the limitedLinearV scheme. The limitedLinear scheme is used for the granular temperature convection term. The gradient terms are discretized with the non-limited Gauss linear scheme. Figure 3.12 shows the comparison of the time-averaged profiles of particle axial velocity simulated with the limitedLinear01, Sweby01 and vanLeer01 schemes. The three schemes have no significant differences in the simulated profiles. Figure 3.13 presents the instantaneous contours of the first bubble predicted with the limitedLinear01, Sweby01 and vanLeer01 schemes at $t = 0.3$ s. Also, the bubble shapes predicted with the three schemes are quite similar to each other. However, the wakes following the first bubbles are different. Due to the gas jet with the high velocity, the strong convection takes place in the wakes. In such strong convective flows, the differences among the different schemes would be more obvious.
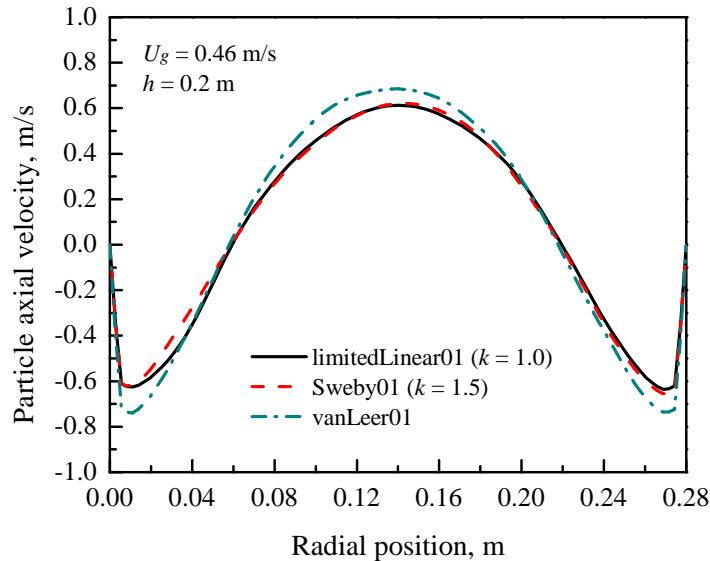
Figure 3.12: Effect of discretization of the solid volume fraction convection terms on the time-averaged results of particle axial velocity

It is found that the SuperBee01 and MUSCL01 schemes for solid volume fraction convection terms destroy the solution convergence. By using the SuperBee01 and MUSCL01 schemes, solid volume fraction cannot be effectively limited to be lower than the packing limit. When solid volume fraction reaches the packing limit, the radial distribution function g_0 becomes infinite which results in the solution divergence.
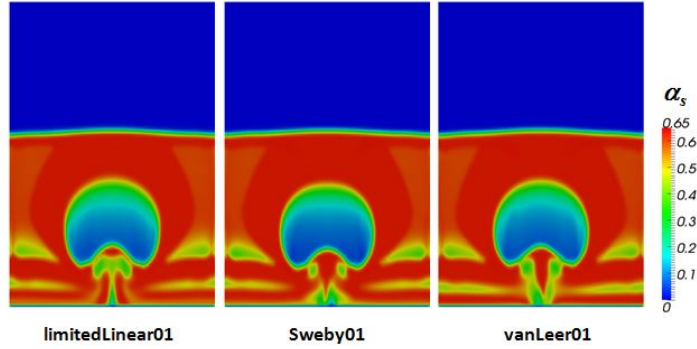
Figure 3.13: The bubble shapes simulated with different schemes for the solid volume fraction convection terms ($t = 0.3$ s)
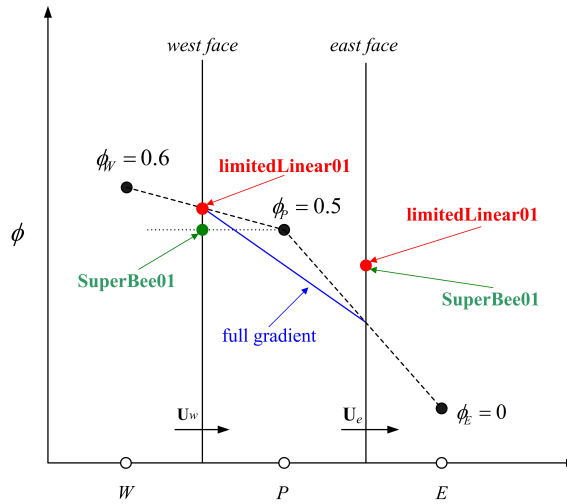
Figure 3.14: An example for comparing the limitedLinear01 and SuperBee01 schemes

In Figure 3.14 the face values of SuperBee01 scheme are compared with those of limitedLinear01 scheme. The one-dimensional variation of ϕ is used as an illustrative example. Here, the variable ϕ represents the solid volume fraction. The cell centers are uniformly located in the grid. In this case, the gradient ratio r has a value of 5 at the west face. Therefore, at the west face, the SuperBee01 scheme becomes the downwind scheme, while the limitedLinear01 scheme uses the central differencing. At the east face, the gradient ratio r is 0.2 and the same face value is interpolated with the SuperBee01 and limitedLinear01 schemes:

$$\phi_e = 0.8\phi_P + 0.2\phi_E \tag{3.47}$$

The first-order Euler implicit scheme is employed to discretize the transient term of solid volume fraction:

$$\int_V \frac{\partial \phi}{\partial t} dV = \frac{\partial}{\partial t} \int_V \phi dV = V_P \frac{\phi_P - \phi_P^{\text{o}}}{\Delta t} \tag{3.48}$$

where V_P is the volume of cell P, ϕ_P^{o} is the value at the previous time step, and Δt is the time step. By discretizing the transient, convection and diffusion terms in Eq.(3.47), the discretized solid phase continuity equation is given in the following form:

$$a_P \phi_P = a_W \phi_W + a_E \phi_E + S_P \tag{3.49}$$

The matrix coefficients in Eq.(3.49) for the limitedLinear01 scheme are listed as

$$a_P = \frac{V_P}{\Delta t} + 0.5 F_w + 0.8 F_e + \frac{\Gamma_w \mid \mathbf{S}_w \mid}{\mid \mathbf{d} \mid} + \frac{\Gamma_e \mid \mathbf{S}_e \mid}{\mid \mathbf{d} \mid} \tag{3.50}$$

$$a_W = \frac{\Gamma_w \mid \mathbf{S}_w \mid}{\mid \mathbf{d} \mid} - 0.5 F_w \tag{3.51}$$

$$a_E = \frac{\Gamma_e \mid \mathbf{S}_e \mid}{\mid \mathbf{d} \mid} - 0.2 F_e \tag{3.52}$$

$$S_P = \frac{V_P}{\Delta t} \phi_P^{\text{o}} \tag{3.53}$$

where F_e and F_w are the flux at the east and west face, respectively, $F_e > 0$ and $F_w < 0$. Γ is the coefficient in the diffusion term. By using the SuperBee01 scheme, the matrix coefficients in Eq.(3.49) are given as

$$a_P = \frac{V_P}{\Delta t} + F_w + 0.8 F_e + \frac{\Gamma_w \mid \mathbf{S}_w \mid}{\mid \mathbf{d} \mid} + \frac{\Gamma_e \mid \mathbf{S}_e \mid}{\mid \mathbf{d} \mid} \tag{3.54}$$

$$a_W = \frac{\Gamma_w \mid \mathbf{S}_w \mid}{\mid \mathbf{d} \mid} \tag{3.55}$$

$$a_E = \frac{\Gamma_e \mid \mathbf{S}_e \mid}{\mid \mathbf{d} \mid} - 0.2 F_e \tag{3.56}$$

$$S_P = \frac{V_P}{\Delta t} \phi_P^{\text{o}} \tag{3.57}$$

Comparing Eq.(3.50) with Eq.(3.54), the matrix coefficient of ϕ_P obtained using the Super-Bee01 scheme is more prone to the negative value, especially when using large time step. According to Versteeg and Malalasekera [52], the negative matrix coefficients would violate the solution boundedness and destroy numerical stability. From Eq.(3.37), the face flux F_e and F_w include the contribution from the solid pressure gradient, which could make the face flux much larger and diverge the solutions more readily. The same stability problem is also encountered by the MUSCL01 scheme.

To further verify the above analysis, the SuperBee01 and MUSCL01 schemes are modified to approach to central differencing by reducing the downwind. The stable solutions are obtained with the modified schemes. Figure 3.15 shows the contours of the first bubble in the bed with a central jet.
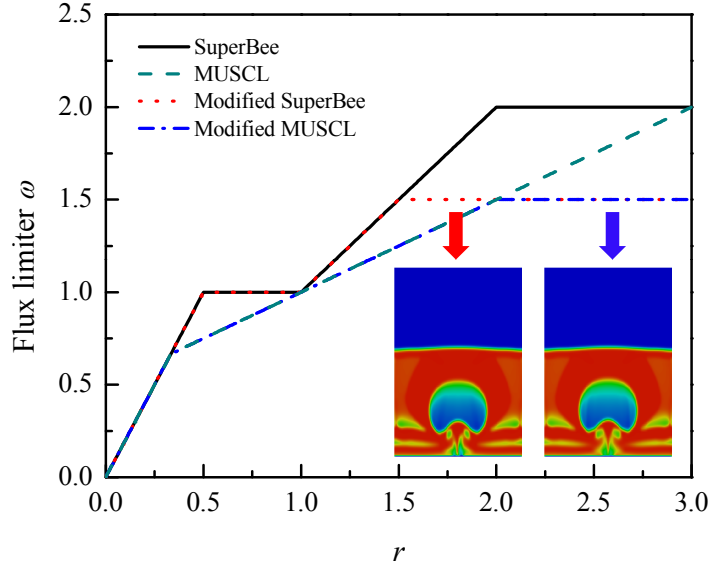
Figure 3.15: Simulated results with the modified SuperBee01 and MUSCL01 schemes

3.6.3.2 The influence of gradient discretization scheme

From Eqs.(3.43) and (3.44), the gradient discretization scheme plays an important role in the calculation of the gradient ratio r used in TVD convection schemes. By combining with the limitedLinear01 convection scheme, the non-limited, cellLimited, faceLimited and cellMDLimited versions of Gauss linear scheme are investigated for the gradient term of solid volume fraction. The gradient limiting method makes the pure Gauss linear scheme more stable [21]. The different gradient limiting methods are illustrated in Appendix B.

Figure 3.16 displays the simulated bubbles with different gradient limiting methods. The non-limited, cellLimited and cellMDLimited methods produce the rounded kidney bubbles, whereas the unphysical pointed shape [24] is predicted by the faceLimited method. The pointed bubble is also predicted with upwind scheme. A large amount of numerical diffusion is introduced by the upwind scheme. It is inferred the faceLimited method generates small values of the gradient ratio r, and makes the limitedLinear01 scheme more diffusive (see Figure 3.3). Hence, the faceLimited scheme should not be applied for the gradient terms, although it provides good numerical stability. The cellLimited and cellMDLimited gradient schemes are recommended to achieve the simulations with higher accuracy and better stability.
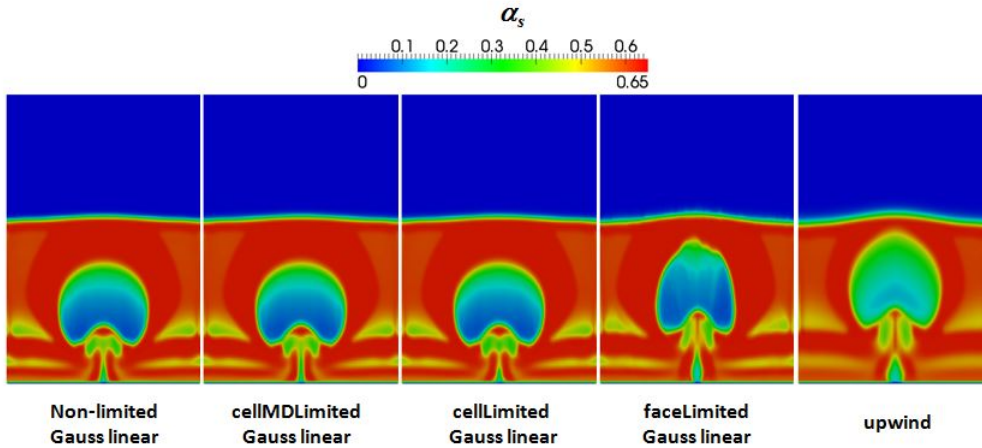
Figure 3.16: The bubble shapes simulated with different schemes for the gradient term of solid volume fraction

3.7   Conclusions

The gas-solid OpenFOAM solver based on two-fluid model is validated by simulating two different fluidized beds. The simulated results of solid volume fraction are in good agreement with the experimental data from the literature. The first bubble in the bed with a central jet is well predicted. The gas-solid solver is capable of predicting the gas-solid flows in the two fluidized beds.

For the discretization of the phase velocity convection terms, the five TVD schemes give very similar time-averaged results of particle axial velocity in the bed with uniform gas feed. In the bed with a central jet, the predicted first bubble shapes and particle velocity profiles are also quite similar among the five schemes. The five schemes have no stability problem in the discretization of phase velocity convection terms. Therefore, the choice of the TVD schemes needs little attention when discretizing the phase velocity convection terms.

When discretizing the solid volume fraction convection terms, the limitedLinear01, Sweby01 and vanLeer01 schemes give the stable solutions in the two test cases. The three schemes have no significant differences in the simulated results. However, in the discretized solid phase continuity equation, the SuperBee01 and MUSCL01 schemes generate the negative matrix coefficients and destroy the solution convergence. The faceLimited gradient scheme makes the convection scheme more diffusive. The cellLimited and cellMDLimited schemes have high accuracy and good stability.

Appendix A. Discretization of Laplacian term

The Laplacian term is integrated over a control volume and discretized as follows:

$$\int_V \nabla \cdot (\Gamma \nabla \phi) dV = \int_S d\mathbf{S} \cdot (\Gamma \nabla \phi) \approx \sum_f \Gamma_f \mathbf{S}_f \cdot (\nabla \phi)_f \qquad (3.58)$$

The face gradient is implicitly discretized when the vector $\mathbf{d}$ between the own cell center and the neighboring cell center is orthogonal to the face:

$$\mathbf{S}_f \cdot (\nabla \phi)_f = \mid \mathbf{S}_f \mid \frac{\phi_N - \phi_P}{\mid \mathbf{d} \mid} \qquad (3.59)$$

Appendix B. Gradient schemes

The gradient term is usually integrated over a control volume and discretized as

$$\int_V \nabla \phi dV = \int_S d\mathbf{S} \phi = \sum_f \mathbf{S}_f \phi_f \qquad (3.60)$$

For incompressible flows the face value ϕ_f is usually calculated using the linear interpolation (i.e., Gauss linear scheme in OpenFOAM). The cell-centered gradient (full gradient) at the cell P is calculated as

$$(\nabla \phi)_P = \frac{1}{V_P} \sum_f \mathbf{S}_f \phi_f \qquad (3.61)$$

where V_P is the volume of the cell P. Gradient reconstruction may lead to the unbounded face value (Figure 3.17). The gradient limiting is necessary for the bounded variable. There are two types of gradient limiting available in OpenFOAM, i.e., cell limiting and face limiting. For the cell limited gradient, the neighbor cell with the maximum value of ϕ and the neighbor cell with the minimum value of ϕ are firstly found. Then, the cell limited gradient is calculated as

$$(\nabla \phi)_{P,cellLimited} = \begin{cases} \dfrac{H}{D}(\nabla \phi)_P & D > H \\[2mm] \dfrac{h}{d}(\nabla \phi)_P & h < d \end{cases} \qquad (3.62)$$

The parameters h and H are calculated as follows:

$$h = \phi_{min} - \phi_P, \quad H = \phi_{max} - \phi_P$$

The parameters d and D are calculated based on the full gradient:

$$d = \mathbf{d}_f \cdot (\nabla \phi)_P, \quad D = \mathbf{d}_f \cdot (\nabla \phi)_P$$

where $\mathbf{d}_f$ is the vector connecting the owner cell center and one of its bounding face centers.
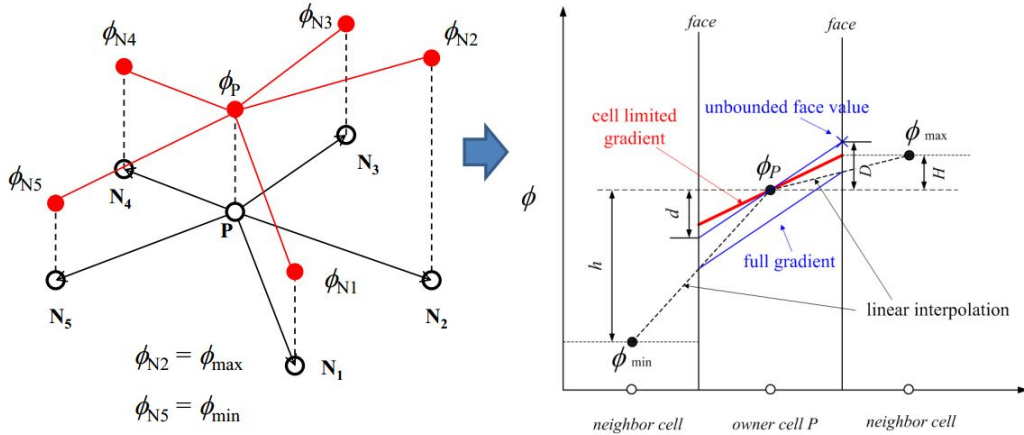
Figure 3.17: The cell limited gradient scheme in OpenFOAM
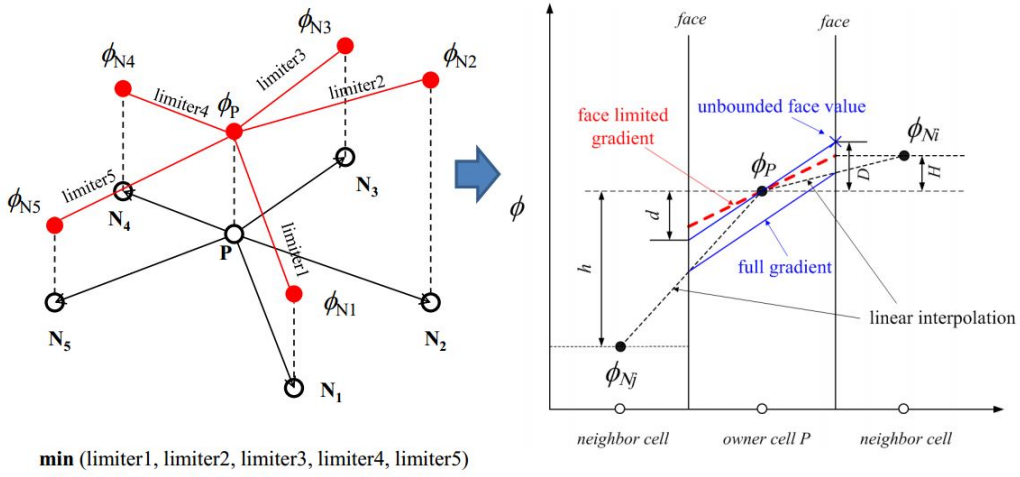
Figure 3.18: The face limited gradient scheme in OpenFOAM

The multi-dimensional version of the cell limited gradient scheme (i.e., cellMDLimited scheme in OpenFOAM) applies the gradient limiter for each face and is expressed as

$$(\nabla\phi)_{P,cellMDLimited} = \begin{cases} (\nabla\phi)_P + \dfrac{\mathbf{d}_f(H-D)}{[\mathbf{d}_f \cdot (\nabla\phi)_P]^2} & D > H \\[3mm] (\nabla\phi)_P + \dfrac{\mathbf{d}_f(h-d)}{[\mathbf{d}_f \cdot (\nabla\phi)_P]^2} & h < d \end{cases} \tag{3.63}$$

Instead of using the cell neighbors having the maximum and minimum values of ϕ, the face limited gradient is calculated by multiplying the minimum face limiter with the full gradient. For each face bounding the owner cell, each face limiter is calculated (Figure 3.18). By comparing each face limiter, the minimum face limiter is chosen to calculate the face limited gradient.

Literature

[1] M. Ishii, T. Hibiki, Thermo-fluid dynamics of two-phase flow, Springer, New York, 2006.

[2] J. M. Ding, R. W. Lyczkowski, A bubbling fluidization model using kinetic theory of granular flow, AIChE Journal 73 (1990) 523–538.

[3] H. Enwald, E. Peirano, A. E. Almstedt, Eulerian two-phase flow theory applied to fluidization, International Journal of Multiphase Flow 22 (1996) 21–66.

[4] J. T. Jenkins, S. B. Savage, A theory of the rapid flow of identical, smooth, nearly elastic spherical particles, Journal of Fluid Mechanics 130 (1983) 187–202.

[5] C. K. K. Lun, S. B. Savage, D. J. Jeffrey, N. Chepurniy, Kinetic theories for granular flow: inelastic particles in Couette flow and slightly inelastic particles in a general flowfield, Journal of Fluid Mechanics 140 (1984) 223–256.

[6] P. C. Johnson, R. Jackson, Frictional-collisional constitutive relations for granular materials, with application to plane shearing, Journal of Fluid Mechanics 176 (1987) 67–93.

[7] D. G. Schaeffer, Instability in the evolution equations describing incompressible granular flow, Journal of Differential Equations 66 (1987) 19–50.

[8] A. Srivastava, S. Sundaresan, Analysis of a frictional-kinetic model for gas-particle flow, Powder Technology 129 (2003) 72–85.

[9] P. Lettieri, L. Cammarata, G. D. M. Micale, J. Yates, CFD simulations of gas fluidized beds using alternative Eulerian-Eulerian modeling approaches, International Journal of Chemical Reactor Engineering 1 (2003) 1–21.

[10] N. Yang, W. Wang, W. Ge, J. H. Li, CFD simulation of concurrent-up gas-solid flow in circulating fluidized beds with structure-dependent drag coefficient, Chemical Engineering Journal 96 (2003) 71–80.

[11] I. Hulme, E. Clavelle, L. van der Lee, A. Kantzas, CFD modeling and validation of bubble properties for a bubbling fluidized bed, Industrial & Engineering Chemistry Research 44 (2005) 4254–4266.

[12] B. Chalermsinsuwan, P. Kuchonthara, P. Piumsomboon, CFD modeling of tapered circulating fluidized bed reactor risers: Hydrodynamic descriptions and chemical reaction responses, Chemical Engineering and Processing 49 (2010) 1144–1160.

[13] T. W. Asegehegn, M. Schreiber, H. J. Krautz, Numerical simulation and experimental validation of bubble behavior in 2D gas-solid fluidized beds with immersed horizontal tubes, Chemical Engineering Science 66 (2011) 5410–5427.

[14] K. Zhang, P. Pei, S. Brandan, H. G. Chen, Y. P. Yang, CFD simulation of flow pattern and jet penetration depth in gas-fluidized beds with single and double jets, Chemical Engineering Science 68 (2012) 108–119.

[15] M. Syamlal, W. Rogers, T. J. O'Brien, MFIX documentation: Theory Guide, Technical Note, DOE/METC-94/100, Morgantown Energy Technology Center Morgantown, WV, USA (1993).

[16] T. McKeen, T. Pugsley, Simulation and experimental validation of a freely bubbling bed of FCC catalyst, Powder Technology 129 (2003) 139–152.

[17] T. W. Li, J. Grace, X. T. Bi, Study of wall boundary condition in numerical simulations of bubbling fluidized beds, Powder Technology 203 (2010) 447–457.

[18] T. W. Li, J.-F. Dietiker, Y. M. Zhang, M. Shahnam, Cartesian grid simulations of bubbling fluidized beds with a horizontal tube bundle, Chemical Engineering Science 66 (2011) 6220–6231.

[19] H. L. Lu, D. Gidaspow, Hydrodynamics of binary fluidization in a riser: CFD simulation using two granular temperatures, Chemical Engineering Science 58 (2003) 3777–3792.

[20] H. L. Lu, Y. R. He, W. T. Liu, J. M. Ding, D. Gidaspow, J. Bouillard, Computer simulations of gas-solid flow in spouted beds using kinetic-frictional stress model of granular flow, Chemical Engineering Science 59 (2004) 865–878.

[21] OpenCFD Ltd., OpenFOAM 2.1.1 User's Guide, UK (2012).

[22] N. Herzog, M. Schreiber, C. Egbers, H. J. Krautz, A comparative study of different CFD-codes for numerical simulation of gas-solid fluidized bed hydrodynamics, Computers and Chemical Engineering 39 (2012) 41–46.

[23] A. Passalacqua, R. O. Fox, Implementation of an iterative solution procedure for multi-fluid gas-particle flow models on unstructured grids, Powder Technology 213 (2011) 174–187.

[24] C. Guenther, M. Syamlal, The effect of numerical diffusion on simulation of isolated bubbles in a gas-solid fluidized bed, Powder Technology 116 (2001) 142–154.

[25] M. P. S. Braun, A. T. Mineto, H. A. Navarro, L. Cabezas-Gomez, R. C. Silva, The effect of numerical diffusion and the influence of computational grid over gas-solid two-phase flow in a bubbling fluidized bed, Mathematical and Computer Modeling 52 (2010) 1390–1402.

[26] D. Gidaspow, Multiphase Flow and Fluidization, 1st Edition, Academic Press, New York, 1994.

[27] S. Ergun, Fluid flow through packed columns, Chemical Engineering Progress 48 (1952) 89–95.

[28] C. Y. Wen, Y. H. Yu, Mechanics of fluidization, Chemical Engineering Progress Symposium Series 62 (1996) 100–111.

[29] J. L. Sinclair, R. Jackson, Gas-particle flow in a vertical pipe with particle-particle interactions, AIChE Journal 35 (1989) 1473–1486.

[30] P. C. Johnson, P. Nott, R. Jackson, Frictional-collisional equations of motion for particulate flows and their application to chutes, Journal of Fluid Mechanics 210 (1990) 501–535.

[31] P. J. Oliveira, R. I. Issa, Numerical aspects of an algorithm for the Eulerian simulation of two-phase flows, International Journal for Numerical Methods in Fluids 43 (2003) 1177–1198.

[32] I. K. Park, H. K. Cho, H. Y. Yoon, J. J. Jeong, Numerical effects of the semi-conservative form of momentum equations for multi-dimensional two-phase flows, Nuclear Engineering and Design 239 (2009) 2365–2371.

[33] D. B. Spalding, Numerical computation of multi-phase fluid flow and heat transfer. In: C. Taylor Ed., Recent Advances in Numerical Methods in Fluids, Pineridge Press, 1980.

[34] R. Issa, Solution of the implicitly discretized fluid flow equations by operator-splitting, Journal of Computational Physics 62 (1985) 40–65.

[35] H. Rusche, Computational fluid dynamics of dispersed two-phase flows at high phase fractions, Ph.D. thesis, Imperial College of Science, Technology and Medicine, London, UK (2002).

[36] M. Syamlal, MFIX documentation: Numerical Technique. EG&G Technical Services of West Virginia, Inc., Morgantown, WV, USA (1998).

[37] J. Bouillard, R. Lyczkowski, D. Gidaspow, Porosity distributions in a fluidized bed with immersed obstacle, AIChE Journal 35 (1989) 908–922.

[38] N. P. Waterson, H. Deconinck, Design principles for bounded higher-order convection schemes - a unified approach, Journal of Computational Physics 224 (2007) 182–207.

[39] H. Jasak, Error analysis and estimation for the finite volume method with applications to fluid flows, Ph.D. thesis, Imperial College of Science, Technology and Medicine, London, UK (1996).

[40] P. K. Khosla, S. G. Rubin, A diagonally dominant second-order accurate implicit scheme, Computers and Fluids 2 (1974) 207–209.

[41] A. Harten, High resolution schemes for hyperbolic conservation laws, Journal of Computational Physics 49 (1983) 357–393.

[42] P. K. Sweby, High resolution schemes using flux limiters for hyperbolic conservation laws, SIAM Journal on Numerical Analysis 21 (1984) 995–1011.

[43] B. P. Leonard, Simple high-accuracy resolution program for convective modelling of discontinuities, International Journal for Numerical Methods in Fluids 8 (1988) 1291–1318.

[44] P. H. Gaskell, A. K. C. Lau, Curvature-compensated convective transport: SMART, a new boundedness-preserving transport algorithm, International Journal for Numerical Methods in Fluids 8 (1988) 617–641.

[45] C. J. Greenshields, H. G. Weller, L. Gasparini, J. M. Reese, Implementation of semi-discrete, non-staggered central schemes in a colocated, polyhedral, finite volume framework, for high-speed viscous flows, International Journal for Numerical Methods in Fluids 63 (2009) 1–21.

[46] P. L. Roe, Some contributions to the modeling of discontinuities flow, Lectures in Applied Mathematics 22 (1985) 163–192.

[47] B. van Leer, Towards the ultimate conservative difference scheme. II. Monotonicity and conservation combined in a second order scheme, Journal of Computational Physics 14 (1974) 361–370.

[48] B. van Leer, Towards the ultimate conservative difference scheme. V. A second-order sequel to Godunov method, Journal of Computational Physics 32 (1979) 101–136.

[49] F. Taghipour, N. Ellis, C. Wong, Experimental and computational study of gas-solid fluidized bed hydrodynamics, Chemical Engineering Science 60 (2005) 6857–6867.

[50] D. Gidaspow, C. Lin, Y. C. Seo, Fluidization in two-dimensional beds with a jet. 1. Experimental porosity distributions, Industrial and Engineering Chemistry Fundamentals 22 (1983) 187–193.

[51] A. Passalacqua, L. Marmo, A critical comparison of frictional stress models applied to the simulation of bubbling fluidized beds, Chemical Engineering Science 160 (2009) 2795 –2806.

[52] H. K. Versteeg, W. Malalasekera, An Introduction to Computational Fluid Dynamics, 2nd Edition, Pearson Education Limited, England, 2007.

Chapter 4

Numerical simulation of the tube erosion in a bubbling fluidized bed with a dense tube bundle

This chapter originates from the following publication:

Abstract

Tube erosion in a bubbling fluidized bed is numerically studied using the Eulerian-Eulerian method coupled with a monolayer kinetic energy dissipation model. The hydrodynamical simulations are performed under conditions with three different superficial gas velocities. The time-averaged bubble frequency and bubble rise velocity are calculated to characterize the bed hydrodynamics. The erosion rates of two target tubes are simulated and the influence of the bubble behaviors on erosion rates is evaluated. Compared with the experimental data in the literature, the bubble behaviors are well captured by the simulations. Good agreement between the calculated and measured erosion rates is also obtained for the two target tubes. The bubble behaviors around the tubes have direct impact on the tube erosion. Only small discrepancies in the calculated erosion rates are found when using different particle-wall restitution coefficients and specularity coefficients.

4.1   Introduction

Gas-solid fluidized beds are widely used in various industrial processes such as combustion, gasification, granulation, and polymerization. For many applications tube bundles are usually inserted into the fluidized beds to modify the inner flow structures, with an effort to enhance transfer and conversion rates, to control operating temperatures, and to reduce gulf circulation of solid particles. For bubbling fluidized beds with tube bundles, the moving gas and solid particles always introduce the tube erosion problems, especially in fluidized bed combustors with tube heat exchangers. The erosion results in material degradation and loss, and eventually affects the continuous operation and the economics of fluidized bed plants [1, 2].

The issue of tube erosion in fluidized beds has received much attention, and remarkable progress has been made in the erosion modeling. Generally, the tube erosion modeling is numerically coupled with the simulations of the hydrodynamics in fluidized beds. There are two widely used computational fluid dynamics (CFD) methods to simulate the hydrodynamics in the gas-solid flows, i.e. the Eulerian-Lagrangian approach and the Eulerian-Eulerian approach. For the Eulerian-Lagrangian method, the physical information of the impacting particles, which is essential to some erosion models, is obtained using the Lagrangian method, and the continuous gas phase is described in the Eulerian manner [3, 4]. Although the Eulerian-Lagrangian method can provide the details of the particle-tube collisions, it is computationally expensive for engineering applications. Alternatively, the Eulerian-Eulerian approach describes the particulate phase as a continuum like a fluid phase by using the Navier-Stokes equations. It is more efficient for the simulations of large-scale processes. Based on the Eulerian-Eulerian method, the kinetic theory erosion model and kinetic energy dissipation erosion model were respectively developed to predict the tube erosions [5, 6]. Due to its low computational demand, the Eulerian-Eulerian method has been extensively applied for investigating erosion rates on the surfaces of the immersed tubes in fluidized beds [7–10].

However, previous numerical studies on tube erosion were only focused on single or very few tubes in gas-solid fluidized beds. Since the densely arranged tubes would complicate the hydrodynamics and then influence the erosion characteristics, the CFD method coupled with the erosion models should be further investigated for simulating dense tube configurations, which is more meaningful and practical for designing and optimizing realistic industrial devices. Simulations on the hydrodynamics in fluidized beds with dense tube bundles have been performed by several researchers. Asegehegn et al. [11] simulated a pseudo-2D fluidized bed with 36 tubes using the Eulerian-Eulerian two-fluid model. Li et al. [12] numerically investigated a bubbling fluidized bed containing 25 tubes by using a cell-cutting technique to deal with the curved tube surfaces in the Cartesian coordinate system. Yusuf et al. [13] studied the tube-to-bed heat transfer in a fluidized bed with 45 tubes based on the Eulerian-Eulerian approach. However, the above reported work only focused on the simulations of hydrodynamics and heat transfer in fluidized beds without considering the tube erosion process. Furthermore, most of the hydrodynamics modeling was just verified by qualitative

comparisons between simulations and experimental data. The influence of the wall boundary conditions on the simulations of erosion rates was also not reported in the previous work. Hence, a parametric study is necessary for better understanding of key modeling parameters as basis for more efficient simulations.

Almstedt et al. have carried out a lot of experimental investigations in tube erosion occurring in the fluidized beds with a large number of tubes [14–16]. They studied the influence of pressure, fluidization velocity, particle size and tube bank geometry on the tube erosion in the fluidized beds. Their experimental work can provide a validation basis on which further studies on the numerical models can be achieved in a more reliable manner.

The coupling of the hydrodynamics simulations with erosion modeling is taken into account to calculate the total erosion rates of the target tubes immersed in a fluidized bed. The Eulerian-Eulerian two fluid model is used to simulate the gas-solid flows. The monolayer kinetic energy dissipation model is used to calculate the erosion rates with the input of the hydrodynamic information. The influence of the wall boundary conditions on the simulated erosion rates is also investigated.
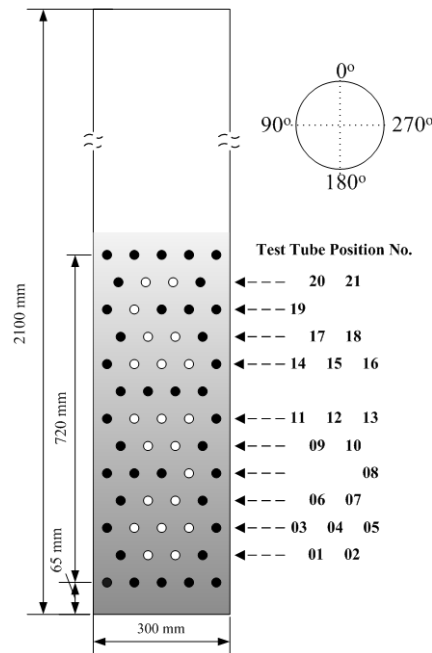
Figure 4.1: Schematic representation of the bubbling fluidized bed with 59 immersed tubes used in the experimental work of Johansson et al. [16].

4.2   Experimental

The experimental work by Johansson et al. [16] is used to validate the hydrodynamics and erosion simulations. The experimental setup (Figure 4.1) was a 2.1-m long fluidized bed with a rectangular cross-section of 0.2 m × 0.3 m. Inside the bed a tube bundle with 59 tubes was horizontally equipped, of which 21 tubes were exchangeable for erosion testing. Prior to the

exposure to gas-solid flows, each testing tube was smoothed to an outer diameter of 0.0264 m. The testing tubes were made of AISI 304L stainless steel.

The bed material was silica sand with a mean particle diameter d_{p} of 0.0007 m and a density ρ_s of 2600 kg/m^3. The bed height at minimum fluidization was 0.86 m with the corresponding voidage of 0.46 and the minimum fluidization velocity U_{mf} of 0.25 m/s. Hydrodynamics measurements were performed for three superficial gas velocities ($U_{\mathrm{fl}} = 0.4$, 0.65 and 1.0 m/s), while the local tube erosion rates were only measured on tubes exposed to the lowest and highest superficial gas velocities. The superficial gas velocity U_{fl} was determined based on the free bed cross-section. The exposure time for the two gas velocities was 1440 h and 504 h, respectively. The local bubble behaviors were measured using a capacitance probe located between the tubes No.12 and No.15. The mean bubble frequency N_{b} was determined from the signals of the lowest positioned capacitor. The erosion rates were determined by subtracting the measured radii along the circumference before and after exposure.

4.3 Mathematical models

4.3.1 Fluid dynamics models

The hydrodynamics of gas-solid flows is simulated using the Eulerian-Eulerian two fluid model with constitutive equations. The constitutive models were derived based on the Kinetic Theory of Granular Flow (KTGF). The continuity equations of gas and solid phases can be written as

$$\frac{\partial(\alpha_g \rho_g)}{\partial t} + \nabla \cdot (\alpha_g \rho_g \mathbf{U}_g) = 0 \tag{4.1}$$

$$\frac{\partial(\alpha_s \rho_s)}{\partial t} + \nabla \cdot (\alpha_s \rho_s \mathbf{U}_s) = 0 \tag{4.2}$$

The gas and solid volume fractions are related as

$$\alpha_g + \alpha_s = 1 \tag{4.3}$$

The momentum conservation equations of gas and solid phases are, respectively, described as follows:

$$\frac{\partial(\alpha_g \rho_g \mathbf{U}_g)}{\partial t} + \nabla \cdot (\alpha_g \rho_g \mathbf{U}_g \mathbf{U}_g) = -\alpha_g \nabla p + \nabla \cdot (\alpha_g \tau_g) + \beta(\mathbf{U}_s - \mathbf{U}_g) + \alpha_g \rho_g \mathbf{g} \tag{4.4}$$

$$\frac{\partial(\alpha_s \rho_s \mathbf{U}_s)}{\partial t} + \nabla \cdot (\alpha_s \rho_s \mathbf{U}_s \mathbf{U}_s) = -\alpha_s \nabla p - \nabla p_s + \nabla \cdot (\alpha_s \tau_s) + \beta(\mathbf{U}_g - \mathbf{U}_s) + \alpha_s \rho_s \mathbf{g} \tag{4.5}$$

To close the above momentum equations, the drag force model is needed and represented by the product of the interphase momentum transfer coefficient β and the slip velocity

$(\mathbf{U}_g - \mathbf{U}_s)$. β is calculated by Eq.(4.6) according to Gidaspow [17], who adopted the Wen and Yu correlation for $\alpha_s < 0.2$ and the Ergun equation for $\alpha_s \geqslant 0.2$.

This drag model was recommended for describing dense fluidized beds.

$$\beta = \begin{cases} \dfrac{3}{4}\dfrac{C_{\mathrm{d}}\alpha_g\alpha_s\rho_g|\mathbf{U}_g - \mathbf{U}_s|}{d_{\mathrm{p}}}\alpha_g^{-2.65}, & \alpha_s < 0.2 \\[3mm] 150\dfrac{\mu_g\alpha_s^2}{\alpha_g^2 d_{\mathrm{p}}^2} + 1.75\dfrac{\rho_g\alpha_s}{\alpha_g d_{\mathrm{p}}}|\mathbf{U}_g - \mathbf{U}_s|, & \alpha_s \geqslant 0.2 \end{cases} \tag{4.6}$$

The drag coefficient C_{d} in Eq.(4.6) is calculated by

$$C_{\mathrm{d}} = \begin{cases} \dfrac{24}{\mathrm{Re}_{\mathrm{p}}}[1 + 0.15(\mathrm{Re}_{\mathrm{p}})^{0.687}], & \mathrm{Re}_{\mathrm{p}} < 1000 \\[3mm] 0.44, & \mathrm{Re}_{\mathrm{p}} \geqslant 1000 \end{cases} \tag{4.7}$$

where the particle Reynolds number Re_{p} is defined as

$$\mathrm{Re}_{\mathrm{p}} = \frac{\rho_g d_{\mathrm{p}}|\mathbf{U}_g - \mathbf{U}_s|}{\mu_g} \tag{4.8}$$

The gases in the fluidized bed are assumed to be Newtonian fluids and the gas phase stress tensor τ_g in Eq.(4.4) can be modeled using the Newtonian stress-strain relation:

$$\tau_g = \mu_g[\nabla\mathbf{U}_g + (\nabla\mathbf{U}_g)^{\mathrm{T}}] - \frac{2}{3}\mu_g(\nabla \cdot \mathbf{U}_g)\mathbf{I} \tag{4.9}$$

where the dynamic viscosity μ_g is assumed to be constant and $\mathbf{I}$ is the unit tensor.

The properties of the solid phase, i.e., the solid shear stress τ_s and solid pressure p_s in Eq.(4.5), were derived based on the Kinetic Theory of Granular Flow [17]. For the Kinetic Theory of Granular Flow, the fluctuation energy of the granular phase, also known as granular temperature Θ, can be obtained by solving the granular temperature transport equation which is expressed as follows:

$$\frac{3}{2}\left[\frac{\partial(\alpha_s\rho_s\Theta)}{\partial t} + \nabla \cdot (\alpha_s\rho_s\mathbf{U}_s\Theta)\right] = (-p_s\mathbf{I} + \tau_s) : \nabla\mathbf{U}_s + \nabla \cdot (\kappa_s\nabla\Theta) - \gamma_s + J_{vis} + J_{slip} \tag{4.10}$$

where κ_s is the conductivity of granular temperature, γ_s the collision dissipation rate of granular temperature, J_{vis} the dissipation rate of granular temperature resulting from viscous damping, and J_{slip} the production rate of granular temperature due to the slip between gas and particle. The solid phase shear stress tensor τ_s can be given as

$$\tau_s = \mu_s[\nabla\mathbf{U}_s + (\nabla\mathbf{U}_s)^{\mathrm{T}}] + \left(\lambda_s - \frac{2}{3}\mu_s\right)(\nabla \cdot \mathbf{U}_s)\mathbf{I} \tag{4.11}$$

where μ_s is the solid phase shear viscosity and λ_s is the solid bulk viscosity. The bulk viscosity λ_s is calculated with the expression of Lun et al. [18].

$$\lambda_s = \frac{4}{3}\alpha_s^2 \rho_s d_{\mathrm{p}} g_0 (1+e)\sqrt{\Theta/\pi} \tag{4.12}$$

The solid-phase shear viscosity μ_s is calculated by the sum of a collisional and a kinetic contribution [17] :

$$\mu_s = \mu_{s,\mathrm{col}} + \mu_{s,\mathrm{kin}} \tag{4.13}$$

with

$$\mu_{s,\mathrm{col}} = \frac{4}{5}\alpha_s \rho_s d_{\mathrm{p}} g_0 (1+e)\sqrt{\Theta/\pi} \tag{4.14}$$

$$\mu_{s,\mathrm{kin}} = \frac{10\rho_s d_s \sqrt{\Theta\pi}}{96\alpha_s g_0(1+e)}\left[1 + \frac{4}{5}\alpha_s g_0(1+e)\right]^2 \tag{4.15}$$

The granular particle pressure p_s is calculated according to [18]

$$p_s = \alpha_s \rho_s \Theta + 2\rho_s \alpha_s^2 g_0 \Theta(1+e) \tag{4.16}$$

where e is the particle-particle restitution coefficient and g_0 is the radial distribution function. The expression of g_0 proposed by Lun and Savage [18] is given as

$$g_0 = \left(1 - \alpha_s/\alpha_{s,\mathrm{max}}\right)^{-2.5\alpha_{s,\mathrm{max}}} \tag{4.17}$$

The radial distribution function g_0 will become infinite to avoid unphysically high values of α_s, when the solid volume fraction α_s reaches the particle packing limit $\alpha_{s,\mathrm{max}}$.

In the case of dense gas-solid flows, some particles are often closely packed together and the granular flow is not adequately described only by the above kinetic theory. In regions with high solid volume fraction, the particle frictional stresses will dominate the solid phase stress generation. Therefore, it is necessary to consider the frictional stresses because of the dense granular flows used in this work. Similar to the shear stresses, frictional stresses consist of frictional shear stress and frictional normal stress (i.e., frictional solid pressure). The frictional stresses are simply added to the solid stresses calculated from KTGF when the solid volume fraction exceeds a critical value $\alpha_{s,\mathrm{min}}$. The solid frictional pressure p_{f} and frictional viscosity μ_{f} proposed by Srivastava and Sundaresan [19] are applied as follows:

$$p_{\mathrm{f}} = 0.1\alpha_s F_{\mathrm{r}}\frac{(\alpha_s - \alpha_{s,\mathrm{min}})^{\mathrm{n}}}{(\alpha_{s,\mathrm{max}} - \alpha_s)^{\mathrm{p}}} \tag{4.18}$$

$$\mu_{\mathrm{f}} = \frac{p_{\mathrm{f}}\sqrt{2}\sin\phi_{\mathrm{f}}}{2\sqrt{\mathbf{S}_s : \mathbf{S}_s + \dfrac{\Theta}{d_{\mathrm{p}}^2}}} \tag{4.19}$$

where $F_r = 0.05$ N/m^2, n $= 2$, p $= 5$, ϕ_f is the internal frictional angle and $\mathbf{S}_s$ is the strain rate of the solid phase which can be calculated as

$$\mathbf{S}_s = \frac{1}{2}[\nabla\mathbf{U}_s + (\nabla\mathbf{U}_s)^{\mathrm{T}}] - \frac{1}{3}(\nabla \cdot \mathbf{U}_s)\mathbf{I} \tag{4.20}$$

4.3.2 Monolayer energy dissipation erosion model

Numerous models for predicting erosion of stationary surfaces in fluidized beds have been suggested in the literature. Lyczkowski and Bouillard [1] classified various erosion modeling methods into the two main approaches, i.e., single-particle models and energy dissipation models. It was reported that the energy dissipation erosion models can provide reliable trends on the overall erosion rates [6].

The monolayer energy dissipation erosion model is used to simulate the erosion rates of the tube surfaces, which was essentially derived by Bouillard et al. [20], as further refined by Bouillard and Lyczkowski [21]. The model formulation is given by Eq.(4.21)

$$\dot{E}_{\mathrm{MED}} = C\left(-\frac{dE_p}{dt}\right)\frac{d_p}{E_{\mathrm{sp}}} = C\left[(\alpha_s\tau_s):\nabla\mathbf{U}_s + \frac{\beta\mathbf{U}_s^2}{2}\right]\frac{d_p}{H_v} \tag{4.21}$$

where E_p is the particle kinetic energy, d_p is the particle diameter, E_{sp} is the specific energy of the tube surface, and H_v is the Vickers hardness of the tube surface. In this model it is assumed that the rate of available energy responsible for erosion in the vicinity of an eroding surface is a constant fraction of the kinetic energy dissipation rate. This constant fraction C represents the fraction of solid particles in contact with the surface that cause surface erosion. Lyczkowski and Bouillard recommended 0.1 as a suitable value for C [2]. The first term in the sum on the right-hand side of Eq.(4.21) represents the rate of irreversible conversion to internal energy due to solid viscous dissipation. The second term represents the rate of dissipation of kinetic energy due to interphase drag dissipation [21]. According to [21], the solid viscous dissipation is much smaller than the interphase drag dissipation at and above the minimum fluidization. In the vicinity of a tube surface, the gas phase velocity is assumed to be zero by the non-slip boundary condition for the gas phase velocity. Hence, the dissipation function $\beta(\mathbf{U}_g - \mathbf{U}_s)^2/2$ in the interphase drag dissipation term becomes $\beta\mathbf{U}_s^2/2$ as written in Eq.(4.21).

4.4 Simulation procedure

4.4.1 Simulation setup

All the simulations of hydrodynamics and erosion in the bubbling fluidized bed are performed using a two-fluid solver (`twoPhaseEulerFoam`) implemented in the open-source CFD package OpenFOAM$^{\circledR}$ [22]. OpenFOAM (Open Field Operation And Manipulation) is a flexible and efficient C++ library for the customization and extension for the CFD applications. The

`twoPhaseEulerFoam` solver is developed for simulating the systems of two incompressible fluid phases with one dispersed phase, e.g., solid particles in a gas-solid fluidized bed. The kinetic theory models of the granular flow have already been implemented into this solver for modeling the hydrodynamic properties of the solid phase. The two-fluid modeling framwork in OpenFOAM has been developed and applied for simulating gas-liquid flows [23, 24]. Further numerical and theoretical details of this solver is found in the technical report of Weller [25].

The particle frictional stress models proposed by Srivastava and Sundaresan [19] are implemented into the `twoPhaseEulerFoam` solver. The calculated frictional stress terms are added to the kinetic stress terms when the solid volume fraction exceeds a specified critical value $\alpha_{s,\mathrm{min}}$. To limit the over-packing of the particles, the frictional pressure term is introduced into the dispersed phase continuity equation. The implicit treatment of the frictional pressure term is crucial in enforcing the particle packing limit to ensure numerical stability. To calculate the erosion rates of the tube surface, the implementation of the monolayer kinetic energy dissipation model is carried out using the results obtained by the hydrodynamic models. The physical properties and model parameters are listed in Table 4.1.

Table 4.1: Physical properties and model parameters used for the simulations

Symbol	Description	Value
ρ_g	Gas density	0.468 kg/m^3
ρ_s	Particle density	2600 kg/m^3
μ_g	Gas viscosity	4.1×10^{-5} Pa·s
d_{p}	Particle diameter	7×10^{-4} m
D	Diameter of a immersed tube	0.0264 m
H	Bed height at minimum fluidization	0.86 m
H_{v}	Vickers hardness	1.08×10^{10} Pa
U_{mf}	Minimum fluidization velocity	0.25 m/s
$\alpha_{s,\mathrm{mf}}$	Minimum fluidization solid volume fraction	0.54
U_{fl}	Superficial gas velocity	0.4, 0.65, 1.0 m/s
e	Particle-particle restitution coefficient	0.96
$\alpha_{s,\mathrm{max}}$	Particle packing limit	0.63
$\alpha_{s,\mathrm{min}}$	Critical value for frictional stresses	0.50
ϕ_{f}	Internal friction angle	28.5º
e_{w}	Particle-wall restitution coefficient	0.6, 0.8, 1.0
ϕ	Specularity coefficient	0.3, 0.6, 0.9

In view of extremely large computational effort required for 3D simulations, a 2D unstructured mesh is used to capture the profiles around the tubes. It was reported that an acceptable grid-independent solution can be obtained when a fine enough grid resolution (approximately ten particles in diameter) is used for gas-solid flow systems [26]. The grid size around the

surface of one circular tube is set to be 4.15 mm, which is almost six times larger than the particle diameter ($d_{\mathrm{p}} = 7 \times 10^{-4}$ m). The following simulations in this work are performed based on the above mesh with 13286 hexahedral cells. The transient simulations are conducted with an adaptive time stepping technique. The time step is limited by the maximum Courant number Co = 0.3. Simulations are carried out for 20 s real time. The time-averaged results are obtained in the last 15 s. The mathematical equations are solved by using a 64 bit computer with Intel Xeon Quad Core 3.47 GHz CPU and 11.8 GB RAM.

4.4.2 Initial and boundary conditions

The initial conditions for all simulation cases are set to be at the minimum fluidization conditions with bed voidage of 0.46 and bed height of 0.86 m. Initially, the velocities of both gas and solid phases in the bed are set to be 0 m/s. The initial values of the granular temperature in the bed are set to be 0.0001 m^2/s^2.

At the inlet of the fluidized bed, the gas and solid velocities, granular temperature and solid volume fraction are specified as Dirichlet boundary conditions. The bed pressure at the inlet is specified using zero-gradient Neumann conditions. At the bed outlet, the bed pressure is specified as atmospheric pressure, and the zero-gradient boundary condition is applied for solid volume fraction, granular temperature and gas and solid velocities.

At the bed walls and tube surfaces, the zero-gradient boundary condition is used for solid volume fraction and bed pressure. The non-slip Dirichlet condition is applied for the gas phase velocity. The partial slip boundary conditions proposed by Johnson and Jackson [27] are used for the granular temperature and solid phase velocity. At the wall surfaces, the normal velocity of solid phase is set to be 0 m/s. The tangential velocity and granular temperature of solid phase at the wall are specified as follows:

$$\mathbf{U}_{st,\mathrm{w}} = -\frac{6\mu_s \alpha_{s,\max}}{\phi \pi \rho_s \alpha_s g_0 \sqrt{3\Theta}} \frac{\partial \mathbf{U}_{st,\mathrm{w}}}{\partial n} \tag{4.22}$$

$$\Theta_{\mathrm{w}} = -\frac{k_s \Theta}{\gamma_{\mathrm{w}}} \frac{\partial \Theta_{\mathrm{w}}}{\partial n} + \frac{\sqrt{3}\pi \phi \rho_s \alpha_s \mathbf{U}_{s,slip}^2 g_0 \Theta^{3/2}}{6\gamma_{\mathrm{w}} \alpha_{s,\max}} \tag{4.23}$$

with

$$\gamma_{\mathrm{w}} = \frac{\sqrt{3}\pi (1 - e_{\mathrm{w}}^2) \alpha_s \rho_s g_0 \Theta^{3/2}}{4\alpha_{s,\max}} \tag{4.24}$$

where e_{w} is the solid-wall restitution coefficient and ϕ is the specularity coefficient.

4.5 Results and discussion

4.5.1 Bubble characteristics

In order to predict tube erosion rates, the hydrodynamic properties of both solid and bubble phases are needed as inputs for the erosion modeling. The tube erosion is directly related

to the bubble-induced particle motion. Hence, accurately predicting bubble behaviors is a prerequisite to the erosion modeling. For this reason, it is worthwhile to analyse the bubble characteristics in the bed firstly.
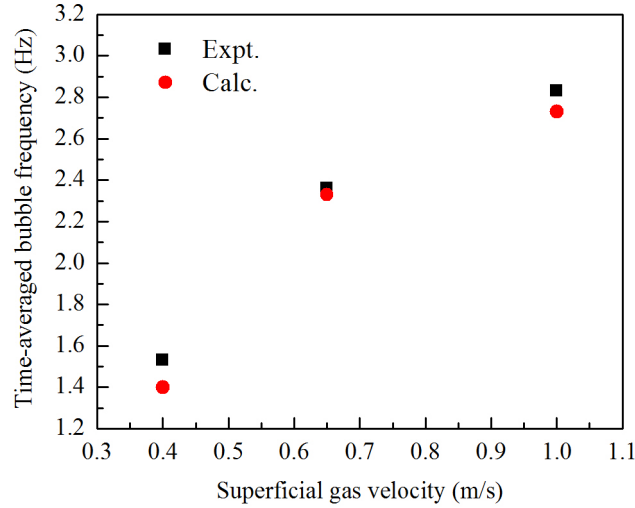
Figure 4.2: Comparison of the simulated mean bubble frequency with the experimental data at three superficial gas velocities.
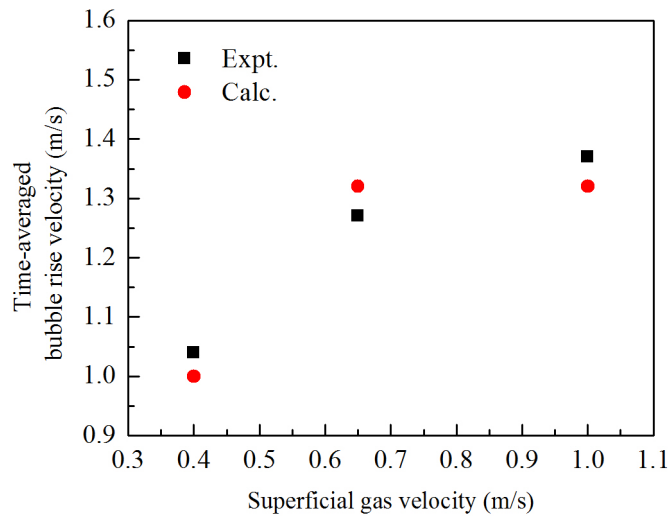
Figure 4.3: Comparison of the simulated mean bubble rise velocity with the experimental data at three superficial gas velocities.

Before determining the bubble frequency, a criterion demarcating the boundary of the bubble and solid phases should be firstly defined. Different values of the bubble boundary have been adopted in the literature to indicate the existence of bubbles [28, 29]. The voidage of 0.85 is adopted to determine the bubble boundary. Figure 4.2 presents the comparison of simulated time-averaged bubble frequency with the experimental data at three different superficial gas

velocities (U_{fl} = 0.4, 0.65 and 1.0 m/s). The time-averaged bubble frequency is obtained by using the profiles of the instantaneous solid volume fractions in the last 15 s of the simulation time. Figure 4.2 reveals that the simulated values of bubble frequency are in good agreement with the experimental data. The bubble frequency increases with the increase in superficial gas velocities, i.e., there are more bubbles formed at larger superficial gas velocities.

Local bubble rise velocities are also important to characterize the bubble characteristics and bed hydrodynamics. Figure 4.3 shows the simulated bubble rise velocities at different superficial gas velocities comparing with the experimental data. According to the experimental measuring method [16], the bubble rise velocity can be measured through dividing the distance between the two capacitors by the time shift of the occurrences of two consecutive bubbles. The instantaneous bubble rise velocities are calculated between two different locations with a vertical distance of 0.015 m that equals to the distance between the two capacitors. As indicated in Figure 4.3, the simulated time-averaged bubble rise velocities qualitatively agree with the experimental results at three different superficial gas velocities, and the bubble rise velocity becomes larger when the gas velocity is increased.

In summary, the complicated hydrodynamics of gas-solid flows around such a dense tube bundle can be well predicted by the Eulerian-Eulerian two-fluid model. Consequently, the validity of the hydrodynamic information used for the erosion modeling can be guaranteed.

4.5.2   Tube erosion modeling

The variation of the measured and simulated erosion rates with the circumferential angles for the target tube No. 21 is presented in Figure 4.4. It is exposed to the superficial gas velocity (U_{fl} = 0.4 m/s). The most severe erosion occurs on the circumferential positions of about 140º and 220º. The smaller erosion rates are found at the lowest part of the tube, while the smallest erosion rates are obtained at the upper parts of the tube.
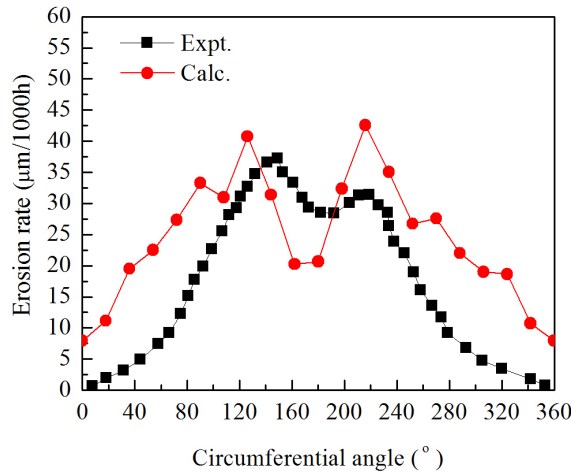
Figure 4.4: Comparison of the predicted erosion rates with experimental data at different circumferential positions of tube No.21 (U_{fl} = 0.4 m/s).

Figure 4.5 gives the measured and simulated erosion rates of the target tube No. 18. They are obtained at the same superficial gas velocity. Both the experimental data and simulations also show the similar trend of the erosion rates to those in Figure 4.4.
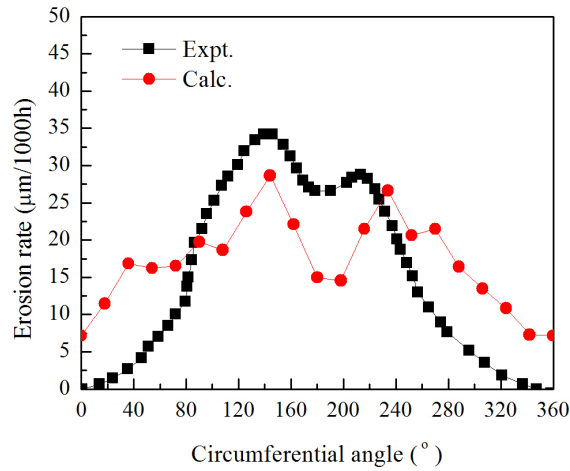
Figure 4.5: Comparison of the predicted erosion rates with experimental data at different circumferential positions of tube No.18 (U_{fl} = 0.4 m/s).

Compared with the experimental data, the trend of the erosion rates around the two tubes is well captured by the simulations, and the quantitative agreement between the experimental and simulated results can also be obtained. However, there still exist some overpredictions on the erosion rates at the upper part of the tube. Moreover, the erosion rates at the lowest part of the tube are underestimated. The disagreement could possibly be due to the 2D simulation method used here. This is because the dispersion of the gas and solid phases is only restricted in the 2D region.
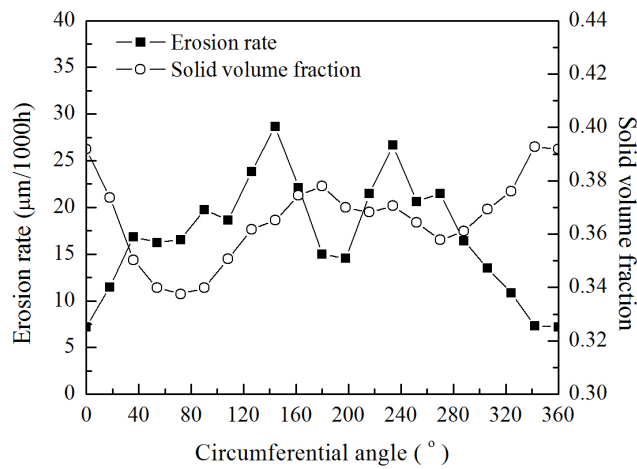
Figure 4.6: Predicted values of time-averaged erosion rates and solid volume fractions at different circumferential positions of tube No.18 (U_{fl} = 0.4 m/s).

The time-averaged erosion rates and solid volume fractions at various positions along the tube surface are given in Figure 4.6. There is a similar tendency in the erosion rate and solid volume fraction at the lower part of the tube. Hence, the erosion rates are closely related to the solid volume fractions around the tubes. The solid particles easily achieve the packing at the upper part of the tube, which in turn results in the large values of solid volume fraction.
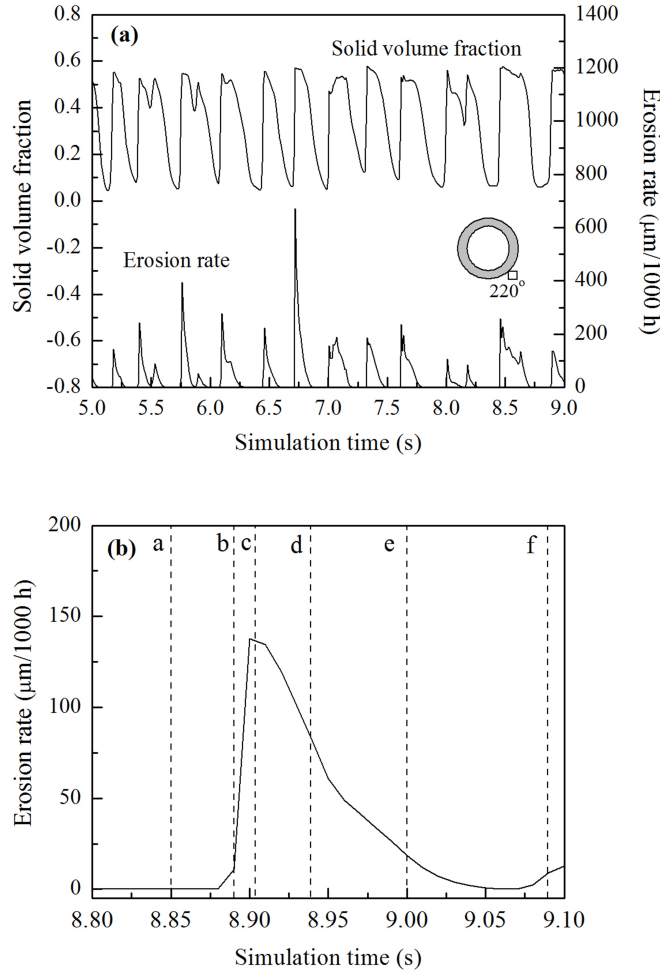
Figure 4.7: (a) Predicted solid volume fractions and erosion rates at the circumferential position 220° of tube No.21 ($U_{fl} = 0.4$ m/s); (b) Change of erosion rates in a short time interval.

Figure 4.7a illustrates the local instantaneous solid volume fraction and erosion rate as a function of time at the circumferential position of 220°. The occurrence of the erosion rate peaks also closely follows the variation in the solid volume fraction. The peak of erosion rate emerges when the solid volume fraction suddenly increases from the lowest value, i.e., the tube is being hit by the solid particles entrained by the wake of a bubble. Most of the peaks of the erosion rate are followed by the smoothly varying profiles of the erosion rate which was also observed by Gustavsson and Almstedt [8]. Figure 4.7b indicates a short time interval when just one peak of the erosion rate occurs which is obtained from Figure 4.7a.

To investigate the influence of bubble behaviors on erosion rate, the time sequence of the solid volume fraction around the target tube No.21 is given in Figure 4.8. Figure 4.8a presents that the tube is immersed in the bubble phase. The corresponding erosion rate is low at this moment (see Figure 4.7b). In Figure 4.8b, it can be seen that a dense stream of particles is approaching to the target tube from below and the target tube is very near to the bubble wake. Figure 4.8c reveals that the tube is being hit by the dense solid particles. Hence, the corresponding erosion rate reaches the maximum value in Figure 4.7b. Due to the energy dissipation, the erosion rate decreases (Figure 4.7b, 4.8d). Figure 4.8e presents that a new bubble is approaching to the tube from below, causing the surrounding particles to move away as it expanded. Then, the erosion rate further decreases. It can be observed in Figure 4.8f that a new stream of the solid particles is formed again following the bubble, and the erosion rate starts to increase at this moment (Figure 4.7b). Based on the above analysis, the erosion rate greatly depends on the bubble behaviors around the tube. Overall, the accurate hydrodynamic simulation is definitely the key step to determine the tube erosion rates.
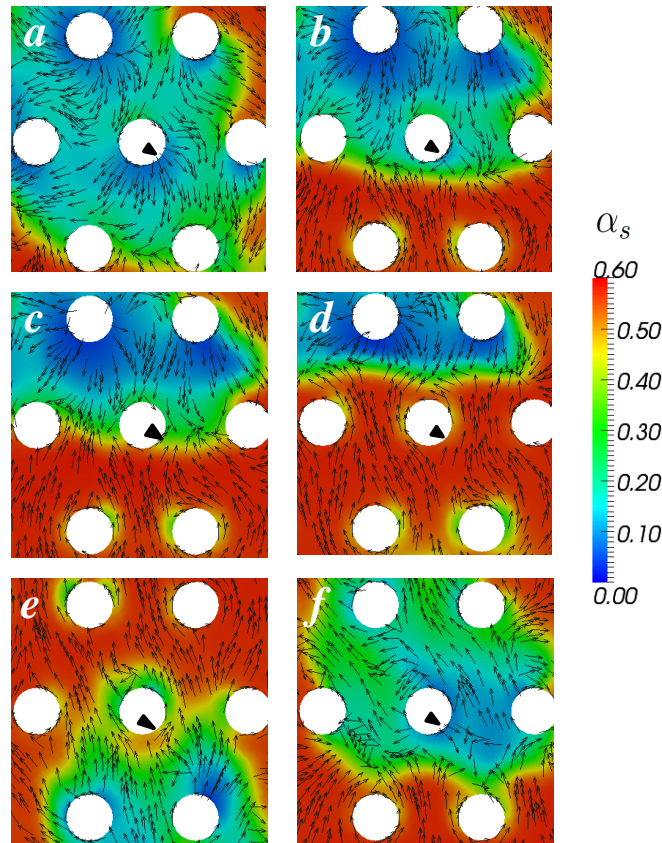
Figure 4.8: Contours of the simulated solid volume fraction and particle velocity around tube No.21 at different time ($U_{fl} = 0.4$ m/s).
(a) 8.85 s (b) 8.89 s (c) 8.90 s (d) 8.93 s (e) 9.00 s (f) 9.09 s.

4.5.3 Effect of particle-wall restitution coefficient

The wall boundary conditions have an important influence on CFD modeling of gas-solid fluidized beds. However, no work has been reported on the influence of wall boundary conditions on erosion rates of the immersed tube surface. Three kinds of wall boundary conditions are usually used in numerical simulations of fluidized beds (i.e. non-, partial- and free-slip). The partial slip wall boundary condition proposed by Johnson and Jackson [27], which is the most widely used, requires the particle-wall restitution coefficient e_w and the specularity coefficient ϕ to be specified.

The particle-wall restitution coefficient e_w serves as a characteristic measure of the inelasticity degree of the particle-wall collisions, whose value may be varied from zero, representing perfectly inelastic collisions, to one for elastic collisions. Figure 4.9a displays the simulated results of erosion rates when using the different values of particle-wall restitution coefficient. Tartan and Gidaspow [30] estimated the particle-wall restitution coefficient as 0.6 from experiments by assuming that the walls were softer than the particles. The values of 0.6, 0.8 and 1.0 are employed in the test cases. It can be observed in Figure 4.9a that the increase in the particle-wall restitution coefficient does not result in an evident change in the simulated erosion rates around the target tube. Therefore, little attention can paid on the setting of particle-wall restitution coefficient.
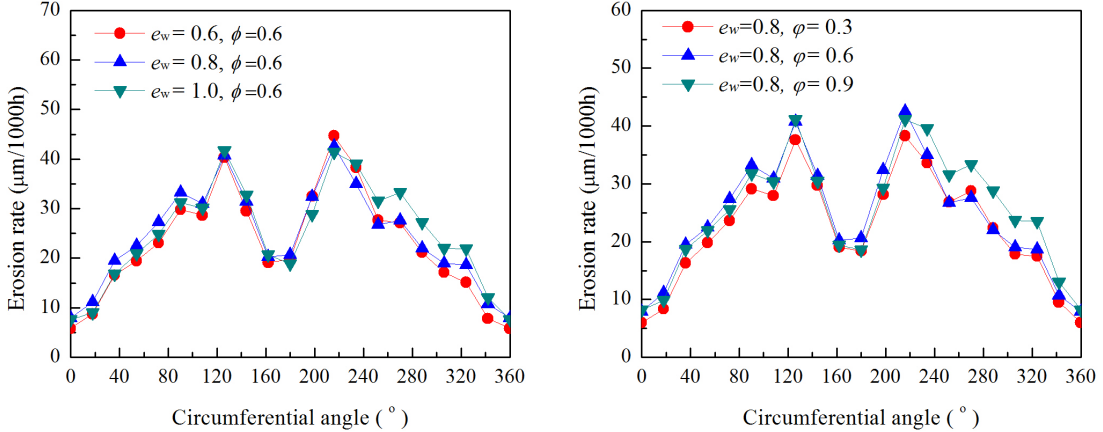
(a) Effect of particle-wall restitution coefficient on the simulated erosion rates of tube No.21.

(b) Effect of specularity coefficient on the simulated erosion rates of tube No.21.

Figure 4.9: Effect of particle-wall restitution coefficient and specularity coefficient.

4.5.4 Effect of specularity coefficient

The specularity coefficient ϕ is used to represent the momentum transfer between walls and particles. When its value is set to be zero, the perfect smooth wall (free-slip condition) is assumed, and its value of unity represents the non-slip wall boundary condition. Li et al. [28] studied the influence of different specularity coefficients on the flow dynamics in bubbling

fluidized beds such as bed expansion, local voidage, solid velocity and bubble diameter and bubble rise velocity. Bahramian et al. [31] also investigated the influence of different particle-wall boundary conditions on a conical fluidized bed unit. They reported that the numerical predictions using free-slip boundary conditions agreed reasonably well with the measured pressure-drop, especially at superficial gas velocities larger than the minimum fluidization velocity. Moreover, the simulated results of the mean axial solid velocity were in better agreement with the experimental data when using the free-slip boundary condition.

The values of specularity coefficient are set to be 0.3, 0.6 and 0.9 in the test cases. As indicated in Figure 4.9b, there are also no large differences in the simulated erosion rates for the three cases. Thus, the specification of the specularity coefficient also has little influence on the simulated results of tube erosion rate.

4.6   Conclusions

Tube erosion of a bubbling fluidized bed with densely arranged tubes is simulated using the Eulerian-Eulerian two-fluid model with a monolayer kinetic energy dissipation model. The main conclusions are as follows:

(1) The simulated time-averaged bubble frequency and bubble rise velocity at three superficial gas velocities are in good agreement with the experimental data reported in the literature. Hence, the hydrodynamics and bubble characteristics are well simulated by the extended `twoPhaseEulerFoam` solver implemented in the OpenFOAM package.

(2) Good agreement between the calculated and measured erosion rates is also obtained for the two target tubes No. 18 and No. 21 at the superficial gas velocity $U_{\mathrm{fl}} = 0.4$ m/s. The erosion rates are closely related to the solid volume fractions around the tube. The study of the influence of the bubble behaviors on erosion rates shows that the erosion rate also depends strongly on the bubble behaviors around the tube. The above coupled CFD and erosion models can provide reasonable predictions of tube erosion rate in the fluidized bed with dense tube bundles.

(3) The sensitivity study of wall boundary conditions used in the simulations reveals that there exist no large differences in the simulated results of erosion rate when using different values of particle-wall restitution coefficient and specularity coefficient.

Literature

[1] R. W. Lyczkowski, J. X. Bouillard, State-of-the-art review of erosion modeling in fluid/solids systems, Progress in Energy and Combustion Science 28 (2002) 543–602.

[2] R. W. Lyczkowski, J. X. Bouillard, Scaling and guidelines for erosion in fluidized beds, Powder Technology 125 (2002) 217–225.

[3] D. G. Rong, M. Horio, Behavior of particles and bubbles around immersed tubes in a fluidized bed at high temperature and pressure: a DEM simulation, International Journal of Multiphase Flow 27 (2001) 89–105.

[4] J. Jin, J. R. Fan, X. Y. Zhang, K. F. Cen, Numerical simulation of the tube erosion resulted from particle impacts, Wear 250 (2001) 114–119.

[5] J. M. Ding, R. W. Lyczkowski, Three-dimensional kinetic theory modeling of hydrodynamics and erosion in fluidized beds, Powder Technology 73 (1992) 127–138.

[6] R. W. Lyczkowski, S. Folga, S. L. Chang, J. X. Bouillard, C. S. Wang, G. F. Berry, D. Gidaspow, State-of-the-art computation of dynamics and erosion in fluidized bed tube banks. In: 10th International Conference on Fluidized Bed Combustion, ASME, New York, USA, 1989.

[7] B. E. Lee, J. Y. Tu, C. A. J. Fletcher, On numerical modelling of particle-wall impaction in relation to erosion prediction Eulerian versus Lagrangian method, Wear 252 (2002) 179–188.

[8] M. Gustavsson, A. E. Almstedt, Two-fluid modeling of cooling-tube erosion in a fluidized bed, Chemical Engineering Science 55 (2000) 867–879.

[9] D. Achim, A. K. Easton, M. P. Schwarz, P. J. Witt, A. Zakhari, Tube erosion modeling in a fluidized bed, Applied Mathematical Modeling 26 (2002) 191–201.

[10] Y. R. He, W. B. Zhan, Y. H. Zhao, H. L. Lu, I. Schlaberg, Prediction on immersed tubes erosion using two-fluid model in a bubbling fluidized bed, Chemical Engineering Science 64 (2009) 3072–3082.

[11] T. W. Asegehegn, M. Schreiber, H. J. Krautz, Numerical simulation and experimental validation of bubble behavior in 2D gas-solid fluidized beds with immersed horizontal tubes, Chemical Engineering Science 66 (2011) 5410–5427.

[12] T. W. Li, J.-F. Dietiker, Y. M. Zhang, M. Shahnam, Cartesian grid simulations of bubbling fluidized beds with a horizontal tube bundle, Chemical Engineering Science 66 (2011) 6220–6231.

[13] R. Yusuf, B. Halvorsen, M. C. Melaaen, Eulerian-Eulerian simulation of heat transfer between a gas-solid fluidized bed and an immersed tube-bank with horizontal tubes, Chemical Engineering Science 66 (2011) 1550–1564.

[14] J. Wiman, B. Mahpour, A. E. Almstedt, Erosion of horizontal tubes in a pressurized fluidized bed-influence of pressure, fluidization velocity and tube bank geometry, Chemical Engineering Science 50 (1995) 3345–3356.

[15] J. Wiman, A. E. Almstedt, Hydrodynamics, erosion and heat transfer in a pressurized fluidized bed: influence of pressure, fluidization velocity, particle size and tube bank

geometry, Chemical Engineering Science 52 (1997) 2677–2695.

[16] K. Johansson, R. Norling, A. Hjörnhede, A. E. Almstedt, F. Johnsson, A. Nylund, Hydrodynamics and steel tube wastage in a fluidized bed at elevated temperature, Chemical Engineering Science 59 (2004) 31–40.

[17] D. Gidaspow, Multiphase Flow and Fluidization, 1st Edition, Academic Press, New York, 1994.

[18] C. K. K. Lun, S. B. Savage, The effects of an impact velocity dependent coefficient of restitution on stresses developed by sheared granular materials, Acta Mechanica 63 (1986) 15–44.

[19] A. Srivastava, S. Sundaresan, Analysis of a frictional-kinetic model for gas-particle flow, Powder Technology 129 (2003) 72–85.

[20] J. X. Bouillard, R. W. Lyczkowski, S. Folga, D. Gidaspow, G. F. Berry, Hydrodynamics of erosion of heat exchanger tubes in fluidized bed combustors, The Canadian Journal of Chemical Engineering 67 (1989) 218–229.

[21] J. X. Bouillard, R. W. Lyczkowski, On the erosion of heat exchanger tube banks in fluidized-bed combustors, Powder Technology 68 (1991) 37–51.

[22] OpenCFD, OpenFOAM - The Open Source CFD Toolbox - User's Guide, OpenCFD Ltd., United Kingdom, 2010.

[23] H. Marschall, R. Mornhinweg, A. Kossmann, S. Oberhauser, K. Langbein, O. Hinrichsen, Numerical simulation of dispersed gas/liquid flows in bubble columns at high phase fractions using OpenFOAM Part I - Modeling basics, Chemical Engineering & Technology 34 (2011) 1311–1320.

[24] H. Marschall, R. Mornhinweg, A. Kossmann, S. Oberhauser, K. Langbein, O. Hinrichsen, Numerical simulation of dispersed gas/liquid flows in bubble columns at high phase fractions using OpenFOAM Part II - Numerical simulations and results, Chemical Engineering & Technology 34 (2011) 1321–1327.

[25] H. G. Weller, Derivation, modeling and solution of the conditionally averaged two-phase flow equations, Tech. rep., OpenCFD Ltd. (2005).

[26] A. T. Andrews, P. N. Loezos, S. Sundaresan, Coarse-grid simulation of gas-particle flows in vertical risers, Industrial & Engineering Chemistry Research 44 (2005) 6022–6037.

[27] P. C. Johnson, R. Jackson, Frictional-collisional constitutive relations for granular materials, with application to plane shearing, Journal of Fluid Mechanics 176 (1987) 67–93.

[28] T. W. Li, J. Grace, X. T. Bi, Study of wall boundary condition in numerical simulations of bubbling fluidized beds, Powder Technology 203 (2010) 447–457.

[29] T. McKeen, T. Pugsley, Simulation and experimental validation of a freely bubbling bed of FCC catalyst, Powder Technology 129 (2003) 139–152.

[30] M. Tartan, D. Gidaspow, Measurement of granular temperature and stresses in risers, AIChE Journal 50 (2004) 1760–1775.

[31] A. Bahramian, M. Kalbasi, M. Olazar, Influence of boundary conditions on CFD simulation of gas-particle hydrodynamics in a conical fluidized bed unit, International Journal of Chemical Reactor Engineering 7 (2009) 1–27.

Chapter 5

CFD simulation of the hydrodynamics and methanation reactions in a fluidized bed reactor for the production of synthetic natural gas

This chapter originates from the following publication:

Abstract

Numerical investigations of hydrodynamics and kinetic reactions in a fluidized bed methanation reactor are carried out by coupling methanation kinetics with the two-fluid flow model. The gas-solid reacting flow models are implemented within OpenFOAM. The grid resolution is investigated using 2D and 3D meshes. The bed height is reasonably predicted with the Gidaspow and Syamlal models. Simulated results are compared against experimental data in literature. The simulated axial species concentrations agree well with the measured results at the end of the bed. The effects of different operating parameters are evaluated using the established models. The increase in the gas inlet velocity results in more dilute solid concentration and larger bed expansion. The weak bed expansion results from the methanation reaction with gas volume reduction. The methane concentration is increased when increasing catalyst inventory in the reactor. The addition of water into the feedstock with low H_2/CO ratio benefits the methanation reaction.

5.1 Introduction

Fluidized beds are extensively employed in gas-solid processes in which large heat and mass transfer rates are highly required. The fluidized bed methanation of syngas from coal or biomass gasification to produce synthetic natural gas (SNG) is an example to deal with fast and highly exothermic reactions [1–3]. The complex reacting flows in fluidized bed methanation reactors would cause great difficulties in rational reactor design and scaleup. Comparing with experimental studies, numerical modeling is more flexible and less expensive, which is becoming a promising route for predicting gas-solid hydrodynamics and catalytic reactions in the fluidized bed reactors.

Many studies involving simulations of syngas methanation processes have been performed with different models. Previously, simple reactor models were usually applied in modeling fluidized bed methanation reactors. Cobb and Streeter [4] used the perfectly mixed reactor model to simplify the hydrodynamics in fluidized beds. Bellagi [5] and Kai et al. [6] employed the original homogeneous two-phase fluidized bed model to simulate methanation reactors. Kopyscinski et al. [7, 8] applied the one-dimensional homogeneous two-phase model to simulate their fluidized bed methanation reactor. However, the above simplified reactor models largely depend on empirical correlations and only reactor-scale information is obtained for the flows and reactions. Advanced modeling techniques based on the first principles are demanded to obtain comprehensive knowledge on fluidized bed methanation reactors.

Nowadays, computational fluid dynamics (CFD) provides the state-of-the-art capabilities of simulating gas-solid hydrodynamics in fluidized bed reactors. CFD strategies used for gas-solid flows are generally classified into two main categories, i.e., Eulerian-Eulerian and Eulerian-Lagrangian methods. In the Eulerian-Eulerian method, the particle phase is treated as a continuous fluid. The averaged mass and momentum balance equations allow for efficiently simulating large-scale reactors. Concerning the Eulerian-Lagrangian approach, the motion of solid particle is calculated individually with Newton's equations of motion. Typically, the discrete element method (DEM) is widely adopted to solve each particle's trajectory.

To date, very few CFD-based studies are carried out to model and simulate fluidized bed methanation reactors. Wu et al. [9] applied the CFD-DEM coupled method to simulate a lab-scale fluidized bed used for the syngas methanation process. Zhang et al. [10] incorporated methanation reaction kinetics into an in-house CFD-DEM code to investigate the effect of reduction in volumetric flow in a bubbling fluidized bed reactor. However, in their work, model validations were not conducted using species concentrations measured in the reactors. Furthermore, the CFD-DEM method requires massive computational effort for industrial-scale reactors. Alternatively, the Eulerian-Eulerian two-fluid method is a good choice to simulate the complex interaction between gas-solid hydrodynamics and chemical kinetics in industrial fluidized beds. In the previous work, no reports were found on the simulations of

fluidized bed methanation reactors by means of the computationally economical Eulerian-Eulerian method. Hence, development and validation of a gas-solid Eulerian-based model coupled with methanation kinetics are very necessary for methanation reactor design.

In this work, a numerical solver based on the open source CFD package OpenFOAM is developed by coupling the Eulerian-Eulerian two-fluid model with methanation reaction kinetics. A lab-scale fluidized bed methanation reactor is simulated with the test of various grids and drag force models. Simulation results of axial species concentrations are compared with experimental data found in the literature. The effects of inlet flow rate, catalyst inventory and feed composition are also numerically investigated.

5.2 Mathematical models

5.2.1 Governing equations

In the fluidized bed methanation reactor, there exist two phases, i.e., gas phase including the reactant gases, product gases and inert gas, solid phase including the catalyst particles. The continuity equations of gas and solid phases are written as follows:

$$\frac{\partial(\alpha_g\rho_g)}{\partial t} + \nabla \cdot (\alpha_g\rho_g\mathbf{U}_g) = R_g \tag{5.1}$$

$$\frac{\partial(\alpha_s\rho_s)}{\partial t} + \nabla \cdot (\alpha_s\rho_s\mathbf{U}_s) = R_s \tag{5.2}$$

where α, ρ and $\mathbf{U}$ are the phase volume fraction, density and velocity, respectively. R_g and R_s are the mass transfer source terms due to catalytic reactions.

The momentum balance equations of gas and solid phases are given as

$$\frac{\partial(\alpha_g\rho_g\mathbf{U}_g)}{\partial t} + \nabla \cdot (\alpha_g\rho_g\mathbf{U}_g\mathbf{U}_g) = -\alpha_g\nabla p + \nabla \cdot (\alpha_g\tau_g) + \beta(\mathbf{U}_s - \mathbf{U}_g) + \alpha_g\rho_g\mathbf{g} \tag{5.3}$$

$$\frac{\partial(\alpha_s\rho_s\mathbf{U}_s)}{\partial t} + \nabla \cdot (\alpha_s\rho_s\mathbf{U}_s\mathbf{U}_s) = -\alpha_s\nabla p - \nabla p_s + \nabla \cdot (\alpha_s\tau_s) + \beta(\mathbf{U}_g - \mathbf{U}_s) + \alpha_s\rho_s\mathbf{g} \tag{5.4}$$

where β is the interphase momentum transfer coefficient.

To close the solid phase momentum equation, the descriptions of solid shear stress τ_s and solid pressure p_s in Eq.(5.4) are required. When the particle motion is dominated by binary collisional interactions, the kinetic theory of granular flow (KTGF) is employed to obtain the properties of solid phase [11].The transport equation of the fluctuation energy of solid phase (also known as granular temperature) is expressed as

$$\frac{3}{2}\left[\frac{\partial(\alpha_s\rho_s\Theta)}{\partial t} + \nabla \cdot (\alpha_s\rho_s\mathbf{U}_s\Theta)\right] = (-p_s\mathbf{I} + \tau_s) : \nabla\mathbf{U}_s + \nabla \cdot (\kappa_s\nabla\Theta) - \gamma_s - J_s \tag{5.5}$$

where Θ is the granular temperature, κ_s is the conductivity of granular temperature, γ_s is the collision dissipation rate of granular temperature, J_s is the dissipation rate of granular temperature resulting from the working of the fluctuating force exerted by the gas through the fluctuating velocity of the particles.

The methanation reactions only take place in the gas phase and no solid species is produced. The gas species transport equation is written using the mass fraction of each species:

$$\frac{\partial(\alpha_g \rho_g Y_{g,i})}{\partial t} + \nabla \cdot (\alpha_g \rho_g \mathbf{U}_g Y_{g,i}) = \nabla \cdot (\alpha_g J_{g,i}) + R_{g,i} \tag{5.6}$$

where $Y_{g,i}$ is the mass fraction of species i in gas phase, $J_{g,i}$ is the species diffusion flux of species i, and $R_{g,i}$ is the reaction rate of species i.

No energy conservation equations are solved because the isothermal flow is assumed in the bubbling fluidized bed reactor. Under the experimental conditions the bed temperature was well controlled at 593 K ($\pm$ 5 K) in the fully developed flow region [7].

5.2.2 Hydrodynamic model closures

The gas phase is assumed as a Newtonian fluid, and its stress tensor is defined using the Newtonian stress-strain relation as

$$\tau_g = \mu_g \big[\nabla \mathbf{U}_g + (\nabla \mathbf{U}_g)^{\mathrm{T}} \big] - \frac{2}{3} \mu_g (\nabla \cdot \mathbf{U}_g) \mathbf{I} \tag{5.7}$$

where μ_g is the shear viscosity of gas phase and $\mathbf{I}$ is the unit tensor. Similarly, the shear stress tensor of solid phase is expressed as

$$\tau_s = \mu_s \big[\nabla \mathbf{U}_s + (\nabla \mathbf{U}_s)^{\mathrm{T}} \big] + \big(\lambda_s - \frac{2}{3} \mu_s \big)(\nabla \cdot \mathbf{U}_s) \mathbf{I} \tag{5.8}$$

where μ_s is the solid shear viscosity and λ_s is the solid bulk viscosity.

The interphase momentum transfer only accounts for the drag force resulting from the velocity differences between two phases. β can be calculated with various drag force functions. These drag force functions were empirically developed. Therefore, their applicability to simulate a specific fluidized bed reactor needs to be evaluated. Here, three different drag force models are tested and compared. First, the Syamlal model was derived by converting the terminal velocity correlations in fluidized or settling beds [12]. Second, the Gidaspow model is a combination of the Ergun equations and the Wen and Yu model [11]. The Ergun equations were derived using the packed-bed pressure drop data [13], whereas the Wen and Yu model was formulated based on the homogeneous expansion of fluidized beds [14]. The third drag force function is the energy minimization multi-scale (EMMS) model proposed by Yang et al. [15]. The EMMS model was developed with the concept of particle clusters. These gas-solid drag relations are given in Table 5.1.

Table 5.1: Interphase momentum transfer coefficients

(a) Syamlal model

$$\beta = \frac{3}{4}C_D\frac{\alpha_g\alpha_s\rho_g}{V_r^2 d_\mathrm{p}}|\mathbf{U}_g - \mathbf{U}_s|$$

$$C_D = \left(0.63 + 4.8\sqrt{\frac{V_r}{\mathrm{Re}}}\right)^2$$

$$V_r = 0.5\left[a - 0.06\mathrm{Re} + \sqrt{(0.06\mathrm{Re})^2 + 0.12\mathrm{Re}(2b - a) + a^2}\right]$$

$$a = \alpha_g^{4.14}, \quad b = \begin{cases} 0.8\alpha_g^{1.28} & \alpha_g \leqslant 0.85 \\ \\ \alpha_g^{2.65} & \alpha_g > 0.85 \end{cases}$$

$$\mathrm{Re} = \frac{\rho_g d_\mathrm{p}|\mathbf{U}_g - \mathbf{U}_s|}{\mu_g}$$

(b) Gidaspow model

$$\beta = \begin{cases} \dfrac{3}{4}\dfrac{C_D\alpha_g\alpha_s\rho_g|\mathbf{U}_g - \mathbf{U}_s|}{d_\mathrm{p}}\alpha_g^{-2.65} & \alpha_s < 0.2 \\ \\ 150\dfrac{\mu_g\alpha_s^2}{\alpha_g^2 d_\mathrm{p}^2} + 1.75\dfrac{\rho_g\alpha_s}{\alpha_g d_\mathrm{p}}|\mathbf{U}_g - \mathbf{U}_s| & \alpha_s \geqslant 0.2 \end{cases}$$

$$C_D = \begin{cases} \dfrac{24}{\alpha_g\mathrm{Re}}[1 + 0.15(\alpha_g\mathrm{Re})^{0.687}] & \alpha_g\mathrm{Re} < 1000 \\ \\ 0.44 & \alpha_g\mathrm{Re} \geqslant 1000 \end{cases}$$

(b) EMMS model

$$\beta = \begin{cases} \dfrac{3}{4}\dfrac{C_\mathrm{D}\alpha_g\alpha_s\rho_g|\mathbf{U}_g - \mathbf{U}_s|}{d_\mathrm{p}}C_{D0}\omega(\alpha_g) & \alpha_g > 0.74 \\ \\ 150\dfrac{\mu_g\alpha_s^2}{\alpha_g^2 d_\mathrm{p}^2} + 1.75\dfrac{\rho_g\alpha_s}{\alpha_g d_\mathrm{p}}|\mathbf{U}_g - \mathbf{U}_s| & \alpha_g \leqslant 0.74 \end{cases}$$

$$C_{D0} = \begin{cases} \dfrac{24}{\alpha_g\mathrm{Re}}[1 + 0.15(\alpha_g\mathrm{Re})^{0.687}] & \alpha_g\mathrm{Re} < 1000 \\ \\ 0.44 & \alpha_g\mathrm{Re} \geqslant 1000 \end{cases}$$

$$\omega(\alpha_g) = \begin{cases} -0.5760 + \dfrac{0.0214}{4(\alpha_g - 0.7463) + 0.0044} & 0.74 \leqslant \alpha_g \leqslant 0.82 \\ \\ -0.0101 + \dfrac{0.0038}{4(\alpha_g - 0.7789) + 0.0040} & 0.82 \leqslant \alpha_g \leqslant 0.97 \\ \\ -31.8295 + 32.8295\alpha_g & \alpha_g > 0.97 \end{cases}$$

Table 5.2: Constitutive equations in the two-fluid granular model

(a) solid pressure

$$p_{s,\mathrm{KTGF}} = \alpha_s \rho_s \Theta [1 + 2(1 + e) g_0 \alpha_s]$$

(b) solid shear viscosity

$$\mu_{s,\mathrm{KTGF}} = \frac{4}{5} \alpha_s^2 \rho_s d_\mathrm{p} g_0 (1 + e) \sqrt{\frac{\Theta}{\pi}} + \frac{10 \rho_s d_\mathrm{p} \sqrt{\Theta \pi}}{96(1 + e) g_0} \left[1 + \frac{4}{5} \alpha_s g_0 (1 + e) \right]^2$$

(c) solid bulk viscosity

$$\lambda_s = \frac{4}{3} \alpha_s^2 \rho_s d_\mathrm{p} g_0 (1 + e) \sqrt{\frac{\Theta}{\pi}}$$

(d) radial distribution function

$$g_0 = \left[1 - \left(\frac{\alpha_s}{\alpha_{s,\mathrm{max}}} \right)^{1/3} \right]^{-1}$$

(e) conductivity of granular temperature

$$\kappa_s = 2 \alpha_s^2 \rho_s d_\mathrm{p} g_0 (1 + e) \sqrt{\frac{\Theta}{\pi}} + \frac{9}{16} \alpha_s^2 \rho_s d_\mathrm{p} g_0 (1 + e) \sqrt{\Theta \pi} + \frac{15}{16} \alpha_s \rho_s d_\mathrm{p} \sqrt{\Theta \pi} + \frac{25}{64} \sqrt{\Theta \pi} \frac{\rho_s d_\mathrm{p}}{(1 + e) g_0}$$

(f) collision dissipation rate of granular temperature

$$\gamma_s = 12(1 - e^2) \frac{\alpha_s^2 \rho_s g_0}{d_\mathrm{p} \sqrt{\pi}} \Theta^{3/2}$$

(g) dissipation rate of granular temperature resulting from fluctuation

$$J_s = \beta \left[3\Theta - \frac{\beta d_\mathrm{p} (\mathbf{U}_s - \mathbf{U}_g)^2}{4 \alpha_s \rho_s \sqrt{\Theta \pi}} \right]$$

(h) frictional solid pressure

$$p_{s,\mathrm{f}} = F_\mathrm{r} \frac{(\alpha_s - \alpha_{s,\mathrm{min}})^\mathrm{n}}{(\alpha_{s,\mathrm{max}} - \alpha_s)^\mathrm{p}}$$

(i) frictional shear viscosity

$$\mu_{s,\mathrm{f}} = \frac{p_{s,\mathrm{f}} \sqrt{2} \sin \phi_\mathrm{f}}{2 \alpha_s \sqrt{\mathbf{S}_s : \mathbf{S}_s + \dfrac{\Theta}{d_\mathrm{p}^2}}}$$

$$\mathbf{S}_s = \frac{1}{2} [\nabla \mathbf{U}_s + (\nabla \mathbf{U}_s)^\mathrm{T}] - \frac{1}{3} (\nabla \cdot \mathbf{U}_s) \mathbf{I}$$

The physical properties of solid phase are described with the kinetic theory of granular flow and the frictional stress models [16–19]. In the so-called rapid granular regime the particles experience short and fast collisions. The kinetic stresses are calculated by means of the kinetic theory of granular flow. In the so-called quasi-static regime with large solid volume fractions, the frictional interaction of particles is dominant. When the solid volume fraction exceeds a critical value $\alpha_{s,\min}$, the frictional stresses are added to the solid kinetic stresses following Johnson et al. [20]:

$$p_s = p_{s,\text{KTGF}} + p_{s,\text{f}} \tag{5.9}$$

$$\mu_s = \mu_{s,\text{KTGF}} + \mu_{s,\text{f}} \tag{5.10}$$

where $p_{s,\text{KTGF}}$ and $\mu_{s,\text{KTGF}}$ are the solid pressure and shear viscosity from the kinetic theory of granular flow. $p_{s,\text{f}}$ and $\mu_{s,\text{f}}$ are the frictional solid pressure and the frictional shear viscosity. The constitutive relations of the kinetic theory of granular flow and the frictional stress models are summarized in Table 5.2.

5.2.3 Methanation kinetics

For the catalytic methanation of carbon monoxide (CO) to methane (CH_4), two global reactions are taken into consideration, i.e., the CO methanation reaction and the water-gas shift reaction.

CO methanation reaction:

$$CO + 3H_2 \leftrightarrow CH_4 + H_2O \quad \Delta H_{298K} = -206.28 \text{kJ/mol} \tag{5.11}$$

water-gas shift reaction:

$$CO + H_2O \leftrightarrow CO_2 + H_2 \quad \Delta H_{298K} = -41.16 \text{kJ/mol} \tag{5.12}$$
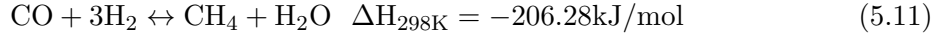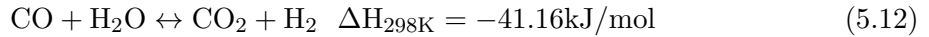
The rate equations of the above reactions are based on the kinetic model proposed by Kopyscinski et al. [21] and described by the following expressions:

$$r_1 = \frac{k_1 K_C p_{CO}^{0.5} p_{H_2}^{0.5}}{(1 + K_C p_{CO}^{0.5} + K_{OH} p_{H_2O} p_{H_2}^{-0.5})^2} \tag{5.13}$$

$$r_2 = \frac{k_2 \left[K_\alpha p_{CO} p_{H_2O} - \left(p_{CO_2} p_{H_2} / K_{eq} \right) \right]}{p_{H_2}^{0.5} (1 + K_C p_{CO}^{0.5} + K_{OH} p_{H_2O} p_{H_2}^{-0.5})^2} \tag{5.14}$$

The values of the kinetic parameters in Eqs.(5.13) and (5.14) follow those determined by Kopyscinski et al. [21]. The composition of gas mixture is changed with the progress of gas

phase reactions. The local gas density is variable and calculated with the ideal gas law. The local viscosity of gas mixture is determined following Kopyscinski et al. [7]

5.3 Numerical solutions

5.3.1 Solver development

Our own gas-solid solver is developed based on the original solver `twoPhaseEulerFoam` in the open source CFD package OpenFOAM [22]. The conservative forms of phase momentum equations are employed as suggested by Passalacqua and Fox [23]. Instead of the semi-implicit method used in `twoPhaseEulerFoam`, the partial elimination algorithm developed by Spalding [24] is implemented to deal with the interphase momentum transfer terms. To prevent solid volume fraction from exceeding its maximum physical value, the effect of solid pressure is implicitly included into the solid-phase continuity equation.
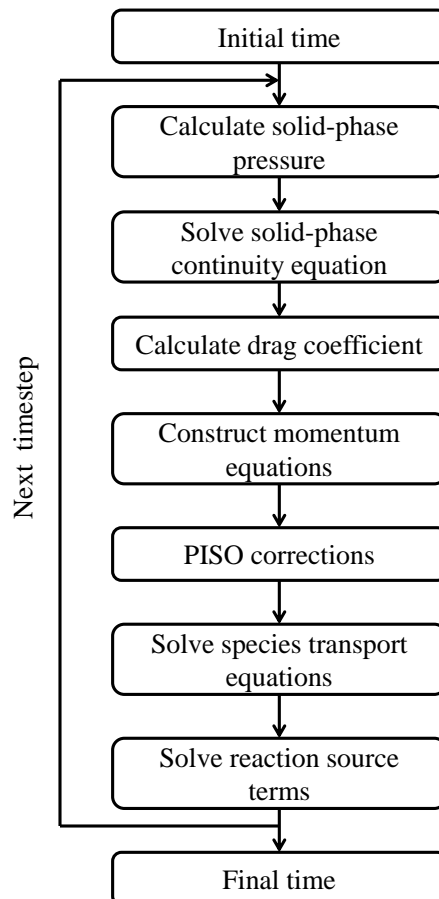
Figure 5.1: Solution algorithm used in the gas-solid two-fluid solver

100

The PISO (Pressure Implicit with Split Operator) solution procedure [25] is adopted to handle pressure-velocity coupling, where a pressure equation is constructed based on the volumetric continuity equation and is solved to correct the predicted velocities. The full coupling of hydrodynamics and chemical reactions is achieved using the time-splitting scheme. In the first fractional time step, the gas species transport equations are constructed and solved spatially without the reaction source terms. In the second fractional time step, the ordinary differential equations representing the reaction source terms are calculated in each cell using the fourth-order Runge-Kutta method. After solving the kinetic reactions, the species mass fractions and other physical properties are updated. The sequences of the iteration operations performed at each time step are illustrated in Figure 5.1.

5.3.2 Simulation setup

The lab-scale fluidized bed setup built by Kopyscinski et al. [7] is simulated as the base case (Figure 5.2). Experimental data of species concentrations are employed for model validation. 0.1 kg of Ni/γ-Al$_2$O$_3$ catalyst as the Geldart B particles was used in this experiment. The gases H$_2$, CO, and N$_2$ are fed into a 0.052 m i.d. fluidized bed reactor and distributed with a nonreactive porous metal plate. The pressure in the bed was 1.3×10^5 Pa. The inlet feed gas mixture consisted of 60 vol.% H$_2$, 20 vol.% CO, and 20 vol.% N$_2$ with a total volumetric flow rate of 10 L$_N$/min.
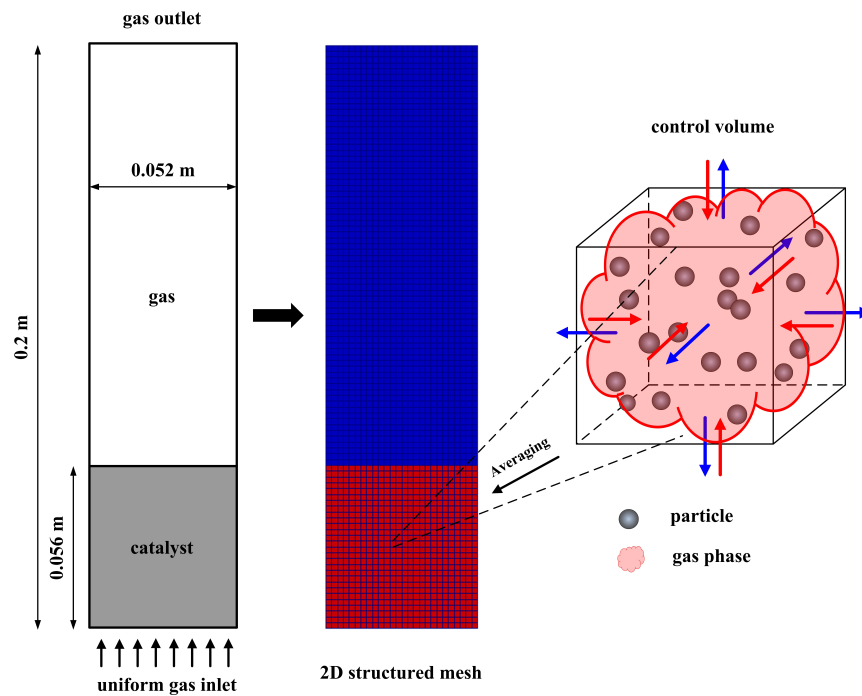
Figure 5.2: Schematic of the fluidized bed reactor and the computational mesh

Table 5.3: Parameters for the simulation of the fluidized-bed base case

Parameter	Value
Bed diameter, m	0.052
Bed height, m	0.20
Initial bed height, m	0.056
Initial solid packing	0.6
Superficial gas velocity, m/s	0.13
Gas density, kg/m^3	ideal gas law
Particle diameter, m	1×10^{-4}
Particle density, kg/m^3	2000
Restitution coefficient	0.7
Y_{CO}	0.45
Y_{H2}	0.10
Y_{N2}	0.45
$F\mathrm{r}$, kg/(m s^2)	0.05
n	2
p	5
ϕ_{f}, deg	28.5
$\alpha_{s,\mathrm{max}}$	0.65
$\alpha_{s,\mathrm{min}}$	0.55

Table 5.4: Discretization schemes for the terms in the governing equations

Term	Discretization scheme
$\partial\psi/\partial t$	`Euler`
$\nabla\psi$	`cellMDLimited Gauss linear 1`
∇p	`Gauss linear`
$\nabla\cdot(\alpha_g\mathbf{U}_g\mathbf{U}_g)$	`Gauss limitedLinearV 1`
$\nabla\cdot(\alpha_s\mathbf{U}_s\mathbf{U}_s)$	`Gauss limitedLinearV 1`
$\nabla\cdot(\alpha_s\mathbf{U}_s)$	`Gauss limitedLinear01 1`
$\nabla\cdot(\alpha_g\mathbf{U}_g Y_{g,i})$	`Gauss limitedLinear01 1`
$\nabla\cdot(\alpha_s\mathbf{U}_s\Theta)$	`Gauss limitedLinear 1`
$\nabla\cdot\tau_k$	`Gauss linear`
$\nabla^2\psi$	`Gauss linear uncorrected`
$\nabla^\perp\psi$	`uncorrected`
$(\psi)_f$	`linear`

Numerical simulations are performed using 2D and 3D meshes with the same dimension as the experimental setup in Figure 5.2. The simulation parameters of the base case are given in Table 5.3. Numerical schemes for all terms in the governing equations are listed in Table 5.4. The first-order Euler implicit scheme is employed to discretize the transient terms. The Gauss linear scheme is used for the pressure gradient, whereas the cellMDLimited Gauss linear scheme with good stability is recommended for other gradients. OpenFOAM provides a limited second-order central differencing scheme (limitedLinear) for the convection terms. When discretizing the velocity convection terms, OpenFOAM adopts the limitedLinearV scheme to maximize the limiting. To bound solid volume fraction and species mass fraction between 0 and 1, the limitedLinear01 scheme is chosen for the convection terms of solid volume fraction and species mass fraction. This special 01-scheme uses the upwind differencing scheme when the variable is not between 0 and 1.

The discretized pressure equation is solved with the geometric algebraic multi-grid (GAMG) method. The bi-conjugate gradient solver with the diagonal incomplete-LU preconditioner is used for solving other equations. Tolerances are set to 1.0×10^{-10} for the pressure, and to 1.0×10^{-5} for other variables. To achieve converged solutions, four PISO corrector steps are performed to make the residual of the solution of the pressure equation below 1.0×10^{-9}.

At the reactor outlet, a fixed pressure of 1.3×10^5 Pa is given to both gas and solid phases. At the solid walls, the no-slip boundary condition is applied to the gas phase, and the partial-slip boundary condition is used for the solid phase [18]. To obtain the time-averaged data, 20 s of operation is simulated during which the results of the last 15 s are adopted for time-averaging. The adaptive time-step is used to guarantee good numerical stability.

5.4   Results and discussion

5.4.1   Grid resolution and drag model study

To study the effect of mesh resolution on the simulation results, three 2D meshes are employed: 1 mm, 2 mm and 4 mm rectangular cells. In Figure 5.3a, due to the considerable numerical diffusion, the largest bed height is predicted with the 4 mm mesh size. By refining the mesh, the low bed heights are given by the 1 mm and 2 mm meshes. Although the numerical diffusion is significantly reduced with the mesh refinement, it is not eliminated and the minor differences in the profiles of solid volume fraction are still observed for the 1 mm and 2 mm meshes. Figure 5.3b shows the simulated CH_4 concentrations with the three meshes. Due to numerical diffusion, the small differences are also found for the three meshes. Different from the solid volume fraction, the CH_4 concentrations predicted with the 4 mm mesh are close to those predicted with 2 mm mesh. The strong gas convective flows in the reactor would reduce the differences in the CH_4 concentration between these two meshes. Since the computational demand significantly increases with the mesh refinement, the 2 mm mesh size has to be used for the reasonable computational effort.

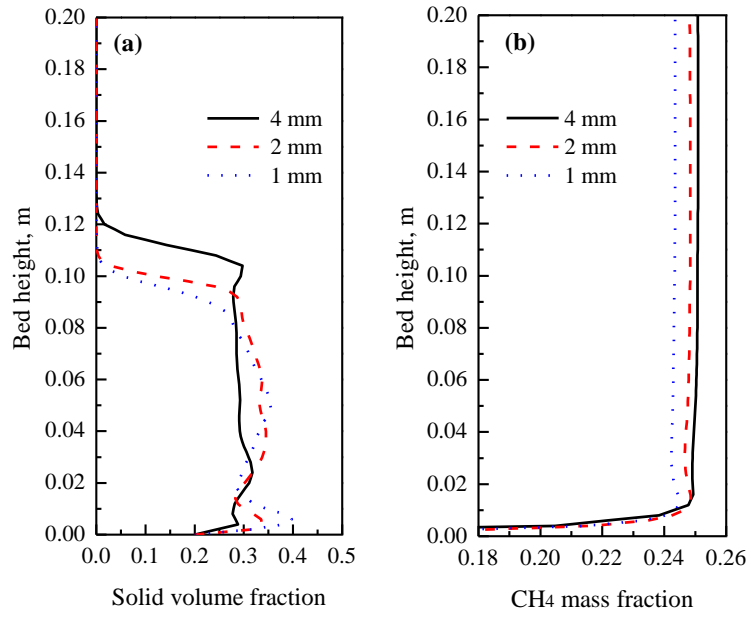**Figure 5.3:** The effect of mesh size on the simulated solid volume fraction and CH_4 mass fraction
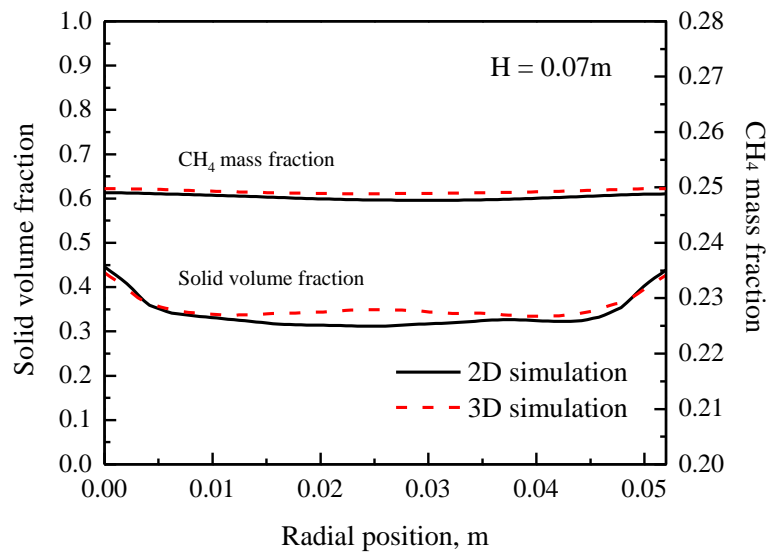

Figure 5.4: The radial profiles of the time-averaged solid volume fraction and CH_4 mass fraction calculated with 2D and 3D computational domains

Generally, all physical gas-solid flows are 3D in nature and the 3D computational domain should be used. However, the 3D simulations are computationally very demanding. Therefore, most of the previous simulations were conducted with 2D computational domains. Cammarata et al. [26] performed the 2D and 3D simulations of bubbling fluidized beds. They found the 2D simulations predicted smaller bubbles than those predicted with the 3D simulations. Xie et al. [27] studied the effects of 2D and 3D domains on the simulated results in bubbling fluidized beds. They concluded that the 2D domain can be used to successfully simulate the bubbling regime. From the above work, great care should be taken when using the 2D computational mesh. In Figure 5.4, the comparison of the 2D and 3D simulations is performed. Similar to the 2D mesh with 2 mm cell, the 3D mesh has 2 mm cell size in the axial direction. The minor differences are found in the solid volume fraction and CH_4 concentrations. According to the Ergun equation [13], the minimum fluidization velocity U_{mf} is calculated as 0.033 m/s. The fluidization velocity of 0.13 m/s ($\sim 4.0U_{mf}$) generates the bubbling fluidization regime. The minor differences between 2D and 3D simulations are consistent with the findings of Xie et al. [27]. Therefore, the 2D computational domain is employed for less computational resources.

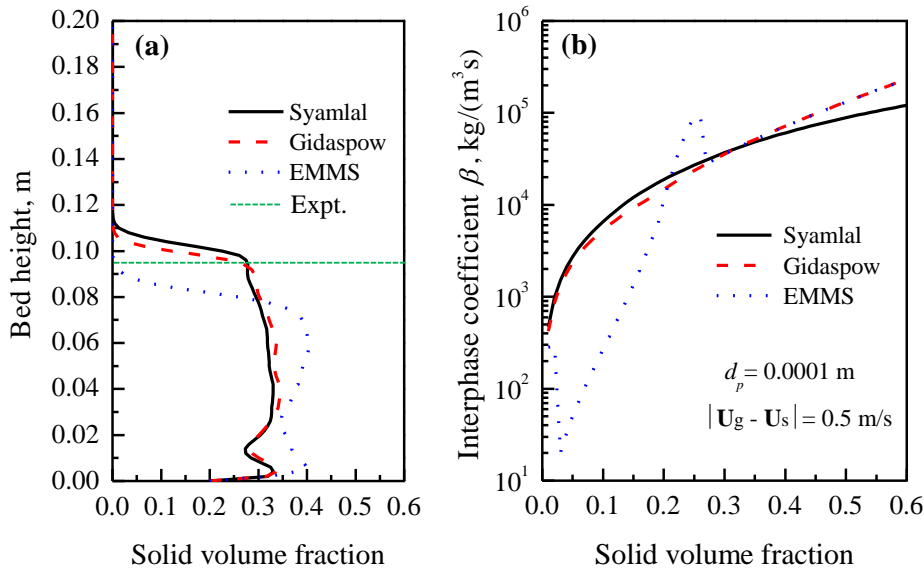**Figure 5.5:** The calculated solid volume fraction and interphase momentum transfer coefficient with three drag force models

In a fluidized bed reactor, the drag force is usually the dominant interaction between gas and solid phases. The simulated axial profiles of solid volume fraction with three drag force models are shown in Figure 5.5a. Clearly, the prediction of bed expansion strongly depends on the

drag force models. The bed expansion is underestimated by the EMMS model and the higher beds are predicted by the Syamlal and Gidaspow models. From the experimental observation, the fluidized bed ended at a height of 0.095 m [7]. The degree of bed expansion is reasonably captured by the Syamlal and Gidaspow models. Figure 5.5b shows the calculations of the interphase momentum transfer coefficient for three models. It is seen that the EMMS model gives much smaller values of β in the dilute particle flows with the solid volume fraction below 0.2. The smaller value of β represents the weaker interaction and results in the lower bed expansion. The EMMS model is developed based on the concept of particle clusters. The particle cluster has a larger particle diameter and a smaller interphase exchange coefficient. As suggested by Yang et al. [15], the EMMS model needs to be further improved for other systems. In this work, the Gidaspow model is chosen for the subsequent simulations.

5.4.2 Reacting flow fields and model validation

The efficiency of a fluidized bed reactor mainly depends on the gas-solid mixing. The large volumetric interfacial areas are preferred since the catalytic methanation reaction takes place in the emulsion phase. Figure 5.6 demonstrates the instantaneous gas-solid flow patterns at the superficial gas velocity of 0.13 m/s. It is found that the solid particle flows are quite chaotic with non-uniform distributions and there exist no large gas bubbles formed in the bed. Herein, the excellent gas-solid mixing is achieved under such operating conditions, which allows for achieving the homogeneous temperature fields without hot spots in the bed.
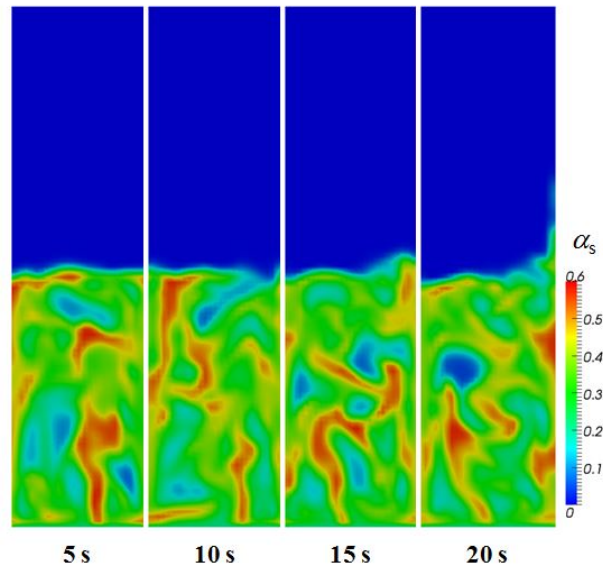
Figure 5.6: Snapshots of the solid volume fraction distributions at the superficial gas velocity of 0.13 m/s
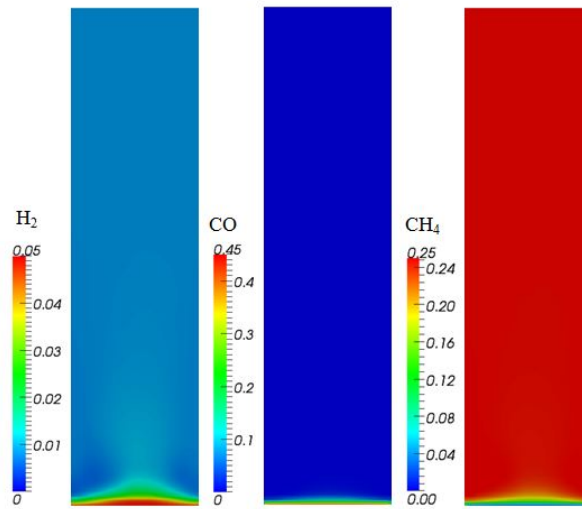
Figure 5.7: The time-averaged distributions of the mass fractions of H_2, CO and CH_4

The time-averaged fields of H_2, CO and CH_4 concentrations are presented in Figure 5.7. The local information of the hydrodynamics and species concentrations in the reactor is provided by the CFD simulations. H_2 is consumed rapidly in the region near the inlet because of the large reactant concentrations and catalyst content here. In the upper region of the bed, H_2 is not completely reacted and the low concentration of the residual H_2 is observed. However, the CO concentration in the upper region is almost zero, which implies CO has been completely converted in the fluidized bed. The high CH_4 concentration is uniformly distributed in the bed.
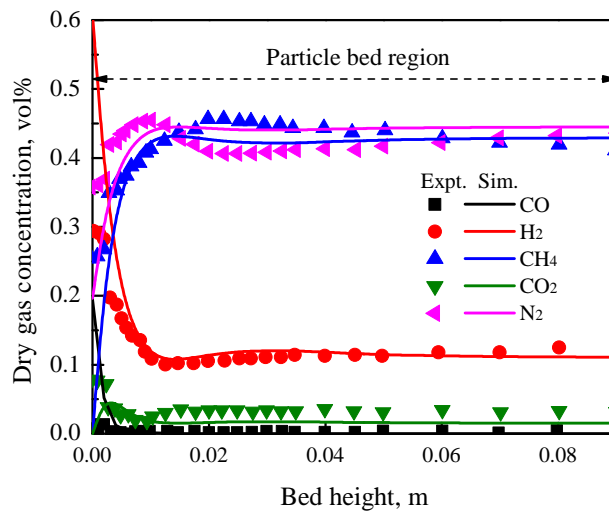
Figure 5.8: Comparison of the simulated species concentrations with the experimental data in the literature

To validate the gas-solid hydrodynamic and methanation reaction models used in current research, the simulated mole fractions of gas species are compared with the literature data (Figure 5.8). The simulated results are in good agreement with the experimental values measured at the end of the bed. However, the large discrepancy is observed in the region near the gas distributor. In accordance with Figure 5.7, the methanation reaction mainly takes place in the region near the gas distributor. The deviation in this region may be due to the uniform distribution of gas feed in the simulations. The key role of the fluidization quality near the gas distributor suggests using the real gas distributor configuration in the further work. Meanwhile, the validity of the global reaction kinetics should be further confirmed in such complex fluidized bed flows.

5.4.3 The effects of different operating parameters

The macroscopic functionality of a fluidized bed reactor is directly determined by various operating conditions. It is of utmost importance to recognize the optimal operating conditions for satisfactory syngas conversion and product yield. The effect of different gas inlet velocities on the bed expansion ratio is shown in Figure 5.9. For the reactive flow simulations, a consistent increase in the bed expansion ratio is observed with the increase in the gas inlet velocity. As a comparison, the cold model simulations are also performed without considering the reactions in the bed. The higher bed expansions are predicted by the cold flow models, especially at the high gas inlet velocities. The significant distinction could be due to the CO methanation reaction. This reaction results in the large reduction of the gas volume and the bed expansion is greatly suppressed by this defluidization behavior. At the high gas inlet velocities, the gas-volume reduction makes the difference in the bed expansion more pronounced. In essence, the density and viscosity of reacting gas mixture are locally variable and then the different interphase force interactions generate the different bed expansion behaviors.
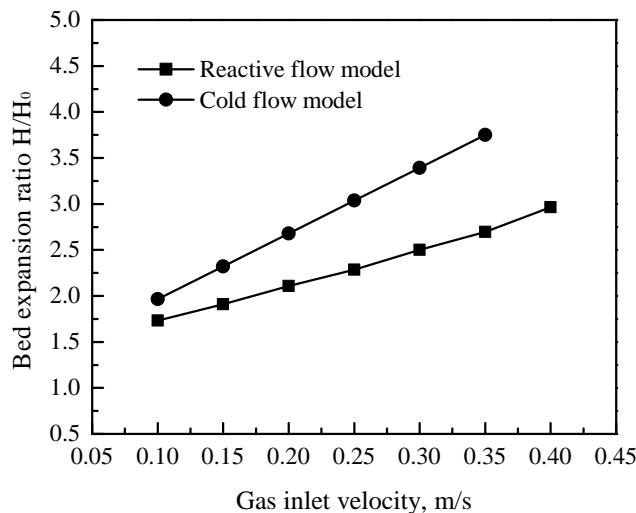
Figure 5.9: The effect of gas inlet velocity on the bed expansion in the reactor
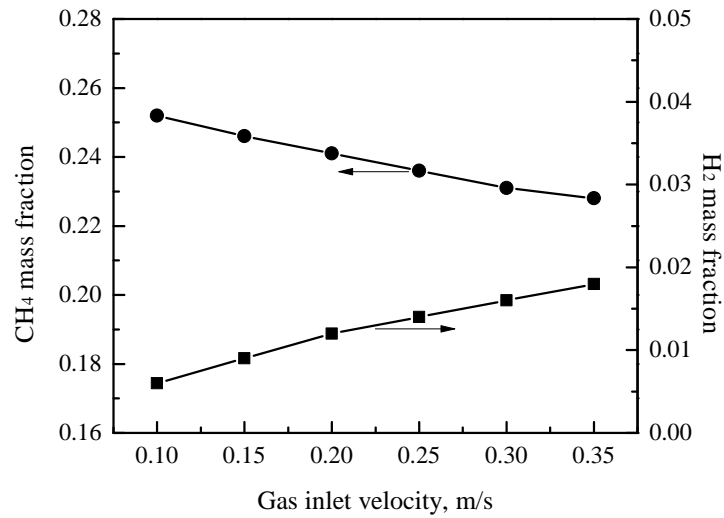
Figure 5.10: The effect of gas inlet velocity on the mass fractions of CH_4 and H_2
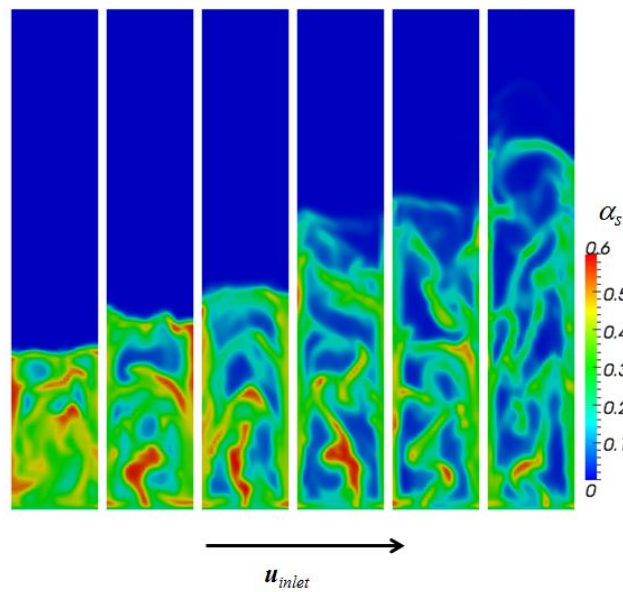
Figure 5.11: Snapshots of solid volume fraction for different gas inlet velocities

Figure 5.10 reveals the effect of gas inlet velocity on the CH_4 and H_2 concentrations at the reactor outlet. It is indicated that the CH_4 concentration decreases with the increase in gas inlet velocity, while the increase in the residual H_2 concentration is found. The instantaneous distributions of the solid volume fraction are predicted by the reactive flow models for different gas inlet velocities. In Figure 5.11, the higher gas input rate makes the catalyst concentration more dilute. Many large bubbles are formed at the high gas inlet velocities. In such cases, the volumetric interfacial areas are significantly reduced. Moreover, the larger gas velocity

shortens the residence time of the reactant gases in the bed. Hence, the high gas inlet velocity is not beneficial to the syngas conversion with this amount of catalyst inventory. However, from the industrial point of view, the large reactant input is of most interest as it ensures high volumetric productivity. Thereby, the catalyst inventory should be adjusted accordingly when increasing the syngas feedstock.
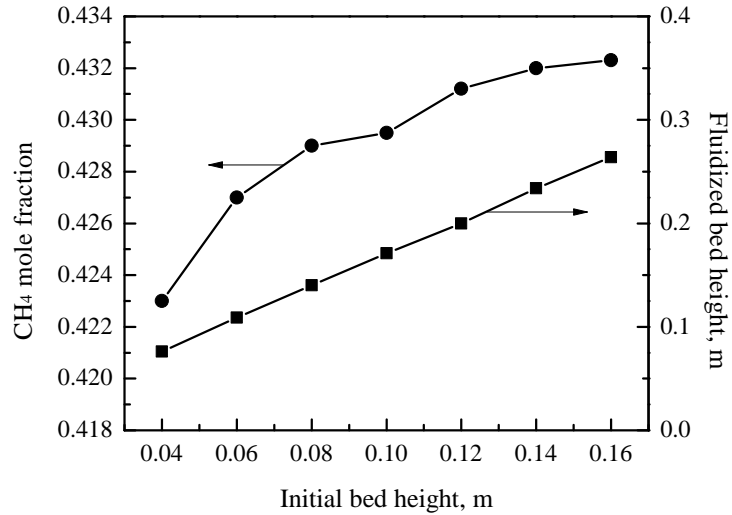
Figure 5.12: The effect of catalyst inventory on the CH_4 concentration and bed height
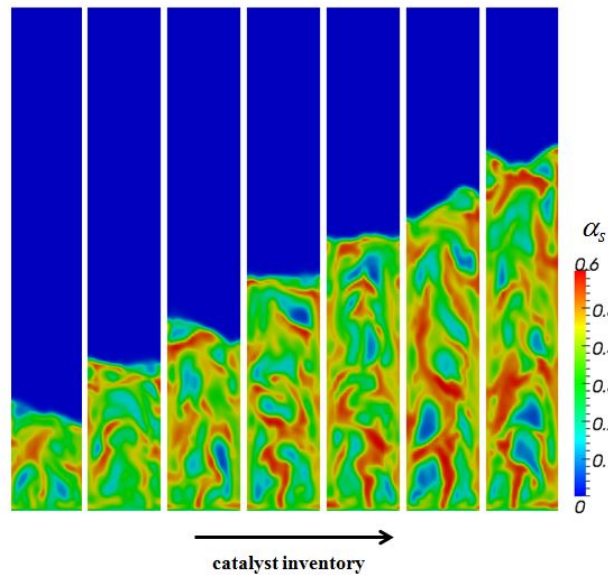
Figure 5.13: Snapshots of solid volume fraction for different catalyst inventories

Figure 5.12 displays the effect of catalyst inventory on the CH_4 mole fraction and bed height. The catalyst inventory is represented by the initial bed height. One observes that the bed height continuously increases when the initial bed height is increased. The CH_4

concentration also increases with the catalyst inventory. However, the increase is quite minor for the large catalyst inventories. This is well reflected by the catalyst particle concentrations as shown in Figure 5.13. The catalyst concentrations are similar for the different catalyst inventories. Meanwhile, when increasing the catalyst inventory, the higher bed leads to the longer residence time of the reactant gases. Due to the fixed feedstock, further increase in the catalyst inventory cannot significantly improve the product concentration. These findings indicate that there exist some optimal conditions where the large product yield could be obtained with reasonable catalyst amount.

In the industrial situations, the H_2/CO ratio is usually very low (0.3 - 2.0) in the syngas produced from biomass and coal gasifiers. To achieve good CO conversion, the water-gas shift reaction plays an important role in adjusting the H_2/CO ratio by converting the excess CO with H_2O into CO_2 and H_2. Figure 5.14 presents the effect of the water addition in feed gases on the axial profiles of the CH_4 and H_2 concentrations. It is found that the decrease in the H_2/CO ratio in the feed gases yields the smaller concentrations of CH_4 and H_2. By adding water into the feed gases, the CH_4 mole fraction is increased by about 38% for the gas feed (30 vol.% H_2, 30 vol.% CO and 20 vol.% H_2O). The water-gas shift reaction provides the additional H_2 used for the methanation reaction. Comparing to CH_4 mole fraction, the increase in the H_2 mole fraction is much higher. As an example, for the gas feed with 30 vol.% H_2 and 30 vol.% CO, H_2 is almost completely consumed, whereas a large amount of CO is not reacted. For the gas feed with 30 vol.% H_2, 30 vol.% CO and 20 vol.% H_2O, the residual CO reacts with H_2O in the feed to produce much H_2.
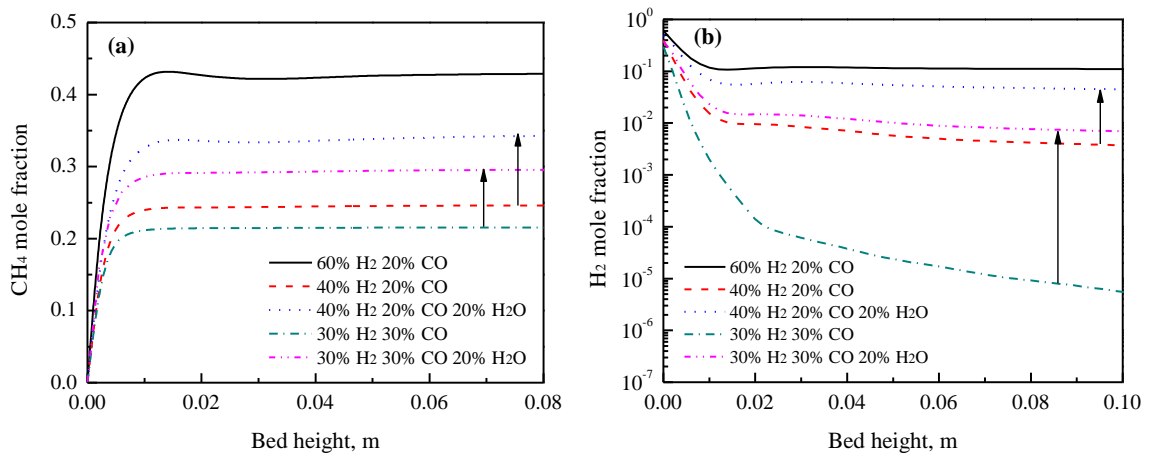
Figure 5.14: The effect of the feed composition on the CH_4 and H_2 concentrations

5.5   Conclusions

The implementation of gas-solid methanation reacting flow models is achieved within Open-FOAM. A methanation kinetic model with two global reactions is coupled with the Eulerian-Eulerian two-fluid model. To achieve a compromise between computational effort and solution accuracy, the simulations are performed with the 2D mesh with 2 mm cell size. The Gidaspow model reasonably predicts the bed height of 0.095 m. The simulated axial concentrations of CO, H_2, CH_4, CO_2 and N_2 agree well with the measured data at the end of the bed. The modeling framework provides a new path for studying the fluidized bed methanation reactors.

The bed expansion in the fluidized bed methanation reactor is weakened due to the CO methanation reaction with the gas volume reduction. The increase in the gas inlet velocity results in the smaller catalyst concentration and shorter reactant residence time. At the reactor outlet the H_2 concentration is increased when increasing the gas inlet velocity, whereas the decrease in the CH_4 concentration is obtained. When increasing the catalyst inventory, the bed height and CH4 concentration are increased. The addition of water into the gas feedstock increases the CH_4 and H_2 concentrations since the additional H_2 used for the methanation reaction can be produced by the water-gas shift reaction. It is important to couple the water-gas shift reaction with the hydrodynamic models for the methanation reactor modeling.

Literature

[1] I. Wender, Reactions of synthesis gas, Fuel Processing Technology 48 (1996) 189–297.

[2] M. Gassner, F. Marechal, Thermo-economic process model for thermochemical production of Synthetic Natural Gas (SNG) from lignocellulosic biomass, Biomass and Bioenergy 33 (2009) 1587–1604.

[3] J. Kopyscinski, T. J. Schildhauer, S. M. A. Biollaz, Production of synthetic natural gas (SNG) from coal and dry biomass - a technology review from 1950 to 2009, Fuel 89 (2010) 1763–1783.

[4] Cobb, R. C. Streeter, Evaluation of fluidized-bed methanation catalysts and reactor modeling, Industrial & Engineering Chemistry Process Design and Development 18 (1979) 672–679.

[5] A. Bellagi, H. Hammer, Mathematische Modellierung eines Wirbelschichtreaktors für die Methanisierung von Kohlenmonoxid, Chemie Ingenieur Technik 56 (1984) 60–62.

[6] T. Kai, S. Furusaki, Effect of volume change on conversions in fluidized catalyst beds, Chemical Engineering Science 39 (1984) 1317–1319.

[7] J. Kopyscinski, T. J. Schildhauer, S. M. A. Biollaz, Fluidized-bed methanation: Interaction between kinetics and mass transfer, Industrial & Engineering Chemistry Research 50 (2011) 2781–2790.

[8] J. Kopyscinski, T. J. Schildhauer, S. M. A. Biollaz, Methanation in a fluidized bed reactor with high initial CO partial pressure: Part II - Modeling and sensitivity study, Chemical Engineering Science 66 (2011) 1612–1621.

[9] C. N. Wu, D. Y. Tian, Y. Cheng, CFD-DEM simulation of syngas-to-methane process in a fluidized-bed reactor. In: 13th International Conference on Fluidization - New Paradigm in Fluidization Engineering, Gyeong-ju, Korea, 2010.

[10] Y. L. Zhang, Y. F. Zhao, M. Ye, R. Xiao, Z. M. Liu, A DEM study of the reduction of volumetric flow in bubbling fluidized bed methanation reactors. In: 14th International Conference on Fluidization - From Fundamentals to Products, Noordwijkerhout, The Netherlands, 2013.

[11] D. Gidaspow, Multiphase flow and fluidization: Continuum and kinetic theory descriptions; Academic Press: Boston, 1994.

[12] M. Syamlal, W. Rogers, T. J. OBrien, MFIX Documentation: Theory Guide; Technical Note DOE/METC-94/1004; Department of Energy (DOE), Morgantown Energy Technology Center: Morgantown, WV, USA, 1993.

[13] S. Ergun, Fluid flow through packed columns, Chemical Engineering Progress 48 (1952) 89–95.

[14] C. Y. Wen, Y. H. Yu, Mechanics of fluidization, Chemical Engineering Progress Symposium Series 62 (1966) 100–111.

[15] N. Yang, W. Wang, W. Ge, L. N. Wang, J. H. Li, Simulation of heterogeneous structure in a circulating fluidized-bed riser by combining the two-fluid model with the EMMS approach, Industrial & Engineering Chemistry Research 43 (2004) 5548–5561.

[16] J. T. Jenkins, S. B. Savage, A theory of the rapid flow of identical, smooth, nearly elastic spherical particles, Journal of Fluid Mechanics 130 (1983) 187–202.

[17] C. K. K. Lun, S. B. Savage, D. J. Jeffrey, N. Chepurniy, Kinetic theories for granular flow: inelastic particles in Couette flow and slightly inelastic particles in a general flowfield, Journal of Fluid Mechanics 140 (1984) 223–256.

[18] P. C. Johnson, R. Jackson, Frictional-collisional constitutive relations for granular materials, with application to plane shearing, Journal of Fluid Mechanics 176 (1987) 67–93.

[19] A. Srivastava, S. Sundaresan, Analysis of a frictional-kinetic model for gas-particle flow, Powder Technology 129 (2003) 72–85.

[20] P. C. Johnson, P. Nott, R. Jackson, Frictional-collisional equations of motion for particulate flows and their application to chutes, Journal of Fluid Mechanics 210 (1990) 501–535.

[21] J. Kopyscinski, T. J. Schildhauer, F. Vogel, S. M. A. Biollaz, A. Wokaun, Applying spatially resolved concentration and temperature measurements in a catalytic plate reactor for the kinetic study of CO methanation, Journal of Catalysis 271 (2010) 262–279.

[22] OpenCFD Ltd., OpenFOAM 2.1.1 User's Guide, UK (2012).

[23] A. Passalacqua, R. O. Fox, Implementation of an iterative solution procedure for multi-fluid gas-particle flow models on unstructured grids, Powder Technology 213 (2011) 174–187.

[24] D. B. Spalding, Numerical computation of multi-phase fluid flow and heat transfer. In: C. Taylor Ed., Recent Advances in Numerical Methods in Fluids, Pineridge Press, 1980.

[25] R. Issa, Solution of the implicitly discretized fluid flow equations by operator-splitting, Journal of Computational Physics 62 (1985) 40–65.

[26] L. Cammarata, P. Lettieri, G. D. Micale, D. Colman, 2D and 3D simulations of bubbling fluidized beds using Eulerian-Eulerian models, International Journal of Chemical Reactor Engineering 1 (2003) 1–15.

[27] N. Xie, F. Battaglia, S. Pannala, Effects of using two- versus three-dimensional computational modeling of fluidized beds: Part I, Hydrodynamics, Powder Technology 182 (2008) 1–13.

Chapter 6

Study on CFD-PBM turbulence closures based on k-ε and Reynolds stress models for heterogeneous bubble column Flows

Abstract

Gas-liquid heterogeneous flows in two cylindrical bubble columns are simulated using the computational fluid dynamics - population balance model (CFD-PBM) implemented in the open source CFD package OpenFOAM. The liquid phase turbulence is described by the k-ε model and the Reynolds stress model (RSM). Simulation results are compared with experimental data from the literature. For the bubble column operated at 0.10 m/s, minor difference is found in the predicted profiles when using 10 and 20 bubble classes. With the Rampure drag coefficient, Tomiyama lift coefficient and bubble-induced turbulence (BIT), the gas holdup is well predicted by both k-ε model and RSM. For the bubble column operated at 0.12 m/s, good agreement with experimental data is obtained when the k-ε BIT model works with the Tsuchiya drag coefficient and Tomiyama lift coefficient. The RSM with BIT also gives reasonable prediction when using the combination of Tsuchiya drag coefficient and Tomiyama lift coefficient.

6.1 Introduction

Bubble columns are of considerable industrial importance due to their wide applications in the chemical, biochemical and petrochemical industries. Numerous advantages of the bubble column reactors are recognized such as excellent heat/mass transfer characteristics, simple construction, no moving parts and low operating cost [1]. Most of the bubble columns are operated under turbulent flow conditions. Turbulent fluid dynamics is physically related to gas dispersion, bubble breakup/coalescence and interphase transfer phenomena. The deep knowledge of flow turbulence in bubble columns is crucial to successful reactor design and scale-up.

In recent years computational fluid dynamics (CFD) has emerged as an important tool to resolve the multiphase physics in bubbly turbulent flows. The multiphase turbulence could be described by the fully-resolved direct numerical simulation (DNS) methods [2]. Due to massive computational demand, the application of DNS-based methods is only restricted to very few bubbles in gas-liquid systems. The Euler-Lagrange method also has limited applications in simulating the gas-liquid flows. Alternatively, the Euler-Euler two-fluid model is widely employed to simulate the gas-liquid turbulent flows with high gas fractions. As a result of the averaging procedure, the Reynolds stress terms in the two-fluid model should be closed by the appropriate turbulence model. The gas-liquid two-fluid modeling approach still remains some open questions due to the uncertainty regarding the phase interaction terms, turbulence closure schemes, and multiple bubble sizes [3].

Most of the two-fluid simulations were carried out using single mean bubble size in bubble columns [4–7]. This assumption is usually reasonable in the homogeneous flow regime. However, in the highly turbulent heterogeneous flows, the knowledge of local bubble size distribution is very essential since a wide spectrum of bubble size is formed due to bubble breakup and coalescence. Many attempts have been made by coupling computational fluid dynamics with population balance model (CFD-PBM) to simulate the gas-liquid flows [8–12]. In the CFD-PBM method the turbulence closure scheme not only determines the Reynolds stress terms but also governs the solution of the population balance equations. Thus, it is of prime importance to examine the turbulence models used in the CFD-PBM method.

The two equation k-ε turbulence models are widely applied in simulating bubbly turbulent flows [13–18]. The k-ε models have mathematical simplicity and need low computational demand. However, they have the shortcoming from the isotropic eddy-viscosity assumption. In order to handle the anisotropic turbulent flows, the Reynolds stress model (RSM) can be coupled with the Euler-Euler multiphase algorithm [19]. The directional effect of the Reynolds stress field is represented with the transport equation of each Reynolds stress component. The Euler-Euler large eddy simulation (LES) method is often employed to track more turbulence details in the gas-liquid flows [20–22]. Comparing with the RSM, the two-phase LES method requires much larger computational effort because the finer grids should be used for resolving

116

the large eddy structures. As a result, this LES form of turbulence model has not been widely applied for simulating large-scale flow reactors.

The two equation k-ε turbulence models are widely applied in simulating bubbly turbulent flows [13–18]. The k-ε models have mathematical simplicity and need low computational demand. However, they have the shortcoming from the isotropic eddy-viscosity assumption. In order to handle the anisotropic turbulent flows, the Reynolds stress model (RSM) can be coupled with the Euler-Euler multiphase algorithm [19]. The directional effect of the Reynolds stress field is represented with the transport equation of each Reynolds stress component. The Euler-Euler large eddy simulation (LES) method is often employed to track more turbulence details in the gas-liquid flows [20–22]. Compared to the RSM, the two-phase LES method requires much larger computational effort because the finer grids should be used for resolving the large eddy structures. This form of turbulence model has not been widely applied by industrial users.

Comparative studies of turbulence models were performed for bubble column flows by various researchers. Zhang et al. [4] compared the different model constants of the sub-grid scale LES model, and three bubble-induced k-ε models were also investigated. Tabib et al. [6] studied three different turbulence models (standard k-ε, RSM and LES) used for the liquid phase. Ekambara and Dhotre [7] assessed the performance and applicability of the standard k-ε, RNG k-ε, k-ω, RSM and LES models. Laborde-Boutet et al. [23] investigated three formulations of the k-ε model (standard, RNG, realizable) combined with three different modalities to account for gas-phase effects. However, the bubble size distribution was not considered in the above work. The roles of different turbulence models in the CFD-PBM method are still not clarified, especially for the heterogeneous flow regime in the bubble columns. Furthermore, the combined effects of interfacial force models and bubble-induced turbulence models should be further investigated.

Most of previous bubble column simulations were conducted with different CFD codes and the test cases were also of great difference. As a result, the distinct choices of solution algorithms, discretization schemes and grid arrangements make it difficult to clarify the intrinsic difference among various turbulence models. Jakobsen et al. [24] suggested a solution to this issue through a unified code available for all research groups. Nowadays the open source CFD package OpenFOAM (Open Field Operation And Manipulation) gains some success in the bubble column simulations [10, 18, 25]. The OpenFOAM package offers the possibility to have insight into the source codes and hence it is of great convenience to implement new physical models.

The previous simulations were conducted with different commercial CFD codes and the test cases were also of great difference. As a result, the distinct choices of solution algorithms, discretization schemes and grid arrangements make it difficult to clarify the intrinsic difference

among various turbulence models. Jakobsen et al. [24] suggested a solution to this issue through a unified code available for all research groups. Nowadays the open source CFD package OpenFOAM (Open Field Operation And Manipulation) gains some success in the bubble column simulations [10, 18, 25]. The OpenFOAM package offers the possibility to have insight into the source codes and hence it is of great convenience to implement new physical models.

In this work the population balance equation (PBE) is implemented into OpenFOAM and coupled with a two-fluid model solver. The k-ε model and Reynolds stress model with bubble-induced turbulence models are also implemented to account for the liquid phase turbulence. Two bubble columns operated at high gas inlet velocities are simulated. Numerical results are obtained for gas holdup, axial liquid velocity, bubble mean diameter and turbulence fields. Simulations of the k-ε and Reynolds stress models are compared with the experimental data in the literature.

6.2   Two-fluid model equations

Numerical simulations are performed with the Euler-Euler two-fluid model. For the bubble population balance, the bubble size distribution is divided into a number of bubble classes. All the bubbles are assumed to travel at the same velocity $\mathbf{U}_g$. This simplification has been employed with success by some researchers [9, 10, 12]. Theoretically, the multi-fluid model is more accurate and it allows different bubble classes to move at different velocities. However, the momentum equation for each bubble class should be solved. Since the multi-fluid model is computationally expensive, the two-fluid model is used in this work. The continuity and momentum equations of the gas and liquid phases are written as

$$\frac{\partial(\alpha_k \rho_k)}{\partial t} + \nabla \cdot (\alpha_k \rho_k \mathbf{U}_k) = 0 \tag{6.1}$$

$$\frac{\partial(\alpha_k \rho_k \mathbf{U}_k)}{\partial t} + \nabla \cdot (\alpha_k \rho_k \mathbf{U}_k \mathbf{U}_k) = -\alpha_k \nabla p + \nabla \cdot (\alpha_k \tau_k) + \alpha_k \rho_k \mathbf{g} + \mathbf{M}_k \tag{6.2}$$

where k refers to the phase (l for liquid and g for gas), $\mathbf{U}$ represents the phase velocity, α denotes the volume fraction of each phase and τ is the effective stress tensor. $\mathbf{M}_k$ is the interfacial momentum transfer term due to various interphase forces.

In this study the drag and lift forces are considered, while the other forces are neglected since they have little effect on the flows [4]. The drag force resists the bubble motion in the surrounding liquid. The interfacial transfer term due to the drag force is defined as

$$\mathbf{M}_{D,g} = -\mathbf{M}_{D,l} = \frac{3}{4} \alpha_l \alpha_g \rho_l \frac{C_D}{d_B} |\mathbf{U}_g - \mathbf{U}_l| (\mathbf{U}_l - \mathbf{U}_g) \tag{6.3}$$

where d_B is the bubble size and C_D is the drag coefficient which depends on the flow regime and the liquid property. The drag coefficient for the single bubble proposed by Tsuchiya et al. [26] is used in this work:

$$C_{D,\infty} = \max\left[\frac{24}{\text{Re}}(1 + 0.15\text{Re}^{0.687}), \frac{8}{3}\frac{\text{Eo}}{\text{Eo} + 4}\right] \tag{6.4}$$

where the bubble Reynolds number Re_B and Eötvös number Eo are defined as

$$\text{Re} = \frac{\rho_l d_B |\mathbf{U}_g - \mathbf{U}_l|}{\mu_l}, \quad \text{Eo} = \frac{g(\rho_l - \rho_g)d_B^2}{\sigma}$$

In the heterogeneous flow, the bubble swarms are formed and they experience different drag forces from the single bubble. The drag coefficient for bubble swarm is also used following the work of Rampure et al. [27] by correcting the drag coefficient of the single bubble as

$$C_D = (1 - \alpha_g)^2 C_{D,\infty} \tag{6.5}$$

In addition to the drag force, the bubble experiences a lift force perpendicular to its relative motion. The lift force plays an important role in the radial gas holdup distribution. The momentum transfer due to the lift force is calculated as

$$\mathbf{M}_{L,g} = -\mathbf{M}_{L,l} = \alpha_g \rho_l C_L (\mathbf{U}_l - \mathbf{U}_g) \times (\nabla \times \mathbf{U}_l) \tag{6.6}$$

where C_L is the lift coefficient. For the single bubble, the lift coefficient varies with bubble size and shape. Small bubbles tend to move towards the wall and large bubbles move towards the centre of the bubble column. Tomiyama [28] proposed a lift coefficient to capture this phenomenon:

$$C_L = \begin{cases} \min\big[0.288\tanh(0.121\text{Re}), f(\text{Eo}_\text{d})\big] & \text{Eo}_\text{d} < 4 \\ f(\text{Eo}_\text{d}) & 4 \leqslant \text{Eo}_\text{d} \leqslant 10.7 \\ -0.29 & 10.7 < \text{Eo}_\text{d} \end{cases} \tag{6.7}$$

with

$$f(\text{Eo}_\text{d}) = 0.00105\text{Eo}_\text{d}^3 - 0.0159\text{Eo}_\text{d}^2 - 0.0204\text{Eo}_\text{d} + 0.474$$

$$\text{Eo}_\text{d} = \frac{g(\rho_l - \rho_g)d_\text{H}^2}{\sigma}, \quad d_\text{H} = d_\text{B}(1 + 0.163\text{Eo}^{0.757})^{1/3}$$

The above lift coefficient is justified for the single bubble, but for bubble swarm the uncertainty still remains. Very few studies are found on the lift force of the bubble swarms. Behzadi et al. [17] proposed a lift coefficient as a function of gas holdup:

$$C_L = 6.51 \times 10^{-4} \alpha_g^{-1.2} \tag{6.8}$$

However, the applicability of this lift coefficient should be further confirmed.

6.3 Population balance model

There are several approaches developed for solving the population balance equations, e.g. the method of classes [29], Monte Carlo method [30], the parallel parent and daughter classes method [31], and the direct quadrature method of moments (DQMOM) [32]. The DQMOM has proved an efficient technique for solving the population balance equation. Selma et al. [33] compared the DQMOM with the class method. Both methods can give good agreement with the experimental data. In this work the class method is used, since the bubble size distribution can be directly defined. The bubble classes are represented through a finite number of pivotal grid x_i, and the coalescence and breakup processes are transformed into the birth and death rates for each bubble class. The population balance equation for the i-th class is written as

$$\frac{\partial}{\partial t}(\alpha_g f_i) + \nabla \cdot (\alpha_g \mathbf{U}_{g,i} f_i) = S_i \tag{6.9}$$

where f_i represents the fraction of bubble group i occupied in the gas holdup, and S_i is the source term accounting for bubble coalescence and breakup:

$$S_i = \sum_{\substack{j,k \\ x_{i-1} \leqslant (x_j + x_k) \leqslant x_{i+1}}}^{j \geqslant k} (1 - \frac{1}{2}\delta_{jk})\eta_{i,jk}c(x_j, x_k)\frac{\alpha_g f_j}{x_j}\frac{\alpha_g f_k}{x_k}x_i$$

$$-\alpha_g f_i \sum_{k=1}^{M} c(x_i, x_k)\frac{\alpha_g f_k}{x_k} + \sum_{k=i}^{M} \gamma_{i,k}b(x_k)\frac{\alpha_g f_k}{x_k}x_i - b(x_i)\alpha_g f_i \tag{6.10}$$

where

$$\eta_{j,ik} = \begin{cases} \dfrac{x_{i+1} - v}{x_{i+1} - x_i} & x_i \leqslant v \leqslant x_{i+1} \\[3mm] \dfrac{v - x_{i+1}}{x_i - x_{i-1}} & x_{i-1} \leqslant v \leqslant x_i \end{cases}$$

$$\gamma_{i,k} = \int_{x_{i-1}}^{x_i} \frac{v - x_{i-1}}{x_i - x_{i-1}}\beta(v, x_k)dv + \int_{x_i}^{x_{i+1}} \frac{x_{i+1} - v}{x_{i+1} - x_i}\beta(v, x_k)dv$$

where $c(x_j, x_k)$ is the coalescence frequency, $b(x_i)$ is the breakup frequency of the bubble group i, and $\beta(v, x_k)$ is the daughter size distribution. the Sauter mean diameter d_{32} is calculated to represent the bubble size d_B:

$$d_{32} = \frac{\sum_i f_i}{\sum_i (f_i/d_i)} \tag{6.11}$$

The coalescence frequency $c(d_i, d_j)$ is usually calculated as the product of the collision frequency $\varpi_c(d_i, d_j)$ and the coalescence efficiency $P_c(d_i, d_j)$:

$$c(d_i, d_j) = \varpi_c(d_i, d_j) P_c(d_i, d_j) \tag{6.12}$$

where d_i and d_j are the diameter of bubble group i and j, respectively. The bubble coalescence may occur due to a variety of mechanisms in turbulent flows, e.g. turbulent fluctuation, global velocity gradient, eddy capture, buoyancy and wake effect [34]. Various coalescence models are proposed in the literature. Since we focus on assessing the performance of the turbulence models, the coalescence mechanism only due to turbulent fluctuation is considered in this work. The uncertainty in other mechanisms would make the problem more complicated. The collision frequency resulting from turbulent fluctuation is expressed as [35]

$$\varpi_c(d_i, d_j) = \frac{\pi}{4}\sqrt{2}\varepsilon_l^{1/3}(d_i + d_j)^2 (d_i^{2/3} + d_j^{2/3})^{1/2} \tag{6.13}$$

Wu et al. [36] and Wang et al. [37] proposed some modified forms of the collision frequency. However, the uncertainty still exists in their expressions. Accordingly, the coalescence efficiency of the bubble group i and j is calculated as [35]:

$$P_c(d_i, d_j) = \exp\left\{ -C\frac{[0.75(1 + \xi_{ij}^2)(1 + \xi_{ij}^3)]^{1/2}}{(\rho_g/\rho_l + C_{\mathrm{vm}})(1 + \xi_{ij})^3}\mathrm{We}_{ij}^{1/2}\right\} \tag{6.14}$$

where C is a model parameter, $C = 1.0$; $\xi_{ij} = d_i/d_j$; C_{vm} is the coefficient of the virtual mass force, $C_{\mathrm{vm}} = 0.5$; We_{ij} is the Weber number.

Many previous models considered the turbulent collision between eddies and bubbles was the dominant reason for bubble breakup. The breakup model by Luo and Svendsen [38] is used in this work. It is based on the concept that the bubble breaks up when it collides with the turbulent eddy with sufficient energy. One advantage is that this model does not include empirical parameters. Another advantage is that the daughter size distribution is derived directly. This model has been widely used in the previous work [8, 10–12]. The breakup frequency of a bubble with volume v_i that breaks into two daughter bubbles with volume v_j and $(v_i - v_j)$ is given as

$$\Omega(v_j, v_i) = 0.923(1 - \alpha_g)\left(\frac{\varepsilon_l}{d_i^2}\right)^{1/3}\int_{\xi_{\min}}^1 \frac{(1 + \xi)^2}{\xi^{11/3}}\exp\left(-\frac{12c_f\sigma}{2\rho_l\varepsilon_l^{2/3}d_i^{5/3}\xi^{11/3}}\right)d\xi \tag{6.15}$$

where $\xi_{\min} = \lambda_{\min}/d_i$, $\lambda_{\min} = (11.4 - 31.4)\eta$, $\eta = (\mu_l/\rho_l)^{0.75}/\varepsilon_l^{0.25}$. c_f is calculated as

$$c_f = \left(\frac{v_j}{v_i}\right)^{2/3} + \left(1 - \frac{v_j}{v_i}\right)^{2/3} - 1 \tag{6.16}$$

The total breakup frequency of bubbles with size v_i is calculated:

$$b(v_i) = \frac{1}{2} \int_0^{v_i} \Omega(v, v_i) dv = \frac{1}{2} \int_0^1 \Omega(v_i f_{\mathrm{v}}, v_i) df_{\mathrm{v}} = \int_0^{0.5} \Omega(v_i f_{\mathrm{v}}, v_i) df_{\mathrm{v}} \quad (6.17)$$

where the factor $1/2$ represent the binary breakage and the breakup fraction $f_{\mathrm{v}} = v_j/v_i$. The daughter bubble size distribution is calculated as

$$\beta(v_j, v_i) = \frac{\Omega(f_{\mathrm{v}}|v_i)}{\displaystyle\int_0^{0.5} \Omega(f_{\mathrm{v}}|v_i) df_{\mathrm{v}}} \quad (6.18)$$

6.4 Turbulence closure models

The two-fluid model requires the closure relations for the Reynolds stresses in the phase momentum equations. For the liquid phase, the effective stress tensor reads

$$\tau_l = \mu_{l,lam}\Big[\nabla \mathbf{U}_l + (\nabla \mathbf{U}_l)^{\mathrm{T}}\Big] - \frac{2}{3}\mu_{l,lam}(\nabla \cdot \mathbf{U}_l)\mathbf{I} + \tau_{l,turb} \quad (6.19)$$

where $\mu_{l,lam}$ is the laminar viscosity and $\tau_{l,turb}$ is the Reynolds stress tensor which can be modeled either by solving the Reynolds stress transport equation or by using the classical Boussinesq relation:

$$\tau_l = -\rho_l \mathbf{R}_l = \mu_{l,turb}\Big[\nabla \mathbf{U}_l + (\nabla \mathbf{U}_l)^{\mathrm{T}}\Big] - \frac{2}{3}\mu_{l,turb}(\nabla \cdot \mathbf{U}_l)\mathbf{I} - \frac{2}{3}\rho_l k_l \mathbf{I} \quad (6.20)$$

where $\mathbf{R}_l$ is the Reynolds stress and $\mu_{l,turb}$ is the turbulent viscosity. For the gas phase, the effective stress tensor is calculated as

$$\tau_g = (\mu_{g,lam} + \mu_{g,turb})\Big[\nabla \mathbf{U}_g + (\nabla \mathbf{U}_g)^{\mathrm{T}}\Big] - \frac{2}{3}(\mu_{g,lam} + \mu_{g,turb})(\nabla \cdot \mathbf{U}_g)\mathbf{I} \quad (6.21)$$

where $\mu_{g,turb}$ is the turbulent viscosity of gas phase and calculated from that of the liquid phase [39]: $\mu_{g,turb} = \rho_g/\rho_l \mu_{l,turb}$.

6.4.1 Two equation k-ε model

In the majority of publications on numerical simulations of turbulent bubbly flows, the standard k-ε model developed for single-phase flows has been employed to calculate the turbulent viscosity. The transport equations for k_l and ε_l are written as

$$\frac{\partial(\alpha_l \rho_l k_l)}{\partial t} + \nabla \cdot (\alpha_l \rho_l \mathbf{U}_l k_l) = \nabla \cdot \Big[\alpha_l\big(\mu_{l,lam} + \frac{\mu_{l,turb}}{\sigma_k}\big)\nabla k_l\Big] + \alpha_l(G_{k,l} - \rho_l \varepsilon_l) + S_{k,l} \quad (6.22)$$

$$\frac{\partial(\alpha_l \rho_l \varepsilon_l)}{\partial t} + \nabla \cdot (\alpha_l \rho_l \mathbf{U}_l \varepsilon_l) = \nabla \cdot \Big[\alpha_l\big(\mu_{l,lam} + \frac{\mu_{l,turb}}{\sigma_\varepsilon}\big)\nabla \varepsilon_l\Big] + \alpha_l \frac{\varepsilon_l}{k_l}(C_{\varepsilon 1} G_{k,l} - C_{\varepsilon 2}\rho_l \varepsilon_l) + S_{\varepsilon,l} \quad (6.23)$$

where $G_{k,l}$ is the production term of turbulent kinetic energy and calculated as

$$G_{k,l} = \nabla \mathbf{U}_l : \tau_{l,turb} \tag{6.24}$$

The shear-induced turbulent viscosity $\mu_{l,SI}$ is calculated as

$$\mu_{l,SI} = \rho_l C_\mu \frac{k_l^2}{\varepsilon_l} \tag{6.25}$$

In this work the standard k-ε model constants are used as $C_\mu = 0.09$, $C_{\varepsilon 1} = 1.44$, $C_{\varepsilon 2} = 1.92$, $\sigma_k = 1.0$, $\sigma_\varepsilon = 1.3$. The source terms $S_{k,l}$ and $S_{\varepsilon,l}$ represent the influence of the bubble phase on the liquid phase turbulence, i.e., bubble-induced turbulence. In this work, the source terms are set to zero. The bubble-induced turbulence is considered by adding an extra bubble-induced contribution to the shear-induced turbulent viscosity [40]:

$$\mu_{l,turb} = \mu_{l,SI} + \mu_{l,SI} \tag{6.26}$$

The bubble-induced turbulent viscosity $\mu_{l,BI}$ is calculated as

$$\mu_{l,BI} = \rho_l C_{\mu,B} d_B \alpha_g |\mathbf{U}_g - \mathbf{U}_l| \tag{6.27}$$

where the model constant $C_{\mu,B}$ is set to 0.6.

6.4.2 Reynolds stress model

The transport equation of the Reynolds stress $\mathbf{R}_l$ in the liquid phase is written as

$$\frac{\partial(\alpha_l \rho_l \mathbf{R}_l)}{\partial t} + \nabla \cdot (\alpha_l \rho_l \mathbf{U}_l \mathbf{R}_l) = \nabla \cdot \left[\alpha_l \left(C_s \rho_l \frac{k_l}{\varepsilon_l} \mathbf{R}_l \right) \nabla \mathbf{R}_l \right] + \alpha_l \rho_l \mathbf{P}_l + \alpha_l \rho_l \mathbf{\Phi}_l$$
$$- \frac{2}{3} \alpha_l \rho_l \varepsilon_l \mathbf{I} + \mathbf{S}_{R,l} \tag{6.28}$$

The production terms $\mathbf{P}_l$ is calculated as

$$\mathbf{P}_l = -\mathbf{R}_l \cdot \left[\nabla \mathbf{U}_l + (\nabla \mathbf{U}_l)^{\mathrm{T}} \right] \tag{6.29}$$

The pressure-strain term are modeled as

$$\mathbf{\Phi}_l = -C_1 \frac{\varepsilon_l}{k_t} \left(\mathbf{R}_l - \frac{2}{3} k_t \mathbf{I} \right) - C_2 \left(\mathbf{P}_l - \frac{2}{3} \mathrm{tr}(\mathbf{P}_l) \mathbf{I} \right) \tag{6.30}$$

The source term $\mathbf{S}_{R,l}$ accounts for the bubble-induced turbulence, which is also set to zero in this work. To consider the bubble-induced turbulence, the bubble-induced turbulent viscosity

$\mu_{l,BI}$ calculated in Eq. (6.27) is added to the laminar viscosity. The total turbulent kinetic energy is calculated from the trace of the total Reynolds stress:

$$k_t = \frac{1}{2} tr(\mathbf{R}_l + \mathbf{R}_{l,BI}) \tag{6.31}$$

The bubble-induced Reynolds stress is calculated following Arnold et al. [41]:

$$\mathbf{R}_{l,BI} = \alpha_g C_{\mathrm{vm}}[a(\mathbf{U}_r \otimes \mathbf{U}_r) + b(\mathbf{U}_r \cdot \mathbf{U}_r)\mathbf{I}] \tag{6.32}$$

where $C_{\mathrm{vm}} = 1.2$, $a = 0.1$ and $b = 0.3$ in this work.

To close the Reynolds stress model, the transport equation of the dissipation rate ε_l should be solved and it is expressed as

$$\frac{\partial(\alpha_l \rho_l \varepsilon_l)}{\partial t} + \nabla \cdot (\alpha_l \rho_l \mathbf{U}_l \varepsilon_l) = \nabla \cdot \left[\alpha_l \big(C_\varepsilon \rho_l \frac{k_l}{\varepsilon_l} \varepsilon_l\big) \nabla \mathbf{R}_l \right] + \alpha_l \frac{\varepsilon_l}{k_l}(C_{\varepsilon 1} G_{k,l} - C_{\varepsilon 2} \rho_l \varepsilon_l) + S_{\varepsilon,l} \tag{6.33}$$

where the source term $S_{\varepsilon,l}$ in the dissipation rate equation is set to zero in this work. The Reynolds stress model constants are listed as $C_1 = 1.8$, $C_2 = 0.6$, $C_s = 0.22$, $C_{\varepsilon 1} = 1.44$, $C_{\varepsilon 2} = 1.92$, $C_\varepsilon = 0.15$.

6.5   Numerical solution

6.5.1   Model implementation

OpenFOAM is employed as the basic framework which is a flexible and efficient C++ library for manipulating scalar, vector and tensor fields [42]. In our developed solver, the discretized population balance equations are constructed using the C++ template: `PrtList<fvScalarMatrix>`. The partial differential equations are discretized with the operator `fvc` (finite volume calculus) and `fvm` (finite volume method). The `fvc` functions calculate the explicit terms, while the `fvm` functions are used to discretize the implicit derivatives. To calculate the triple integration in the breakup frequency term, the incomplete Gamma function is implemented following the work of Alopaeus et al. [43]. Figure 6.1 shows the calculated results of breakup frequency and daughter size distribution. The dissipation rate of kinetic energy has obvious influence on the breakup frequency and daughter size distribution. Meanwhile, the breakup frequency is not sensitive to the different values of the minimum eddy size.

Since the liquid phase is not present in the whole domain of the bubble colmn, the discretized turbulence model equations result in the singular system of linear algebraic equations. Following the work of Oliveira and Issa [44], the phase-intensive forms of the turbulence model equations are employed by dividing the original transport equations by the liquid volume fraction. Oliveira and Issa found the phase-intensive formulation gives stable solutions and the predicted results have quite small difference from those predicted by the original equations.
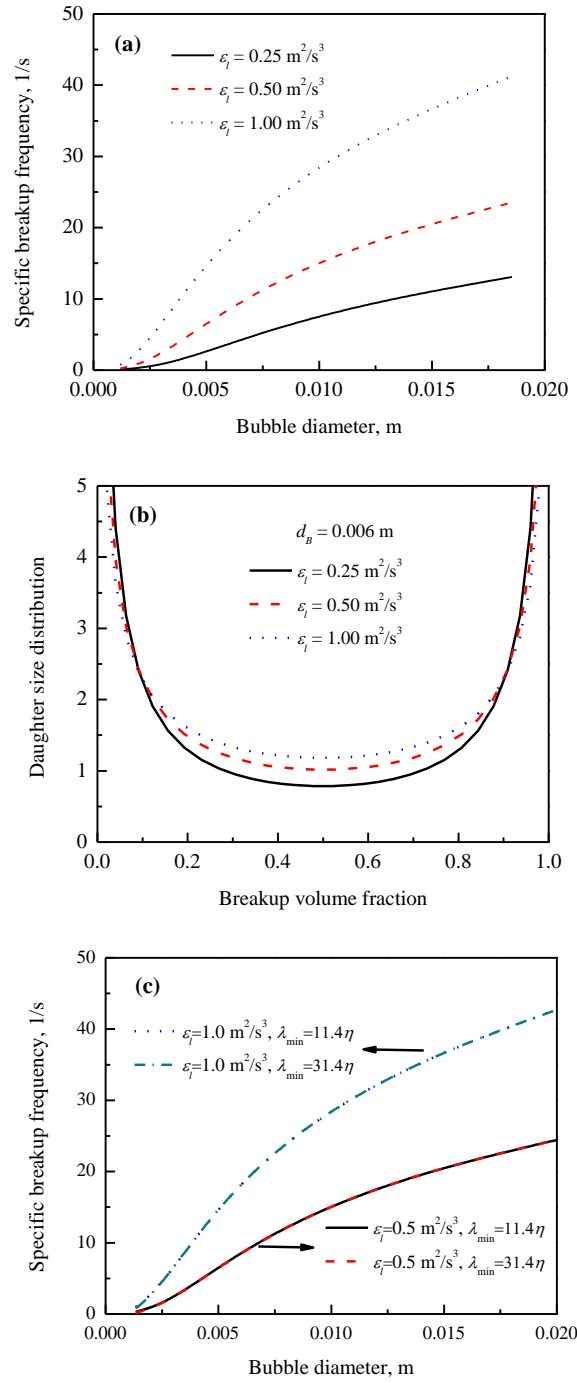
Figure 6.1: (a) Specific breakup frequency; (b) daughter size distribution; (c) effect of the minimum eddy size.
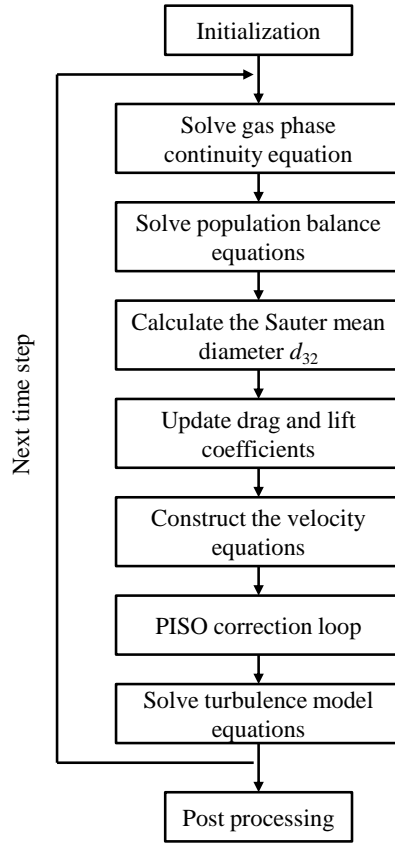
Figure 6.2: Solution algorithm implemented in the CFD-PBM coupled solver.

Table 6.1: The numerical schemes used in the test cases

Term	Discretization scheme
$\dfrac{\partial \psi}{\partial t}$	`Euler`
$\nabla \psi$	`cellMDLimited Gauss linear 1`
$\nabla \cdot (\mathbf{U}_k \mathbf{U}_k)$	`Gauss limitedLinearV 1`
$\nabla \cdot (\mathbf{U}_\mathrm{g} \alpha_\mathrm{g})$	`Gauss limitedLinear01 1`
$\nabla \cdot (\mathbf{U}_l k_l)$	`Gauss limitedLinear 1`
$\nabla \cdot (\mathbf{U}_l \varepsilon_l)$	`Gauss limitedLinear 1`
$\nabla \cdot (\mathbf{U}_l \mathbf{R}_l)$	`Gauss limitedLinear 1`
$\nabla \cdot \tau_k$	`Gauss linear`
$\nabla^2 \psi$	`Gauss linear corrected`
$\nabla^\perp \psi$	`corrected`
$(\psi)_f$	`linear`

The linear equation systems resulting from the discretization procedure are solved in a segregated fashion. The pressure-velocity coupling is handled using the PISO solution algorithm [45]. The interphase coupling terms in the momentum equations are treated using the semi-implicit method [46]. The pressure equation is solved and the predicted phase velocities are corrected by the pressure change. The solution procedure is schematized in Figure 6.2. Table 6.1 gives the details of the discretization schemes used for the different terms in the governing equations.

6.5.2   Test case descriptions

The bubble column (2.0 m height and 0.2 m i.d.) built by Rampure et al. [27] is simulated using the CFD-PBM method. It contained a batch liquid with unexpanded height of 1.0 m. Air was supplied through the column bottom at 0.10 m/s. The heterogeneous flow regime was formed with high gas holdup. The simulations are also performed to predict the hydrodynamics in a bubble column of 2.0 m height and 0.19 m diameter. The experimental data of gas holdup, liquid velocity and turbulent kinetic energy were measured in this column [47–49]. The static water height was 0.95 m. The heterogeneous flow regime was achieved by operating the column at a superficial gas velocity of 0.12 m/s.

Initially, the static water exists in the bubble columns and the gas holdup is set to be zero within the static water. The gas distributor is treated as a uniform inlet with the gas volume fraction of 1.0. The liquid inlet velocity is set to zero for all test cases because of no water supply into the bubble columns. The pressure at the inlet is specified using the zero gradient boundary condition. At the outlet, the pressure is specified as atmospheric pressure. The no-slip boundary condition is applied at the wall for all velocities. The wall function proposed by Launder and Spalding [50] is used to specify the turbulent quantities. The law of the wall for mean velocity gives

$$U^* = \frac{1}{\kappa}\ln(Ey^*) \tag{6.34}$$

with

$$y^* = \frac{\rho_l C_\mu^{1/4} k_P^{1/2} y_P}{\mu_l} \tag{6.35}$$

where κ is the von Karman constant, $\kappa = 0.42$, E is an empirical constant, $E = 9$. In OpenFOAM, the log-law equation is employed when $y^* > 11.6$.

The turbulent kinetic energy is solved in the whole domain including the wall-adjacent cells. At the wall, the zero gradient boundary condition is used for turbulent kinetic energy. The

production term of turbulent kinetic energy and its dissipation rate at the wall-adjacent cells are computed as

$$G_P = \frac{\mu_l \mathbf{U}_P C_\mu^{1/4} k_P^{1/2}}{\rho_l \kappa y_P} \tag{6.36}$$

$$\varepsilon_P = \frac{C_\mu^{3/4} k_P^{3/2}}{\kappa y_P} \tag{6.37}$$

where y_P is the distance from point P to the wall, $\mathbf{U}_P$ is the mean velocity at the point P, and k_P is the turbulent kinetic energy at the point P.

Table 6.2: Bubble classes used in the simulations

(a) 10 bubble classes										
index	1	2	3	4	5	6	7	8	9	10
diameter (mm)	3.1	3.9	4.9	6.1	7.7	9.7	12.2	15.4	19.4	24.5
(a) 20 bubble classes										
index	1	2	3	4	5	6	7	8	9	10
diameter (mm)	2.3	2.6	3.0	3.4	3.9	4.5	5.1	5.9	6.7	7.7
index	11	12	13	14	15	16	17	18	19	20
diameter (mm)	8.8	10.1	11.6	13.2	15.2	17.4	19.9	22.7	26.0	29.8

Simulations are conducted using two-dimensional computational meshes with 10 mm cell size. The diameters of 10 and 20 bubble classes are listed in Table 6.2. The simulations are carried out for 60 s real time and the time-averaged results are obtained in the last 55 s. The governing equations are solved in a transient way using adaptive time step method to improve the stability. The time step is adapted by the Courant number. The Courant number is defined as

$$\mathrm{Co} = \frac{\Delta t |\mathbf{U}_r|}{\Delta x} \tag{6.38}$$

where Δt is time step, $\mathbf{U}_r$ is the relative velocity through the cell, Δx is the cell size in the direction of relative velocity. The maximum Courant number is set to 0.1.

6.6 Results and discussion

6.6.1 Test case I: superficial gas velocity of 0.10 m/s

Sensitivity study on the bubble number is performed through the 10 and 20 bubble classes for the k-ε model and the RSM. The bubble-induced turbulence is considered in the two turbulence models. Figure 6.3 shows the effect of the number of bubble classes on the gas

holdup and axial liquid velocity when using the k-ε model. Clearly, increasing the number of bubble classes does not significantly increase the agreement with experimental data. However, much more computational time is needed when increasing the number of classes to 20. Figure 6.4 shows the effect of the number of bubble classes on the gas holdup and axial liquid velocity predicted by the RSM. Also, the simulation results of the RSM are not sensitive to the number of bubble classes. From Figures 6.3 and 6.4, the 10 bubble classes are sufficient to resolve the bubble size distribution. The profile of gas holdup is well predicted when using the 10 and 20 bubble classes. However, small underestimation on axial liquid velocity is observed for the k-ε model and RSM.
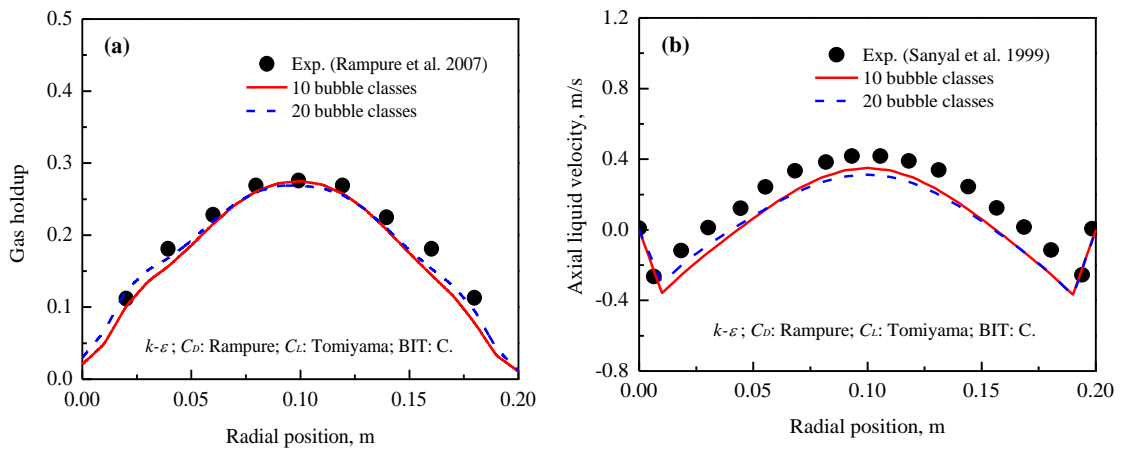

Figure 6.3: Effect of the number of bubble classes on the gas holdup and axial liquid velocity predicted by the k-ε model. BIT: bubble-induced turbulence; C.: considered.
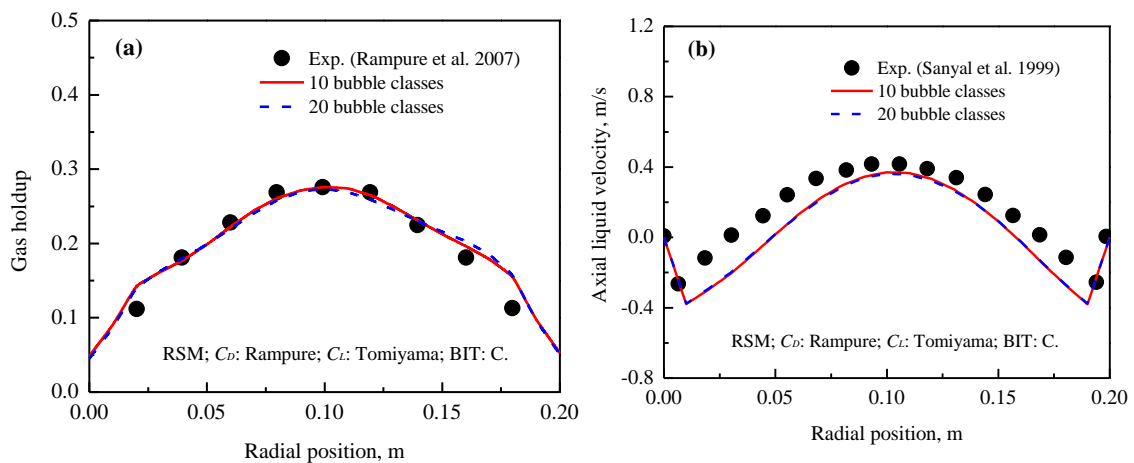

Figure 6.4: Effect of the number of bubble classes on the gas holdup and axial liquid velocity predicted by the RSM.

Figure 6.5 displays the effect of the lift coefficients of the single bubble and the bubble swarm on the simulated results of the k-ε model. The Rampure model is adopted to account for the swarm effect on the drag coefficient. In Figure 6.5a the Tomiyama model gives better prediction on gas holdup than the Behzadi model, although it was formulated based on the data of single bubbles. The Tomiyama model has the lift coefficient in the range $0 < C_L \leqslant 0.288$ for the small bubbles with diameter less than 6 mm, whereas the negative values in the range $-0.29 < C_L \leqslant 0$ are used for the large bubbles with diameter larger than 6 mm. The negative lift coefficient makes the bubbles move towards the center of the bubble column. However, only the positive lift coefficients are predicted by the Behzadi model. The positive coefficient leads to the bubble migration towards the walls. Thus, the flat profile of gas holdup is predicted by the Behzadi model. In Figure 6.5b both lift coefficient models give the underestimation on the axial liquid velocity.
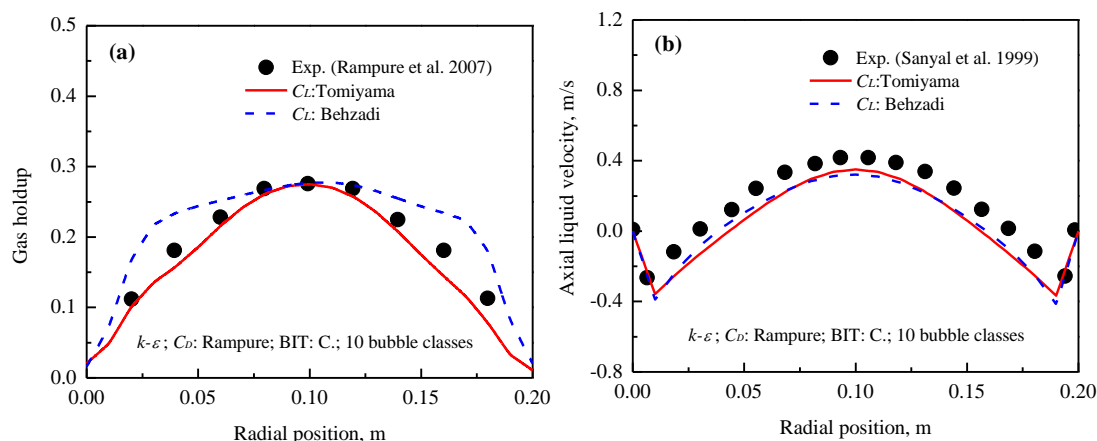

Figure 6.5: Effect of the lift coefficient on the gas holdup and axial liquid velocity predicted by the k-ε model.

Figure 6.6 shows the effect of the lift coefficient on the gas holdup and axial liquid velocity predicted by the RSM. The poor prediction on gas holdup and axial liquid velocity is also observed for the Behzadi lift coefficient. Although the Behzadi lift coefficient was originally proposed for the pipe flows, its applicability is not general in simulating the bubble column flows. Since the strong liquid circulation exists in the bubble columns, the bubble column flow is quite different from the concurrent flow in the pipe.

In Figure 6.7 the predicted profiles of turbulent kinetic energy and its dissipation rate are compared between the k-ε model and the RSM. For the k-ε model, the radial profile of turbulent kinetic energy exhibits the two maximums at the two sides near the walls. However, the parabolic profile is predicted by the RSM. In the RSM, the bubble-induced kinetic energy is added to the shear-induced kinetic energy. Therefore, the large kinetic energy is predicted

by the RSM in the column center. In Figure 6.7b the simulated dissipation rate increases from the center to the wall for the k-ε model and the RSM. Near the walls, the smaller values are predicted by the RSM and the large difference is observed. It should be mentioned that, due to the lack of experimental data of the turbulence quantities in this bubble column, the applicability of the k-ε model and the RSM cannot be judged in predicting the turbulence parameters. Hence, the turbulence models should be further investigated by simulating other test cases.
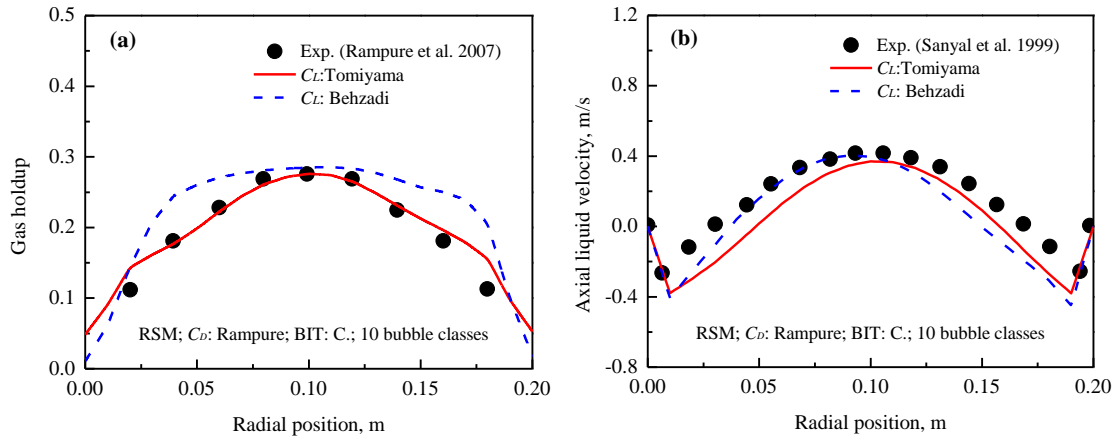

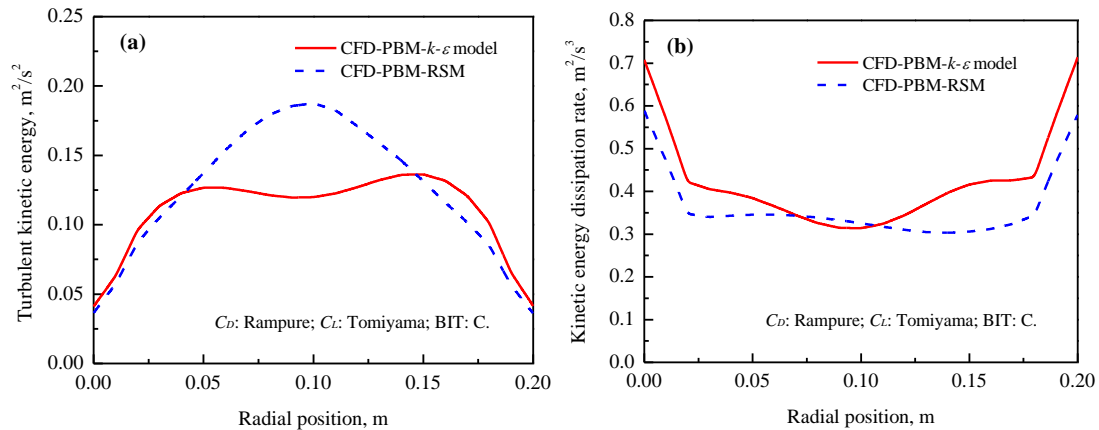**Figure 6.6:** Effect of the lift coefficient on the gas holdup and axial liquid velocity predicted by the RSM.

Figure 6.7: (a) Turbulent kinetic energy and (b) dissipation rate predicted by the k-ε model and the RSM.

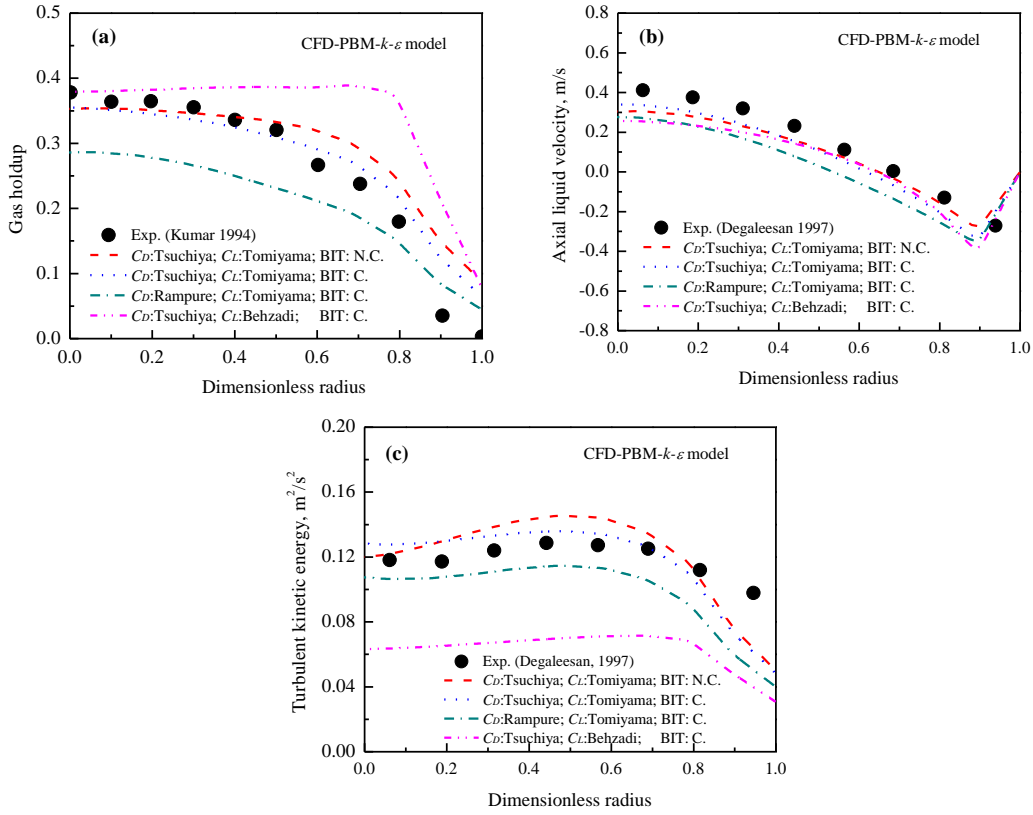## 6.6.2   Test case II: superficial gas velocity of 0.12 m/s

Figure 6.8: Effect of the different closure models with the k-ε model. N.C.: not considered.

To further assess the k-ε and Reynolds stress models in the CFD-PBM method, the bubble column operated at 0.12 m/s is simulated. Figure 6.8 shows the experimental and simulated results of gas holdup, axial liquid velocity and turbulent kinetic energy. The different models for drag and lift coefficients are used with the k-ε model. The bubble size distribution is represented by 10 bubble classes. For the gas holdup profile in Figure 6.8a, the best prediction is obtained by the combination of the Tsuchiya drag coefficient, Tomiyama lift coefficient and bubble-induced turbulence model. However, the gas holdup profile is poorly predicted by the other model combinations. The Behzadi lift coefficient predicts the flat profile when it works with the Tsuchiya drag coefficient. Furthermore, it is found that the bubble-induced turbulence should be taken into account to obtain good agreement with the experimental data. In Figure 6.8b the good prediction on axial liquid velocity is also obtained using the Tsuchiya drag coefficient, Tomiyama lift coefficient and bubble-induced turbulence model. The under-prediction is given by the Rampure drag coefficient. This is because the Rampure drag coefficient is smaller than the Tsuchiya drag coefficient. In Figure 6.8c the

best prediction on turbulent kinetic energy is obtained when the k-ε model is used with the Tsuchiya drag coefficient, Tomiyama lift coefficient and bubble-induced turbulence model.
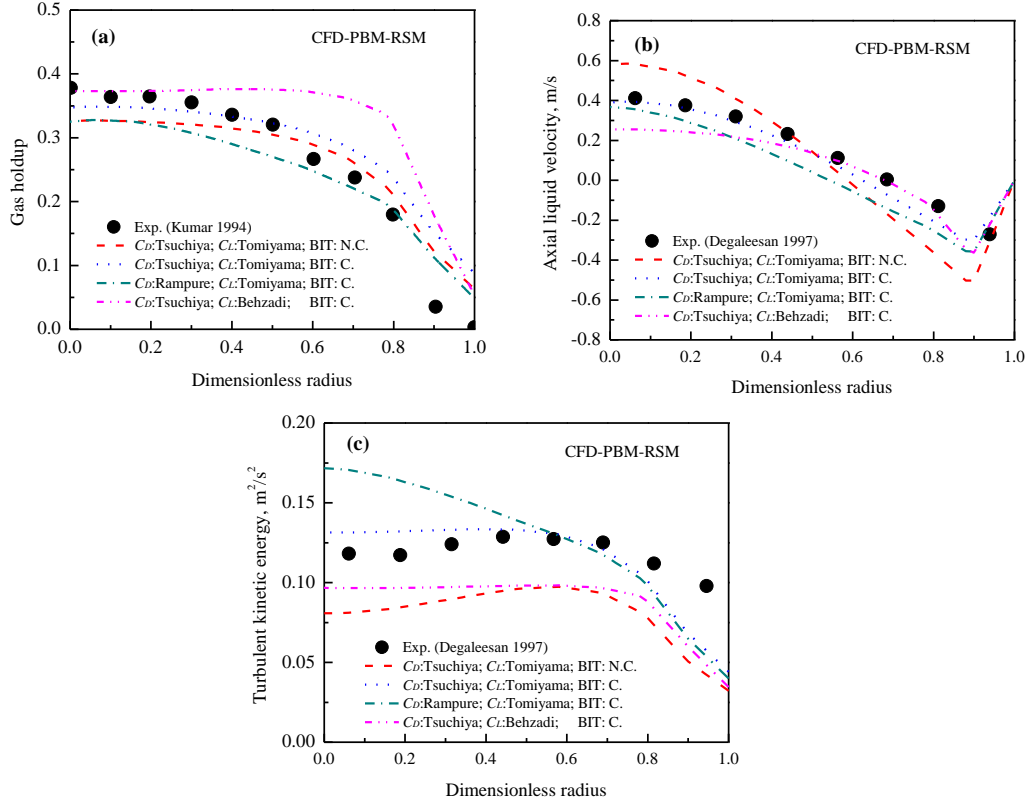

Figure 6.9: Effect of the different closure models with the RSM.

Figure 6.9 gives the profiles of gas holdup, axial liquid velocity and turbulent kinetic energy predicted by the RSM with different closure models. It is seen from Figure 6.9a that good agreement is obtained when the RSM is used with the Tsuchiya drag coefficient, Tomiyama lift coefficient and the bubble-induced turbulence model. Similar to the k-ε model, the RSM with the Behzadi lift coefficient predicts the flat profile of gas holdup in the column center. Although the Rampure drag coefficient was proposed to account for the swarm effect, it is still poor in predicting the gas holdup in the bubble column. The swarm effect in the heterogeneous flow regime needs to be modeled based on more sound physics. In Figures 6.9b and 6.9c the prediction on axial liquid velocity and turbulent kinetic energy is greatly improved when the RSM works with the bubble-induced turbulence, Tsuchiya drag coefficient and Tomiyama lift coefficient. Without the bubble-induced turbulence model, the predicted profile of turbulent kinetic energy is much lower than the experimental data. This discrepancy is due to the lack of the bubble-induced kinetic energy. For the Rampure drag coefficient,

although the bubble-induced turbulence is considered, the large over-prediction on turbulent kinetic energy is observed in the column center. Similar to the k-ε model, the RSM with the Behzadi lift coefficient gives under-prediction on the turbulent kinetic energy.

From Figures 6.8 and 6.9, the closure models of the drag and lift coefficients and the bubble-induced turbulence play very important roles in evaluating the performances of the k-ε and the RSM. The simulated results are determined by the combined effect of various models. In principle, the RSM is more physically sound than the k-ε model in handling the anisotropic flows. However, the uncertainty in the interfacial force terms and the bubble-induced turbulence model would ruin the validity of the RSM. Some effort should be made to establish more accurate models of the interfacial force and bubble-induced turbulence. Furthermore, when the population balance is considered, the bubble coalescence and breakup should be accurately modeled. The multi-fluid model framework would be more reasonable to calculate the velocities of different bubble classes.
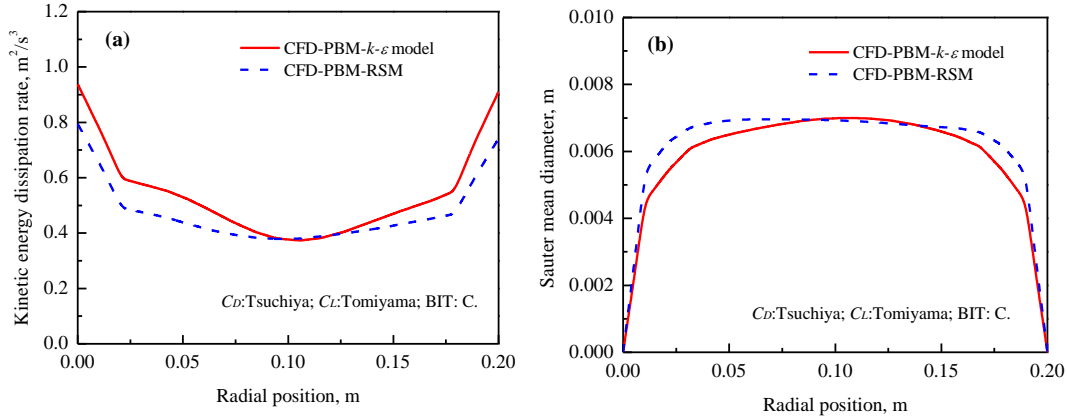
Figure 6.10: Comparison of the dissipation rate and Sauter mean diameter predicted by the k-ε model and the RSM.

Finally, the comparison of the profiles of the dissipation rate and Sauter mean diameter is made for the two turbulence models. In Figure 6.10a, the larger values of the dissipation rate are predicted by the k-ε model near the walls. Since the bubble size distribution is influenced by the dissipation rate, the large difference in the profiles of Sauter mean diameter is also found near the walls. From Figure 6.1a, the increase in the dissipation rate promotes the bubble breakup. Thus, the smaller values of the bubble diameter are predicted by the k-ε model, as shown in Figure 6.10b. The profiles of the dissipation rate and Sauter mean diameter should be validated in the future study.

6.7 Conclusions

The heterogeneous bubble column flows are simulated for the evaluation on the k-ε and Reynolds stress models. The coupled CFD-PBM method is implemented into OpenFOAM. Simulations are compared with the experimental data in the literature. For the bubble column operated at 0.10 m/s, minor difference is found in the predicted profiles of gas holdup and axial liquid velocity when using 10 and 20 bubble classes. The Behzadi lift coefficient gives poor prediction when it is used with the k-ε model and the RSM. With the Rampure drag coefficient, Tomiyama lift coefficient and bubble-induced turbulence, the k-ε model and the RSM gives good prediction on gas holdup.

For the bubble column operated at 0.12 m/s, the k-ε model should work with the Tsuchiya drag coefficient and Tomiyama lift coefficient to get good prediction. The bubble-induced turbulence should also be considered in the k-ε model. Similarly, good agreement with experimental data can be obtained when the RSM is used with the Tsuchiya drag coefficient, Tomiyama lift coefficient and bubble-induced turbulence model. For the k-ε model, the smaller bubble diameters are predicted, because the larger values of the dissipation rate are obtained by this model.

Literature

[1] W. D. Deckwer, Bubble column reactors, John Wiley and Sons, New York, 1992.

[2] G. Tryggvason, A. Esmaeeli, J. C. Lu, S. Biswas, Direct numerical simulations of gas/liquid multiphase flows, Fluid Dynamics Research 38 (2006) 660–681.

[3] A. Sokolichin, G. Eigenberger, A. Lapin, Simulation of buoyancy driven bubbly flows: established simplifications and open questions, AIChE Journal 50 (2004) 24–45.

[4] D. Zhang, N. G. Deen, J. A. M. Kuipers, Numerical simulation of the dynamic flow behavior in a bubble column: A study of closures for turbulence and interface forces, Chemical Engineering Science 61 (2006) 7593–7608.

[5] D. Law, F. Battaglia, T. J. Heindel, Model validation for low and high superficial gas velocity bubble column flows, Chemical Engineering Science 63 (2008) 4605–4616.

[6] M. V. Tabib, S. A. Roy, J. B. Joshi, CFD simulation of bubble column: an analysis of interphase forces and turbulence models, Chem Eng J 139 (2008) 589–614.

[7] K. Ekambara, M. T. Dhotre, CFD simulation of bubble column, Nuclear Engineering and Design 240 (2010) 963–969.

[8] P. Chen, J. Sanyal, M. P. Dudukovic, CFD modeling of bubble columns flows: implementation of population balance, Chemical Engineering Science 59 (2004) 5201–5207.

[9] T. F. Wang, J. F. Wang, Y. Jin, A CFD-PBM coupled model for gas-liquid flows, AIChE Journal 52 (2006) 125–140.

[10] R. Bannari, F. Kerdouss, B. Selma, A. Bannari, P. Proulx, Three-dimensional mathematical modeling of dispersed two-phase flow using class method of population balance in bubble columns, Computers and Chemical Engineering 32 (2008) 3224–3237.

[11] M. R. Bhole, J. B. Joshi, D. Ramkrishna, CFD simulation of bubble columns incorporating population balance modeling, Chemical Engineering Science 63 (2008) 2267–2282.

[12] K. Ekambara, K. Nandakumar, J. B. Joshi, CFD simulation of bubble column reactor using population balance, Ind Eng Chem Res 47 (2008) 8505–8516.

[13] O. Borchers, C. Busch, A. Sokolichin, G. Eigenberger, Applicability of the standard k-ε turbulence model to the dynamic simulation of bubble columns: Part II. Comparison of detailed experiments and flow simulations, Chemical Engineering Science 54 (1999) 5927–5935.

[14] R. F. Mudde, O. Simonin, Two- and three-dimensional simulations of a bubble plume using a two-fluid model, Chemical Engineering Science 54 (1999) 5061–5069.

[15] D. Pfleger, S. Gomes, N. Gilbert, H. G. Wagner, Hydrodynamic simulations of laboratory scale bubble columns. Fundamental studies of the Eulerian-Eulerian modeling approach, Chemical Engineering Science 54 (1999) 5091–5099.

[16] A. Sokolichin, G. Eigenberger, Applicability of the standard k-ε turbulence model to the dynamic simulation of bubble columns: Part I. Detailed numerical simulations, Chemical Engineering Science 54 (1999) 2273–2284.

[17] A. Behzadi, R. I. Issa, H. Rusche, Modeling of dispersed bubble and droplet flow at high phase fractions, Chemical Engineering Science 59 (2003) 759–770.

[18] B. Selma, R. Bannari, P. Proulx, A full integration of a dispersion and interface closures in the standard k-ε model of turbulence, Chem Eng Sci 65 (2010) 5417–5428.

[19] D. Cokljat, M. Slack, S. A. Vasquez, Reynolds-stress model for Eulerian multiphase. In: 4th International Symposium on Turbulence, Heat and Mass transfer, Turkey, 2003.

[20] N. G. Deen, T. Solberg, B. H. Hjertager, Large eddy simulation of the gas-liquid flow in a square cross-sectioned bubble column, Chemical Engineering Science 56 (2001) 6341–6349.

[21] M. T. Dhotre, B. Niceno, B. L. Smith, Large eddy simulation of a bubble column using dynamic sub-grid scale model, Chemical Engineering Journal 136 (2008) 337–348.

[22] B. Niceno, M. T. Dhotre, N. G. Deen, One-equation sub-grid scale (SGS) modeling for Euler-Euler large eddy simulation (EELES) of dispersed bubbly flow, Chemical Engineering Science 63 (2008) 3923–3931.

[23] C. Laborde-Boutet, F. Larachi, N. Dromard, O. Delsart, D. Schweich, CFD simulation of bubble column flows: Investigations on turbulence models in RANS approach, Chemical Engineering Science 64 (2009) 4399–4413.

[24] H. A. Jakobsen, H. Lindborg, C. A. Dorao, Modeling of bubble column reactors: progress and limitations, Industrial & Engineering Chemistry Research 44 (2005) 5107–5151.

[25] H. Marschall, R. Mornhinweg, A. Kossmann, S. Oberhauser, K. Langbein, O. Hinrichsen, Numerical simulation of dispersed gas/liquid flows in bubble columns at high phase fractions using OpenFOAM. Part I: Modeling basics, Chemical Engineering & Technology 34 (2011) 1311–1320.

[26] K. Tsuchiya, A. Furumoto, L. S. Fan, J. Zhang, Suspension viscosity and bubble size velocity in liquid-solid fluidized beds, Chemical Engineerig Science 52 (1997) 3053–3066.

[27] M. R. Rampure, A. A. Kulkarni, V. V. Ranade, Hydrodynamics of bubble column reactors at high gas velocity: Experiments and Computational Fluid Dynamics (CFD) simulations, Industrial & Engineering Chemistry Research 46 (2007) 8431–8447.

[28] A. Tomiyama, Drag and lift and virtual mass forces acting on a single bubble. In: 3rd International Symposium on Two-Phase Flow Expressioning and Experimentation, Pisa, Italy, 2004.

[29] S. Kumar, D. Ramkrishna, On the solution of population balance equations by discretization-I. A fixed pivot technique, Chemical Engineering Science 51 (1996) 1311–1332.

[30] M. Smith, T. Matsoukas, Constant-number Monte Carlo simulation of population balances, Chemical Engineerig Science 53 (1998) 1777–1786.

[31] S. Bove, T. Solberg, B. H. Hjertager, A novel algorithm for solving population balance equations: the parallel parent and daughter classes. Deviation, analysis and testing, Chemical Engineerig Science 60 (2005) 1449–1464.

[32] D. L. Marchisio, R. D. Vigil, R. O. Fox, Quadrature method of moments for aggregation-breakage process, Journal of Colloid and Interface Science 258 (2003) 322–334.

[33] B. Selma, R. Bannari, P. Proulx, Simulation of bubbly flows: Comparison between direct quadrature method of moments (DQMOM) and method of classes (CM), Chemical

Engineerig Science 65 (2010) 1925–1941.

[34] Y. X. Liao, D. Lucas, A literature review on mechanisms and models for the coalescence process of fluid particles, Chemical Engineerig Science 65 (2010) 2815–2864.

[35] H. Luo, Coalescence, breakup and liquid circulation in bubble column reactors, Ph.D. thesis, The Norwegian Institute of Technology, Trondheim, Norway (1993).

[36] Q. Wu, S. Kim, M. Ishii, One-group interfacial area transport in vertical bubbly flow, International Journal of Heat and Mass Transfer 41 (1998) 1103–1112.

[37] T. F. Wang, J. F. Wang, Y. Jin, Theoretical prediction of flow regime transition in bubble columns by the population balance model, Chemical Engineerig Science 60 (2005) 6199–6209.

[38] H. Luo, H. F. Svendsen, Theoretical model for drop and bubble breakup in turbulent dispersions, AIChE Journal 42 (1989) 1225–1233.

[39] H. A. Jakobsen, B. H. Sanaes, S. Grevskott, H. F. Svendsen, Modeling of vertical bubble-driven flows, Industrial & Engineering Chemistry Research 36 (1997) 4052–4074.

[40] Y. Sato, M. Sadatomi, K. Sekoguchi, Momentum and heat transfer in two-phase bubble flow, International Journal of Multiphase Flow 7 (1981) 167–177.

[41] G. S. Arnold, D. A. Drew, R. T. Lahey, Derivation of constitutive equations for interfacial force and Reynolds stress for suspension of spheres using ensemble cell averaging, Chemical Engineering Communications 86 (1989) 43–54.

[42] OpenCFD Ltd., OpenFOAM 2.1.1 User's Guide, UK (2012).

[43] V. Alopaeus, J. Koskinen, K. I. Keskinen, Simulation of the population balances for liquid-liquid systems in a nonideal stirred tank. Part 1 Description and qualitative validation of the model, Chemical Engineering Science 54 (1999) 5887–5899.

[44] P. J. Oliveira, R. I. Issa, Numerical aspects of an algorithm for the Eulerian simulation of two-phase flows, International Journal for Numerical Methods in Fluids 43 (2003) 1177–1198.

[45] R. Issa, Solution of the implicitly discretized fluid flow equations by operator-splitting, Journal of Computational Physics 62 (1985) 40–65.

[46] H. Rusche, Computational fluid dynamics of dispersed two-phase flows at high phase fractions, Ph.D. thesis, Imperial College of Science, Technology and Medicine, London, UK (2002).

[47] S. B. Kumar, Computed tomographic measurements of void fraction and modeling of the flow in bubble columns, Ph.D. thesis, Florida Atlantic University, Florida, USA (1994).

[48] J. Sanyal, S. VaHsquez, S. Roy, M. P. Dudukovic, Numerical simulation of gas-liquid dynamics in cylindrical bubble column reactors, Chemical Engineering Science 54 (1999) 5071–5083.

[49] S. Degaleesan, Fluid dynamic measurements and modeling of liquid mixing in bubble columns, Ph.D. thesis, Washington University, St. Louis, Missouri, USA (1997).

[50] B. E. Launder, D. B. Spalding, The numerical computation of turbulent flows, Computer Methods in Applied Mechanics and Engineering 3 (1974) 269–289.

Chapter 7

Summary and Outlook

7.1 Summary

Two-fluid modeling of gas-solid and gas-liquid flows is performed in the thesis. The different CFD solvers are implemented in the open source C++ package OpenFOAM. The numerical issues are discussed by investigating the effect of total variation diminishing (TVD) convection schemes. The different turbulence closures are also studied for the gas-liquid solver. The two-fluid solvers are applied for simulating the tube erosion in the fluidized bed, the fluidized bed methanation reactor and the bubble column reactors.

Five different TVD schemes are employed to discretize the convection terms of phase velocity and solid volume fraction. Simulated results agree well with the experimental data in the literature. For the discretization of the phase velocity convection terms, the five schemes give quite similar time-averaged radial profiles of particle axial velocity. The predicted bubbles in the bed with a central jet are not influenced by the different schemes. For the discretization of the solid volume fraction convection terms, the limitedLinear01, Sweby01 and vanLeer01 schemes give the converged and reasonable solutions, whereas the SuperBee01 and MUSCL01 schemes diverge the solutions. By using the faceLimited gradient scheme, the TVD scheme becomes more diffusive.

Tube erosion in a bubbling fluidized bed is numerically studied using the Eulerian-Eulerian method coupled with a monolayer kinetic energy dissipation model. The hydrodynamical simulations are performed under conditions with three different superficial gas velocities. The time-averaged bubble frequency and bubble rise velocity are calculated to characterize the bed hydrodynamics. The erosion rates of two target tubes are simulated and the influence of the bubble behaviors on erosion rates is evaluated. Compared with the experimental data in the literature, the bubble behaviors are well captured by the simulations. Good agreement between the calculated and measured erosion rates is also obtained for the two target tubes. The bubble behaviors around the tubes have direct impact on the tube erosion. Only small discrepancies in the calculated erosion rates are found when using different particle-wall restitution coefficients and specularity coefficients.

Numerical investigations of hydrodynamics and kinetic reactions in a fluidized bed methanation reactor are carried out by coupling methanation kinetics with the two-fluid flow model. The gas-solid reacting flow models are implemented within OpenFOAM. The grid resolution is investigated using 2D and 3D meshes. The bed height is reasonably predicted with the Gidaspow and Syamlal models. Simulated results are compared against experimental data in literature. The simulated axial species concentrations agree well with the measured results at the end of the bed. The effects of different operating parameters are evaluated using the established models. The increase in the gas inlet velocity results in more dilute solid concentration and larger bed expansion. The weak bed expansion results from the methanation reaction with gas volume reduction. The methane concentration is increased when increasing catalyst inventory in the reactor. The addition of water into the feedstock with low H_2/CO ratio benefits the methanation reaction.

The heterogeneous flows in bubble columns are simulated for the evaluation on the k-ε and Reynolds stress models in the coupled CFD-PBM method. For the bubble column operated at 0.10 m/s, it is found that minor difference exists in the predicted profiles of gas holdup and axial liquid velocity when using the 10 and 20 bubble classes. The Behzadi lift coefficient gives poor predictions when it works with the k-ε model and the RSM. Working with the Rampure drag coefficient, Tomiyama lift coefficient and bubble-induced turbulence, the k-ε model and the RSM give good prediction on gas holdup. For the bubble column operated at 0.12 m/s, the k-ε model should work with the Tsuchiya drag coefficient and Tomiyama lift coefficient to get good prediction. The bubble-induced turbulence should be also considered in the k-ε model. Good agreement with experimental data can be obtained when the RSM is used with the Tsuchiya drag coefficient, Tomiyama lift coefficient and bubble-induced turbulence model. For the k-ε model, the smaller bubble diameters are predicted, because the larger values of the dissipation rate are obtained by this model.

7.2 Outlook

For the gas-solid flow modeling, it is found that the use of SuperBee01 and MUSCL01 schemes for solid volume fraction convection terms destroys the solution convergence. By using the SuperBee01 and MUSCL01 schemes, solid volume fraction cannot be effectively limited to be lower than the packing limit. When solid volume fraction reaches the packing limit, the radial distribution function g_0 becomes infinite which results in the solution divergence. This problem could be solved by using the deferred correction method. In the deferred correction approach, the part of the convection term corresponding to upwind differencing is implicitly built into the matrix, and the other part is added into the source term. The deferred correction method can be studied in the future to improve the numerical stability.

For the practical applications, the gas-solid solver can be used for simulating other process of industrial importance, e.g. the biomass pyrolysis in the fluidized beds, the fluidized bed

combustion, the fluidized bed MTO process, some chemical vapor deposition processes in the fluidized beds. The two-fluid model is computationally economical for simulating the large-scale reactors. The two-fluid model solver can be extended to the multi-fluid solver for simulating the three-phase reactors. With the development in the catalytic kinetics, some multiphase reaction processes can also be simulated using the two-fluid model with the reaction models.

For the gas-liquid flows, especially the heterogeneous flows, the gas-liquid two-fluid modeling approach still remains certain open questions due to the uncertainties regarding the phase interaction terms, turbulence closure schemes, and multiple bubble sizes. The CFD-PBM method is very promising and should be further studied. From our work, it is found that the closure models for drag and lift coefficients and the bubble-induced turbulence model play very important roles when evaluating the performances of the k-ε and the RSM. The simulated results are determined by the combined effect of various models. In principle, the RSM is more physically sound than the k-ε model in handling the anisotropic flows. However, the uncertainty in the interfacial force terms and the bubble-induced turbulence model would destroy the validity of the RSM. The effort should be made to establish more accurate models for the interfacial force and bubble-induced turbulence. When the population balance is considered, the bubble coalescence and breakup should be accurately modeled. Moreover, the multi-fluid model framework would be more reasonable to calculate the velocities of different bubble classes.

Appendix A

List of Publications

Publications in Journals

- Yefei Liu, Olaf Hinrichsen. Numerical simulation of tube erosion in a bubbling fluidized bed with a dense tube bundle. Chemical Engineering & Technology, 2013, 36, 635-644.

- Yefei Liu, Olaf Hinrichsen. CFD simulation of hydrodynamics and methanation reactions in a fluidized-bed reactor for the production of synthetic natural gas. Industrial & Engineering Chemistry Research, 2014, 53, 9348-9356.

- Yefei Liu, Olaf Hinrichsen. CFD modeling of bubbling fluidized beds using OpenFOAM®: Model validation and comparison of TVD differencing schemes. Computers and Chemical Engineering, 2014, 69, 75-88.

- Yefei Liu, Olaf Hinrichsen. Study on CFD-PBM turbulence closures based on k-ε and Reynolds stress models for heterogeneous bubble column flows. Computers & Fluids, 2014, 105, 91-100.

Refereed conference proceedings

- Yefei Liu, Olaf Hinrichsen. Eulerian two-fluid modeling for erosion simulation in bubbling fluidized bed combustor. 2nd Colloquium of Munich School of Engineering. Technische Universität München, Garching b. München, Germany, 2012.

- Yefei Liu, Olaf Hinrichsen. Eulerian-Eulerian simulation of immersed tube erosion in a bubbling fluidized bed with a dense tube bundle. 9th European Congress of Chemical Engineering, The Hague, The Netherlands, 2013.

- Yefei Liu, Olaf Hinrichsen. CFD simulation of bubble column flows: Comparative analysis of different formulations of standard k-ε turbulence model, Jahrestreffen Reaktionstechnik, Würzburg, Germany, 2013.

- Yefei Liu, Olaf Hinrichsen. CFD study of gas-solid hydrodynamics and catalyzed methanation reactions in a fluidized-bed reactor. 23rd International Symposium on Chemical Reaction Engineering, Bangkok, Thailand, 2014.

Appendix B

Curriculum Vitae

Yefei Liu was born on October 16th 1984 in Shandong, P. R. China. After accomplishing his high school education at hometown in 2004, he started his study in Department of Chemical Engineering, Qingdao University, Qingdao, Shandong, China, and received his Bachelor's degree in July 2008. In September 2008, he went on to study Chemical Reaction Engineering and Technology in Beijing Key Laboratory of Green Reaction Engineering and Technology, Department of Chemical Engineering, Tsinghua University, Beijing, China, under the supervision of Prof. Tiefeng Wang. In June 2011, he graduated with the Master's degree, and his thesis was entitled "Study on Partial Oxidation of Methane for Acetylene Synthesis Based on Detailed Reaction Kinetics". He obtained the award for Tsinghua University Excellent Master's Thesis. In October 2011, he joined the research group of Prof. Kai-Olaf Hinrichsen and started his Ph.D. study at Lehrstuhls I für Technische Chemie, Technische Universität München, Germany. His research focuses on the computational fluid dynamics simulations of gas-solid and gas-liquid flows using the open source CFD package OpenFOAM®.

Appendix C

Declaration

I hereby certify that I am the sole author of this thesis.

I certify that, to the best of my knowledge, my thesis does not infringe upon anyone's copyright nor violate any proprietary rights and that any ideas, techniques, quotations, or any other material from the work of other people included in my thesis, published or otherwise, are fully acknowledged in accordance with the standard referencing practices. Furthermore, I certify that I have obtained a written permission from copyright owner(s) to include copyrighted material(s) in my thesis and have included copies of such copyright clearances right after first appearance of the material.

I declare that this is a true copy of my thesis, including any final revisions, and that this thesis has not been submitted for a higher degree to any other University or Institution.

I am familiar with the relevant course of examination for doctoral candidates at the Technische Universität München (Promotionsordnung).

Garching, October 14, 2014   Yefei Liu